Turkish Journal of Civil Engineering

formerly
Teknik Dergi

Turkish Journal of Civil Engineering (formerly Teknik Dergi) Publication Principles

Turkish Journal of Civil Engineering (TJCE), a non-profit, open access scientific and technical periodical of UCTEA Chamber of Civil Engineers, publishes papers reporting original research work and major projects of interest in the area of civil engineering. TJCE annually publishes six issues and is open to papers in English and Turkish. It should be noted that TJCE (formerly, Teknik Dergi/ Technical Journal of Turkish Chamber of Civil Engineers) is being published regularly for more than 30 years since 1990. Main publication principles of TJCE are summarized below:

1. Articles reporting original scientific research and those reflecting interesting engineering applications are accepted for publication. To be classified as original, the work should either produce new scientific knowledge or add a genuinely new dimension to the existing knowledge or develop a totally new method or substantially improve an existing method.

2. Articles reporting preliminary results of scientific studies and those which do not qualify as full articles but provide useful information for the reader can be considered for publication as technical notes.

3. Discussions received from the readers of the published articles within three months from publication are reviewed by the Editorial Board and then published together with the closing remarks of the author.

4. Manuscripts submitted for publication are evaluated by two or three reviewers unknown to the authors. In the light of their reports, final decision to accept or decline is taken by the Editorial Board. General policy of the Board is to get the insufficient manuscripts improved in line with the reviewers' proposals. Articles that fail to reach the desired level are declined. Reasons behind decisions are not declared.

5. A signed statement is taken from the authors, declaring that the article has not been published as a "journal article or book chapter". In case the Editorial Board is in the opinion that the article has already been published elsewhere with minor changes or suspects plagiarism or a similar violation of ethics, then not only that article, but none of the articles of the same authors are published.

6. Papers reporting works presented as conference papers and developed further may be considered for publication. The conference it was presented to is given as a footnote in the first page.

7. Additionally, a document signed by all authors, transferring the copyright to UCTEA Chamber of Civil Engineers is submitted together with the manuscript.

Turkish Journal of Civil Engineering

formerly
Teknik Dergi

Turkish Journal of Civil Engineering (formerly Teknik Dergi) is a peer reviewed open access periodical publishing papers of original research and interesting practice cases. It addresses both the research community and the practicing engineers.

Turkish Journal of Civil Engineering (formerly Teknik Dergi)

Volume 35   Issue 1   January 2024

CONTENTS

RESEARCH ARTICLE

An Approach for Brick Wall Quantity Take-Off by U-Net Method Based on Deep Learning

Hasan Basri BASAGA[1*]
Kemal HACIEFENDIOĞLU[2]

ABSTRACT

This study presents a deep learning-based method for the quantity take-off in the construction industry. In this context, the brick wall quantity calculation was performed automatically over two-dimensional (2D) pictures by the U-Net method. 280 photos were first taken in the field at different distances and angles. 1960 images were, then, obtained by augmentation to increase the training accuracy. Pixel calculation of the automatically masked area in the images was made for wall estimation. The wall area was calculated by comparing this pixel value with that of the reference brick surface area. The method was tested on four sample photos including different wall images. A parametric study was carried out to reduce the errors. In the study, it has been shown that the proposed method is suitable for brick quantity calculation. In addition, it was concluded that the photo should be taken as close as possible, and more than one brick should be taken as a reference in close-up photos to increase the accuracy.

Keywords: Deep learning, fully convolutional network, U-Net, brick wall, quantity take-off.

1. INTRODUCTION

The advancement of technology has brought digitalization in every field. Especially with the introduction of web-based applications into business life, topics such as automation and big data processing have become even more important. The engineering and construction (AEC) sector closely follows these developments and integrates new ideas inside every day. Since the time factor is very important in the sector, the studies related to fast data analysis, instant job follow-up, instant evaluation of the job, fast communication and fast solutions, etc. have attracted more attention in the sector. In this context, Building Information Modeling (BIM)

technology, which is a three-dimensional (3D) information sharing process that can be used jointly by those involved in the design, construction, and maintenance of different projects, has also accelerated the sector. In addition, the development of artificial intelligence and the creation of solutions for various business areas have been important steps for the construction industry.

Computer vision (CV), a subset of Artificial Intelligence (AI), has revolutionized the analysis of visual data, encompassing images and videos, with the aim of emulating human visual comprehension. This review delves into the progression of CV techniques, tracing their evolution from conventional methods to the transformative influence of deep learning, while emphasizing their application domains and implications for the construction and asset management phases.

Historically, CV relied on manual efforts to design rules-based detectors and handcrafted feature descriptors to detect and classify objects within images [1]. These techniques encompassed feature detectors such as edge detection, corner detection, and blob detection, and feature descriptors including Scale Invariant Feature Transform (SIFT) [2] and Histogram of Oriented Gradients (HOG) [3]. These methods employed fixed-size rectangular regions sliding across images to apply descriptors and classifiers like Support Vector Machines (SVM) [4], though they proved inflexible and demanded expert engineering to design effective descriptors [5].

Advancements in machine learning, particularly deep learning, have ushered in a new era for CV. Deep learning enables the creation of Convolutional Neural Networks (CNNs), intricate networks acting as feature extractors that learn from input data, rendering them versatile for various classification tasks [6]. Deep learning fosters "end-to-end" learning, where CNNs autonomously learn and extract features from input images, culminating in enhanced accuracy and robustness [7].

Conventional CV methods and deep learning often synergize to maximize performance. In certain scenarios, techniques like sliding windows and SIFT are employed to identify regions of interest, followed by deep learning models for efficient processing. Techniques like Principle Component Analysis (PCA) are adopted to minimize feature dimensions and prevent model overfitting. The dynamic interplay between traditional and deep learning-based methods enhances outcomes across domains, such as image processing, object classification, object detection, pose estimation, and 3D reconstruction.

CV technology has gained significant attention within the construction industry due to its potential to revolutionize various aspects of project management, safety, quality control, and overall efficiency. Over the past decade, numerous studies have explored the application of CV methods in construction-related tasks. This literature review aims to provide an overview of the key contributions in this field, focusing on safety management, progress monitoring, productivity tracking, and quality control.

In safety management area, Suman and Paneru [8] presented a comprehensive review of CV applications in construction, with a specific emphasis on safety management. They highlighted the current state, opportunities, and challenges in this area, shedding light on the potential of CV to enhance safety practices. Meanwhile, Brian et al. [9] critically examined the integration of CV technologies for safety science and management in construction. Their review underscored the importance of these technologies and proposed future research

directions to advance safety practices. Moreover, Wu et al. [10] introduced a novel conceptual framework that combined CV and ontology techniques to improve on-site safety management in construction. Their study showcased the potential of semantic reasoning and visual data for enhancing safety protocols. Fang et al. [11] extended this discussion by presenting a framework that integrated deep learning and CV to ensure safety assurance on construction sites. Their work provided insights into the practical implementation of digital technologies to enhance safety performance.

In progress monitoring and productivity tracking, Xu et al. [12] critically reviewed state-of-the-art CV techniques employed for progress monitoring and productivity tracking in construction projects. By analyzing recent advancements, they highlighted the potential of these methods to provide real-time insights into project development. Notably, the potential of CV technology extends beyond individual construction phases. Xu et al. [13] conducted a comprehensive review encompassing the construction, operation, and maintenance phases of civil assets. Their critical assessment underscored the versatility of CV techniques in addressing challenges throughout the lifecycle of civil infrastructure.

Conclusively, these research papers collectively highlight the evolving prospect of CV applications in construction. From safety management to quality control, progress monitoring, and even lifecycle management, the integration of CV technologies promises transformative benefits. However, challenges and opportunities remain, suggesting a fertile ground for further research and innovation in this rapidly advancing field.

This study attempts the quantity calculation needed in all areas of the construction industry automatically by using the deep learning method. Since there is no study in the literature in which quantity calculations are made using deep learning, studies on deep learning applications in civil engineering are only summarized below. Since research on deep learning was carried out in various sub-branches of civil engineering, a limited number of studies are included here for information purposes only. Yang et al. [14], Fan et al. [15], and Wang et al. [16] developed deep learning-based methods for counting rebars in stock using images. These three studies are the closest ones to the subject considered in this work. Quantity calculation studies have been generally made on numerical data. For example, Akanbi et al. [17] developed deep learning models to predict the amount (in tonnes) of scrap and waste materials that could be recovered from buildings before demolition.

Many studies have also been carried out within the scope of occupational safety. These studies generally aimed to detect personal protective equipment or to detect situations that are not suitable for occupational health and safety in the field. Some examples are the determination of whether the helmet is worn [18,19], the joint control of helmet and vest [20], the suitability of the body ergonomic posture of the employees [21,22], and checking if there is a safety guardrail [23].

Another issue emphasized in the AEC industry is crack detection. To detect cracks in concrete surfaces, Pan et al. [24] developed a deep learning-based spatial channel hierarchical network. Yang et al. [25] proposed a new transfer learning method to detect concrete cracks in superstructures. Kang et al. [26] developed a hybrid method producing a pixel-based solution to measure crack thickness and length. In addition to method development studies, crack detection was also carried out in different structures and materials. For example,

structural cracks [27], cracks in buildings [28], road cracks [29,30], shield tunneling [31], cracks inside steel box girders of bridges [32], concrete highway bridges [33], etc.

The deep learning method has been used to produce solutions in different areas of the construction industry. 3D models classification of Building Information Modelling [34,35], construction cost prediction [36,37], building energy system behaviour prediction [38], long term electricity and heating load prediction [39,40], landslide detection [41], determination of earthquake-induced ground failure effects [42] are some examples. There are also literature reviews in which the research work on deep learning and machine learning in the construction sector is given [43,44].

2. AIM OF THE RESEARCH

The aim of this study is to present a method that uses deep learning and image processing techniques to automate the brick wall quantity take-off process from photographs. The proposed method offers several advantages. It eliminates the need for manual measurement, reduces the potential for human error, and increases the speed and accuracy of the take-off process. Furthermore, it can be used for progress control, as it enables automatic tracking of the construction process by comparing the actual construction progress with the planned progress based on the estimated brick quantity. The proposed method can also be integrated with Building Information Modeling (BIM) processes, which can improve the overall efficiency and accuracy of the construction project. Therefore, the objective of this study is to demonstrate the feasibility and effectiveness of using deep learning and image processing techniques for automating the brick wall quantity take-off process and its potential for integration with BIM processes and progress control.

3. U-NET ARCHITECTURE

The fully convolutional network [45] is an architecture for semantic segmentation. In the segmentation process, the image is divided into multiple parts to simplify the representation of the image. ResNet, SegNet, and U-Net are the architectures that are commonly used for fully convolutional networks. In this study, U-Net [46] is used. The architecture of U-Net is built based on a fully convolutional network for pixel-based classification, which is not an image (object) classification. The main difference between U-Net and traditional convolutional neural networks is that the former has the segmented image output, the latter has the image class output. U-Net is like a U-shaped model and has two parts. The first part is the encoder and the second part is the decoder. In the encoder part, by decreasing the dimension, it is progressed downwards. There are two convolution layers which are the max-pooling and dropout layers in each level.

The original U-Net architecture is designed for images with the size of 572×572×3. However, as the input size of the network increases, much more processing power is needed, so it was preferred to train a smaller network model. Input image which is 128×128 pixels was decreased by half at each level, as a result, it becomes 8×8 pixels at the fifth level. On the contrary, the decoder part continues by increasing the image dimensions from the fifth level to upwards. A segmented image with the same size as the input was obtained at the output. The ReLU activation function was used in the convolution layers and the kernel size in the max-pooling layers was taken by 2×2 pixels. The network is shown in Fig. 1 [46].
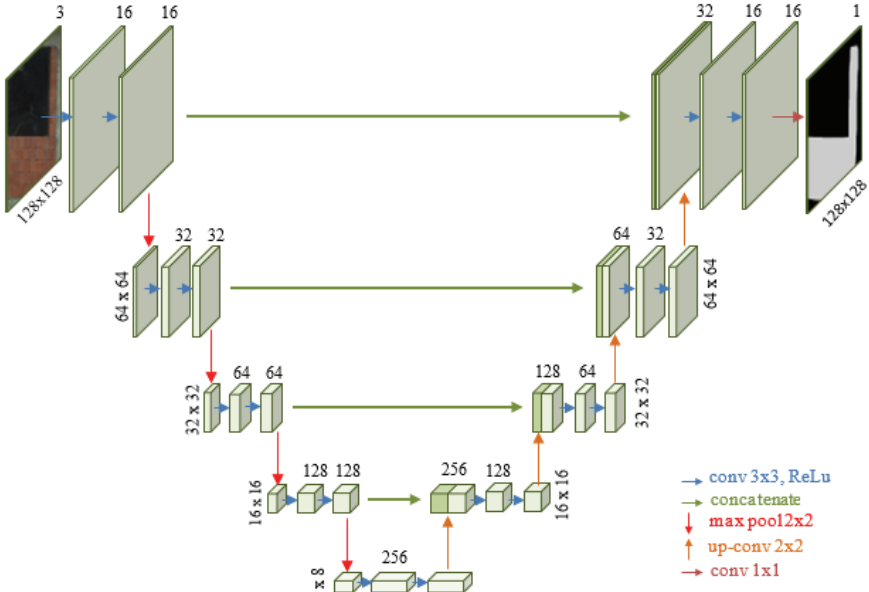
Fig 1 - U-Net architecture [46]

4. MATERIALS AND METHODS

This study, in which brick wall quantity take-offs are made with the U-Net method based on deep learning, consists of two stages:

1. Identifying the area view of the brick wall on the photo with the U-Net method
2. Calculation of the identified wall area.

The methodology of the study is given in Fig. 2.

4.1. Data Sources

The photos used in the training for automatic brick wall detection were taken by the authors with the help of a mobile phone. Different buildings were used so that the data set is not created by the photos of the walls made by the same master. To represent any condition, the photos were taken from different distances, different angles, indoors, outdoors, sunny areas, shaded areas, etc. In this way, a total of 280 images with 3024×3024 pixels were obtained. Some examples of wall photos are shown in Fig. 3.

4.2. Mask the Images

The training data prepared for the U-Net method was divided into two groups as the original image and the masked image. Masked images were obtained by painting the region to be

determined in the original images with a single color and the other parts with a different color. In the 280 photos used in the study, the areas with walls are masked as white, and the other areas are masked as black. Examples of masked images are given in Fig. 4.
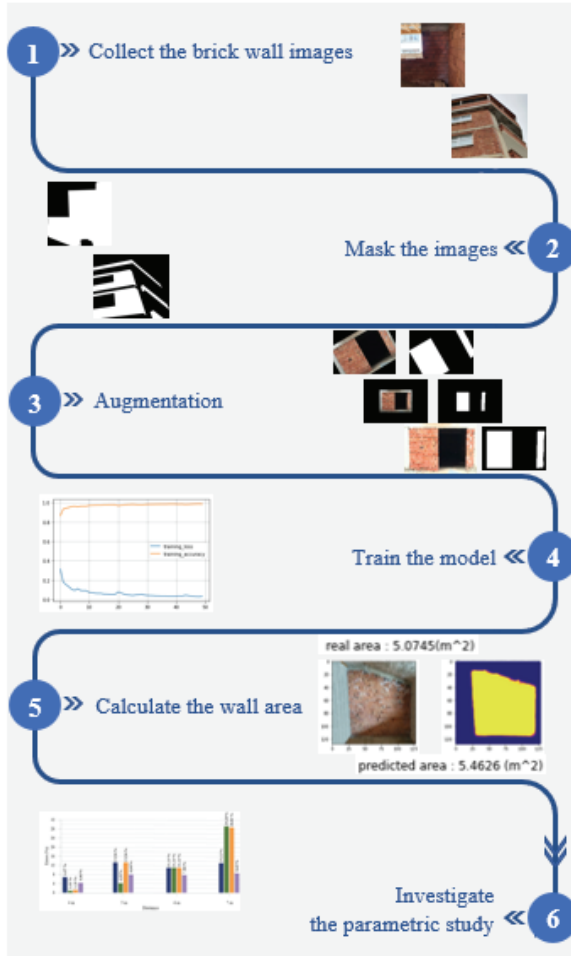
Fig. 2 - The methodology of the study

Fig. 3 - Examples of brick wall images

a. Original images

b. Masked form of the original images

Fig. 4 - Masked images

4.3. Augmentation

In the absence of a suitable dataset, the method of increasing the data is generally used for better training. Certain image enhancement techniques have been used to increase the amount of training data in the analysis. This is because the masking process takes too long. Masking a photo takes between 1-5 minutes, depending on the amount of detail. It took approximately 12 hours to mask the 280 images used in the study. The data has been duplicated because more image masking will require more effort and time. For this purpose, brightness (dark), brightness (light), rotation (30°), flip (vertical), rotation (-30°), and zoom (out) were performed for each photo. The same operations were performed on masked images. Thus, a total of 1960 images were obtained by adding 1680 (280×6) more images to the training set. Table 1 shows the operations for two images.

4.4. Settings

The study used Google Colab Notebook with virtual GPU, which is a free cloud service. This system develops deep learning applications using popular libraries such as Keras, TensorFlow, PyTorch, and OpenCV. Colab, up to Tesla K80 with 12 GB of GDDR5 VRAM, Intel Xeon Processor with two cores @ 2.20 GHz and 13 GB RAM, provided 12 hours of continuous execution time.

4.5. Accuracy Assessment

The IoU score is a standard performance measure for the object category segmentation problem. Given a set of images, the IoU measure gives the similarity between the predicted region and the ground-truth region for an object presented in the set of images and is defined by the following [47]:

$$IoU = \frac{TP}{TP+FP+FN} \tag{1}$$

where, TP, FP, and FN denote the true positive, false positive, and false negatives, respectively. If the prediction is completely correct, then IoU = 1. The lower the IoU, the worse the prediction result.

Table 1 - The augmented form of the images

Orginal	Brightness (dark)	Brightness (light)	Flip (Vertical)	Rotation (30^0)	Rotation (-30^0)	Zoom (out)
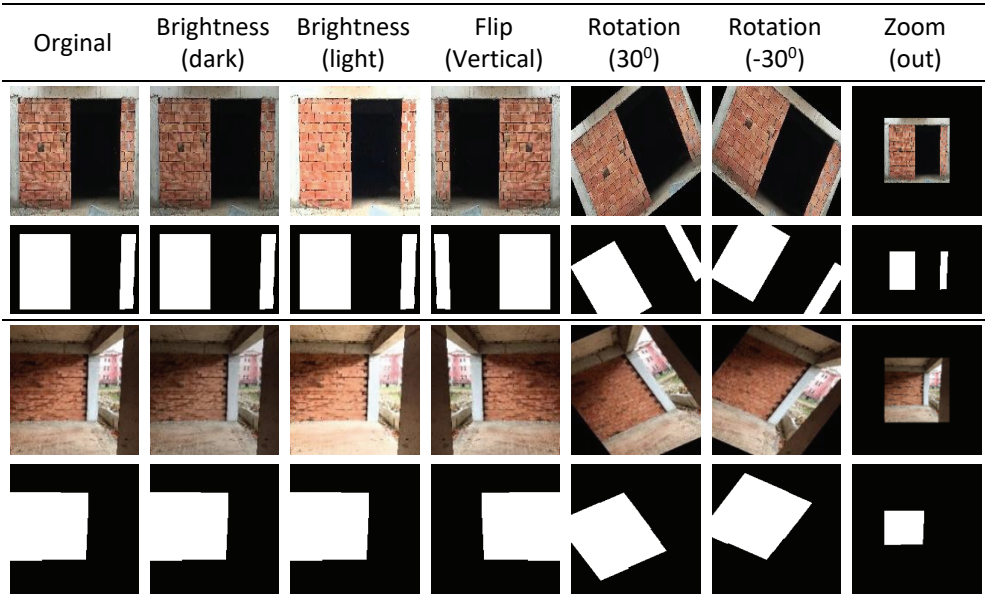
5. RESULTS

5.1. Model Training

The data set was trained using the U-Net architecture. 80% of the data set (1960 images) was reserved as training data and 20% as validation data. The number of epochs was set as 50 and the batch size was 16 since the running of the training data in the corresponding dataset of the model created for brick wall detection was considered as one epoch. The loss function and accuracy values are given in Table 2.

Table 2 - Loss assessment and accuracy results of U-Net architecture

Loss Function	Accuracy Value
0.0338	0.9846

The results of the loss evaluation and accuracy of the 128×128 U-Net architecture are shown in Fig. 5. In these graphics, blue curves indicate the training accuracy, and orange ones show the training loss rate. The best validation value was obtained at step 40.

The average IoU value of the training data set was calculated to be 0.95. This value also supports the results given in Table 2 and Fig. 5. According to the results obtained, the training data and epoch value were sufficient to identify the brick wall and high success was achieved. A comparison of masked and predicted images of some photos included in the training data is given in Fig. 6. They are selected from images with different IoU values.
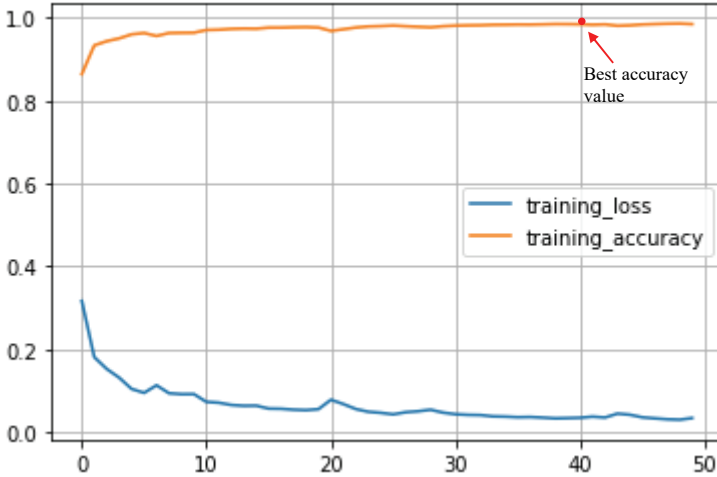
Fig. 5 - Loss assessment and accuracy results of U-Net architecture
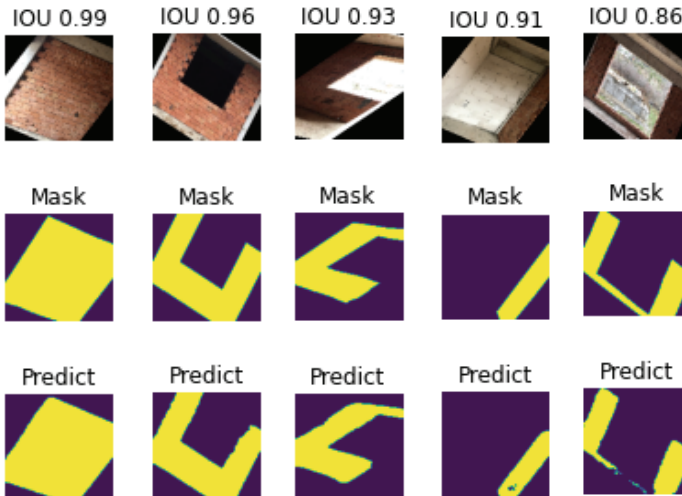
Fig. 6 - Comparison of masked and predicted images
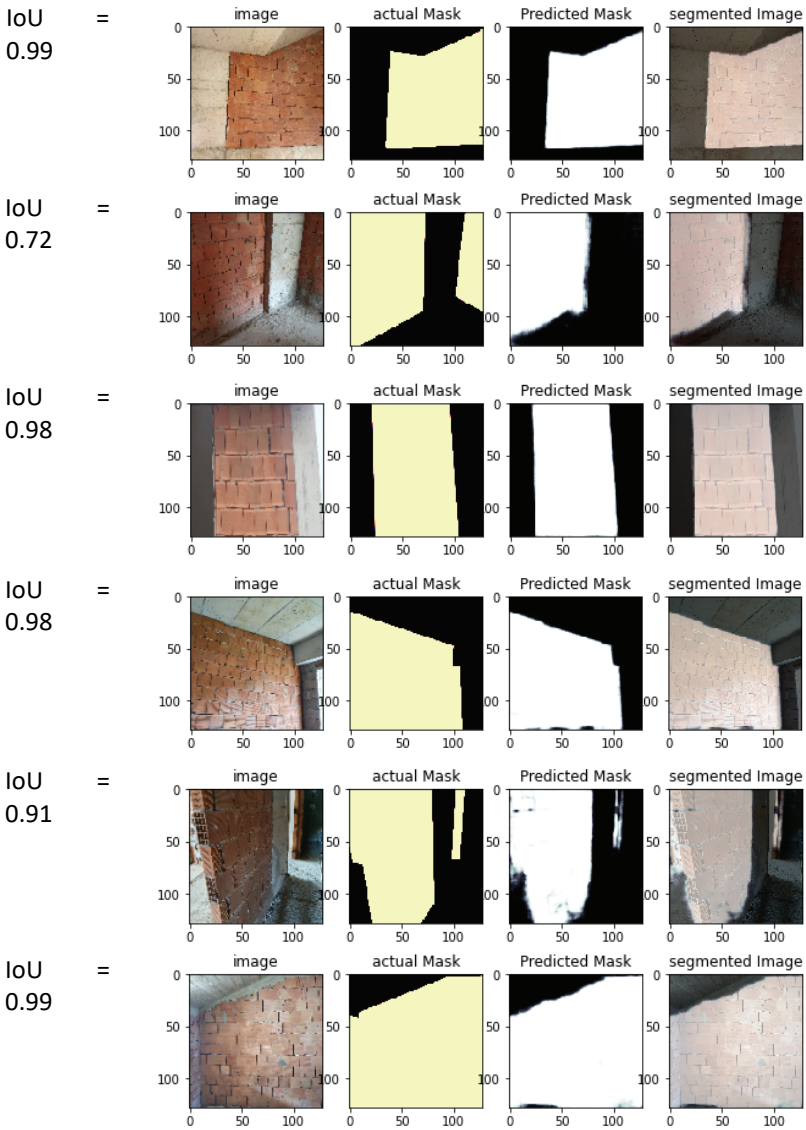
Fig. 7 - The segmentation results of the images

To test the success of the trained model, images taken from a different building, which are not included in the training dataset, were used. Fig. 7 shows the masked and predicted states of these images and the projection of the estimated area on the original image. While choosing the photos, the ones with complex wall shapes and details were preferred. According to the results, it is observed that most images have a high IoU value. Among the factors that reduce the value of the IoU (in other words, the success of identifying the wall) can be counted as light reflections, the presence of regions in the dark area, the details not

being seen very clearly. Success at this stage is very important, as identifying the correct location of the wall directly affects the finding of the wall area. Here, it is necessary to consider the factors affecting the success while taking the photo of the wall to be calculated.

5.2. The Brick Wall Area Calculation

Using the trained data set, the location of the brick walls can be detected and masked on the photo. This area can be calculated in pixel size. However, a reference field on the image is necessary to convert the pixel-sized area to the actual field value since the distance to the wall or the angle of shooting changes the pixel area of the wall on the photo. In this case, a transformation is not possible to calculate the actual field value. In this study, a method for this transformation is presented. The brick area was taken as the reference area on the photo of the wall whose area will be calculated. Since the actual dimensions of the brick are known, the transformation was performed with the following formula:

$$Brick\ wall\ predicted\ area = \frac{Brick\ wall\ predicted\ pixel\ area}{Brick\ pixel\ area} \times Brick\ real\ area \qquad (2)$$

Calculations occur automatically by following the steps below:

1. Any brick is masked on the picture on which the brick wall area calculation will be made

2. The trained model is given the original image, the masked image, and the actual area of the brick

3. The estimated mask image corresponding to the original image from the model is obtained

4. The mask pixel area is calculated on the estimated mask image

5. Brick mask pixel area is calculated

6. With the help of Eq. (2), the estimated wall area is calculated

Four examples were chosen to test the calculations described above: interior wall, outer wall, trapezoidal wall, and wall with a gap. Photos were taken close enough to see the wall with the mobile phone held vertically. No mechanism (such as a tripod) was used to ensure the verticality of the phone while taking the photo. The purpose of this is to measure the wall area estimation performance from photos taken directly from the field. The photos for which the wall area will be calculated and their dimensions are given in Fig. 8. stabilizer, a fully upright position may not be achieved. This may also affect the results. These challenges will be discussed further in the next sections.

After the photos were trained in the U-net model, calculations were made   and then the results are given in Fig. 9. Here, the image in the first column shows the original photo of the wall, the image in the second column shows the masked brick area, and the image in the last column shows the estimated area. A comparison of the results is given in Table 3. The walls are built with 19×19×13.5 cm bricks, and the 19×19 cm surface of the brick forms the wall area.

a. Interior wall

b. Outer wall

c. Trapezoidal wall

d. Wall with a gap
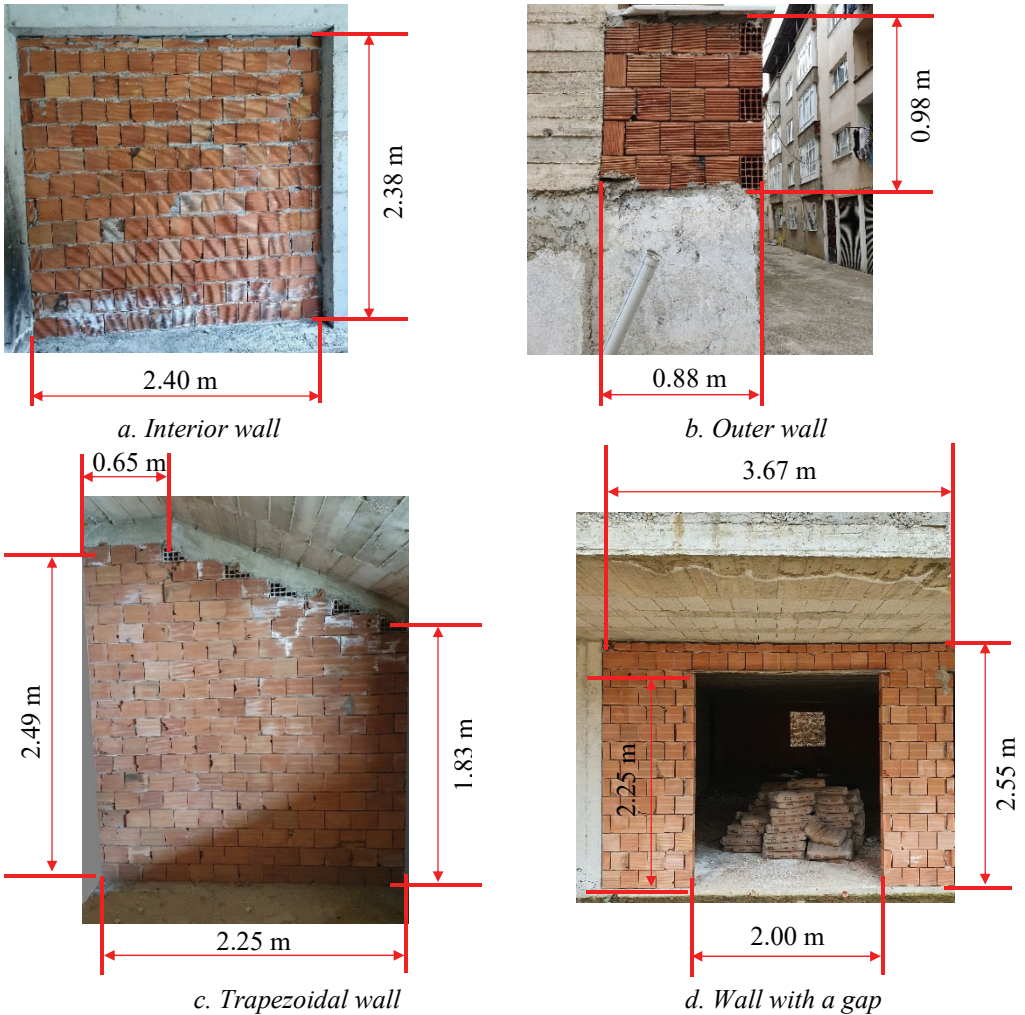
Fig.8 - The dimensions of the test images

As can be seen from Table 3, the error rate in the selected samples is calculated between 3.36 and 9.40. All of the IoU values, that show the success of detecting the wall in the photos, are 0.90 and above. As mentioned earlier, the first step in making a correct prediction is to correctly identify the wall. Mortar particles or dirt on the wall can also affect the masked area, as they can block the detection of the wall. To eliminate this situation and similar ones, it is necessary to increase the variety of photos used in training. This will provide realistic masking. According to the data in the table, there is no direct relationship between IoU and absolute error. This is due to deviations that can be made when masking the reference brick. Since the brick is an element within the wall, it is difficult to define its boundaries precisely. In addition, external factors such as shadows and the mixing of colors are also effective in determining the boundaries of the brick. Further, since the photos were taken without any

Table 3 - Comparison of the real and predicted areas of brick walls

	Real area (m²)	Predicted area (m²)	Absolute Error (%)	IoU
Interior wall	5.7120	5.1753	9.40	0.94
Outer wall	0.8624	0.8334	3.36	0.90
Trapezoidal wall	5.0745	5.4626	7.65	0.98
Wall with a gap	4.8585	4.5711	5.92	0.97
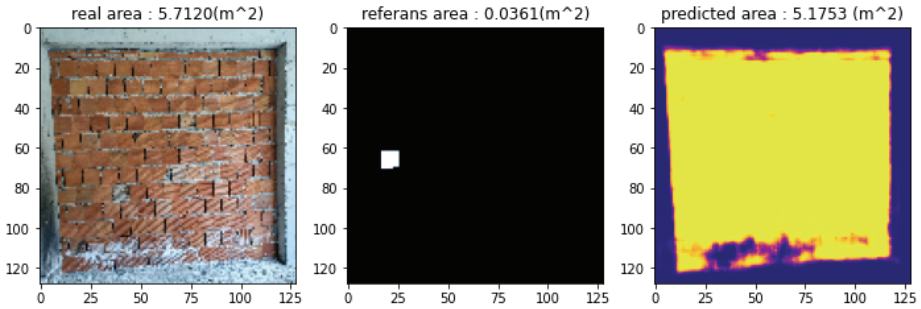
a. Interior wall
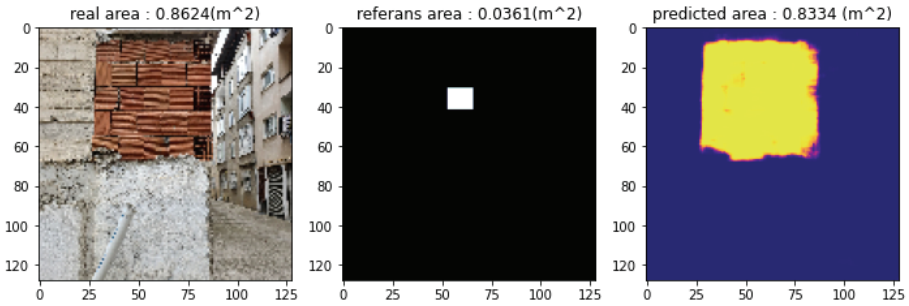
b. Outer wall
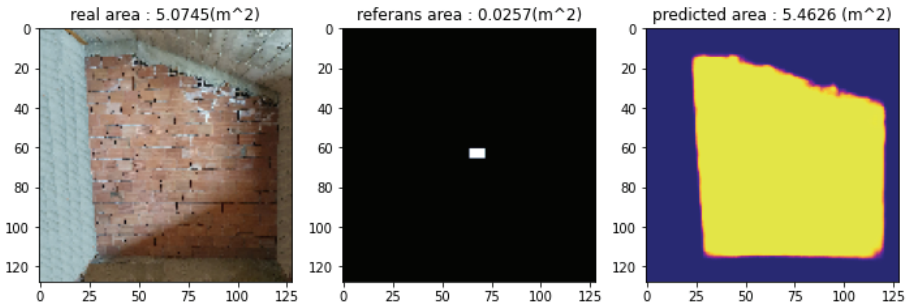
c. Trapezoidal wall
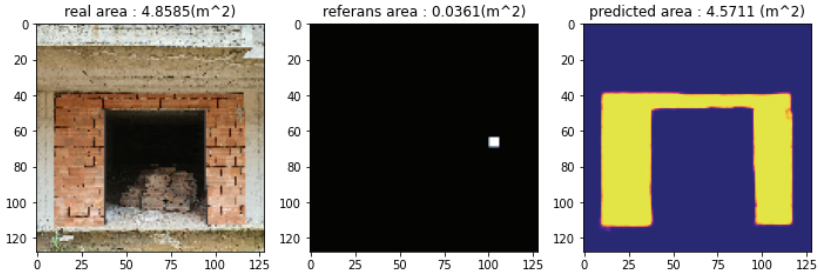
d. Wall with a gap

Fig 9 - The predicted masks and calculated areas by deep learning

5.3. Examining the Effect of Distance on the Wall Area Calculation

The photos, for which the wall area is calculated, were obtained by taking photos from the closest distance to see the wall. To determine the distance effect, photos were taken from a distance of 4, 5, 6, and 7 m from the wall, and the results were compared. Fig. 10 shows the IoU values of the walls and the estimated images. In Fig. 11, the obtained wall areas and errors (%) are shown. As can be seen from the figures, the highest IoU value and the lowest error rate value are obtained from the photographs taken from a distance of 4 m. As the
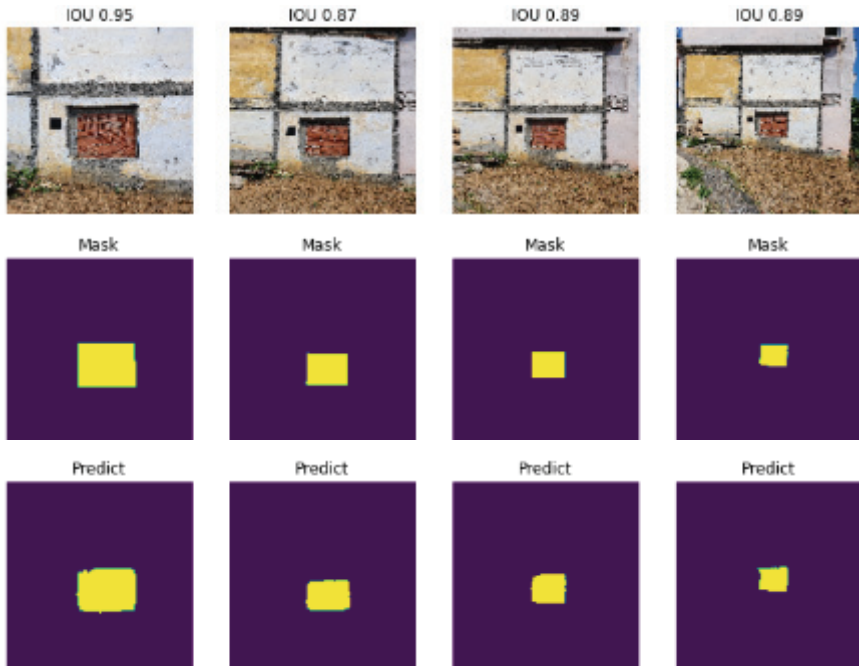
Fig. 10 - IoU values of the walls and the estimated images

distance increases, the loss of details, the more obvious shadows or sun glare, the increase of details entering the photo frame, and the presence of brick-like images cause the IoU to decrease. Also, as the distance increases   it becomes more difficult to mark the reference brick. Therefore, the increase in the distance causes the error rate to increase as well.

5.4. Examining the Effect of Reference Area on the Wall Area Calculation

As stated before, the exact marking of the reference area is of great importance in the correct calculation of the wall area. In particular, as the shooting distance increases, it becomes more difficult to distinguish colors and define brick boundaries. Parametric studies were carried out to reduce the error rate in long-shot images. Accordingly, the wall areas were calculated by considering two bricks, three bricks, and an area other than the brick, and different photographing distances (4, 5, 6, and 7 m). A4 size (21×29.7 cm) black paper was pasted next to the brick wall to determine the reference area outside the brick. The aim here is to examine the results that would be obtained if the reference field is visible at any distance. Table 4 gives reference markings according to the distances. The results obtained are shown in Fig. 12.

In case the photographing distance is 4 m, the error rate for the reference area of two and three bricks decreases to 1%. As the distance increases, the error rates generally increase. If the reference area is an A4 paper, the error rates are approximately close to each other as the photographing distance increases. According to these results, taking a photo of the wall as close as possible and considering more than one brick instead of a single brick as the reference area revealed that the minimum error rate will be obtained in the wall area calculation. If an area other than the brick is taken as a reference, the error rate does not change appreciably   as the distance increases, since this area could be masked more clearly. However, due to the mixing of the color of the paper with the shade, it becomes more difficult to set the paper boundaries as the distance increases, especially during masking. For this reason, color research for different weather conditions on the reference surface will reduce the error rate even more.
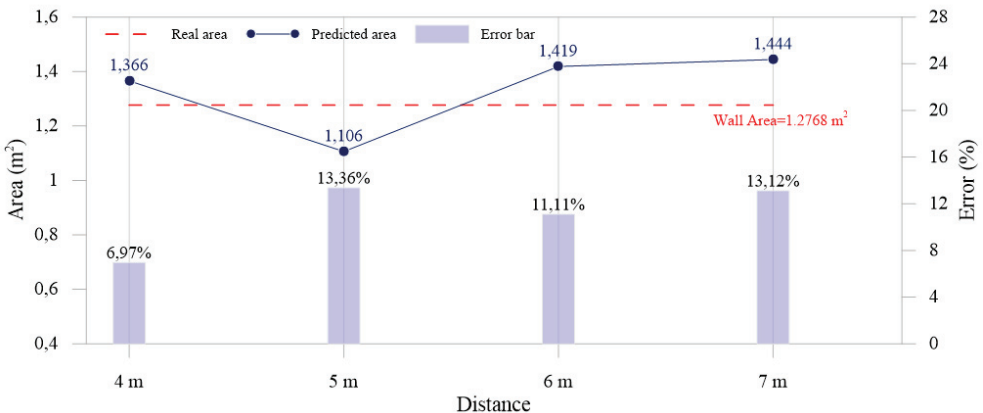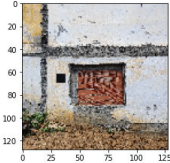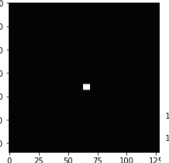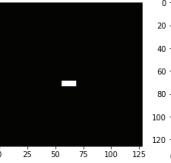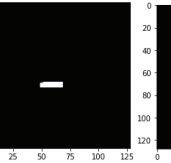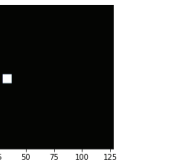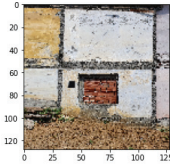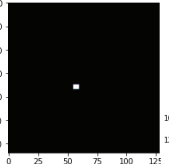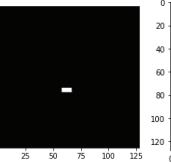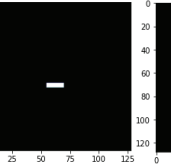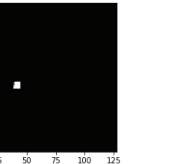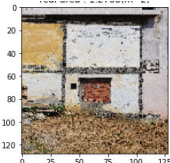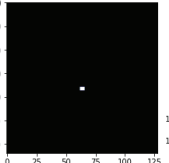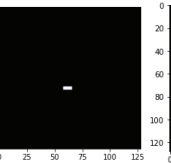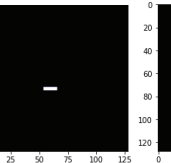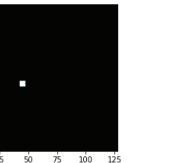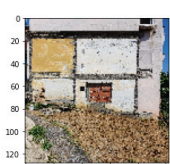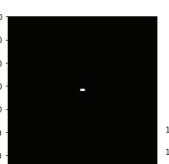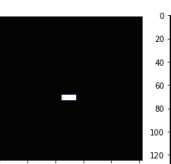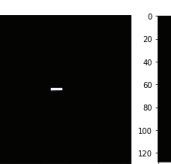
Fig. 11 - The calculated wall areas and errors (%)

Table 4 - The reference markings according to distances

Distance	Original	Ref: 1 brick	Ref: 2 bricks	Ref: 3 bricks	Ref: A4 paper
4 m					
5 m					
6 m					
7 m					

a. The wall areas
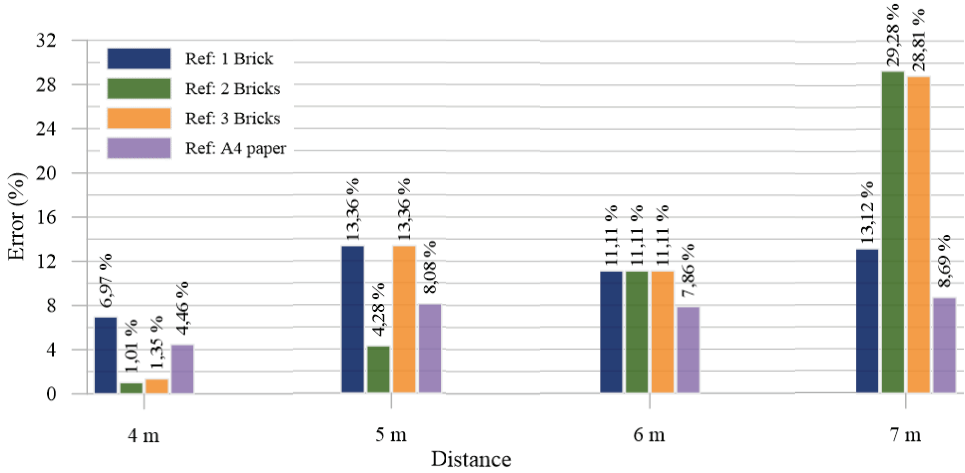
b. The errors

Fig. 12 - The wall areas and calculation errors according to distances and reference point

6. DISCUSSIONS

This study aimed to calculate the wall area automatically from the photograph by using the deep learning method. In this context, first of all, it is necessary to automatically determine the wall from the photograph. For this purpose, the photographs obtained by the authors were masked and trained with the U-Net segmentation method. The results showed that the dataset was sufficient for training, with high accuracy (98.46% accuracy and 0.95 mean Io U). Accordingly, the wall area can be determined automatically with high accuracy from the photograph. In order to find the real area of the wall determined in the photo, a reference area is needed on the photo. In the study, bricks of known dimensions were selected for this reference. The proposed method for wall area calculation was tested on four different walls; interior rectangle wall, outer rectangle wall, trapezoidal wall, and wall with a gap . The results (mean error: 6.58%) showed that this method can be used to calculate the wall area automatically.

In the study, a parametric study is also conducted to examine the effect of different photo shooting distances and the number of reference bricks on the accuracy of the wall area calculation. The results showed that taking photos from a closer distance can significantly reduce the error rate. For instance, when the photo shooting distance was 4m, the error rate was 6.97%, which is significantly lower than the error rates obtained from photos taken from 5m, 6m, and 7m distances.

Furthermore, in the study, the effect of using different numbers of bricks as a reference area has also been investigated. It was observed that taking more bricks as a reference area can significantly reduce the error rate. For instance, using two bricks as a reference area resulted in an error rate as low as 1.01% when the photo shooting distance was 4m. However, using

three bricks as a reference area did not always lead to a lower error rate. In some cases, it resulted in a higher error rate compared to using only one brick as a reference area.

Additionally, in the study, the effect of using an A4 size paper affixed to the wall as a reference area. has been examined, too. The results showed that using an A4 size paper can also lead to a lower error rate compared to using only one brick as a reference area. However, it is important to note that the error rate obtained with this method was not as low as the error rate obtained when using two bricks as a reference area. Overall, the results of the parametric study suggest that taking photos from a closer distance and using more bricks or an A4 size paper as a reference area can significantly improve the accuracy of the wall area calculation. These findings can contribute to the body of knowledge by providing valuable insights into the factors that can affect the accuracy of wall area calculations and the ways to improve them.

The proposed method can be integrated to BIM processes, which can provide valuable information for construction projects. By using the proposed method, the wall area can be automatically calculated and added to the BIM model, which can reduce the time and cost of manual quantity take-off. Additionally, the proposed method can be used for real-time data collection on construction sites. By using a mobile device, the workers can take photos of the walls, and the proposed method can automatically calculate the wall area. This can provide real-time information for project managers, which can help them make informed decisions and monitor the progress of the project.

Finally, the proposed method can be used in conjunction with digital twin technology. By creating a digital twin of the construction site, the proposed method can be used to automatically calculate the wall area in the virtual environment. This can provide valuable insights for architects and engineers, and can help them optimize the design and construction processes. Overall, the proposed method has the potential to improve the efficiency and accuracy of construction projects, and can be integrated with various digital technologies to provide valuable insights for construction professionals.

7. CONCLUSIONS

This study presented a novel method for automatically estimating brick wall quantity from photographs using deep learning. The U-Net architecture was employed to train a model to accurately mask the location of the wall on the photo, followed by estimating the actual area of the wall based on a reference area of known size. Our results showed that the model achieved an accuracy of 0.9846 with an IoU of 0.95, and the maximum error rate was 9.40% for the tested photos. Overall, these findings can be used to inform best practices for brick wall quantity take-off automation and provide guidance for improving the accuracy of construction estimation processes.

In the study, parametric studies were carried out to show the effect of the reference area and the shooting photo distance on the calculation of the wall area. The results showed that taking photographs at a closer distance and using multiple bricks as a reference area can significantly reduce the error rate in wall area calculations. These results showed that the main limitation of the current method is that the distance between the camera and the wall can affect the accuracy of the wall area calculation. Accordingly, future studies should be on developing

methods that can eliminate the effect of camera distance in wall area calculations. In addition, it is recommended to investigate the integration of the proposed method to   Building Information Modeling (BIM) processes and real-time data collection for more efficient use of this system.

In summary, the study demonstrates the potential of deep learning in automating brick wall quantity take-off from photos, and provides valuable insights for further research and development in this area.

Declaration of Competing Interest

The author declares that they have no known competing financial interests or personal relationships that could have appeared to influence the work reported in this paper.

References

[1] Huang, T.S. Computer Vision: Evolution And Promise. In 19th CERN School of Computing, CERN, Geneva; 1996; pp. 21–25.

[2] Lowe, D.G. Distinctive Image Features from Scale-Invariant Keypoints. Int J Comput Vis, 2004, 60, 91–110.

[3] Dalal, N.; Triggs, B. Histograms of Oriented Gradients for Human Detection. Proceedings - 2005 IEEE Computer Society Conference on Computer Vision and Pattern Recognition, CVPR 2005, 2005, I, 886–893.

[4] Cristianini, N.; Shawe-Taylor, J. An Introduction to Support Vector Machines and Other Kernel-Based Learning Methods; Cambridge University Press, 2000.

[5] O'Mahony, N.; Campbell, S.; Carvalho, A.; Harapanahalli, S.; Hernandez, G.V.; Krpalkova, L.; Riordan, D.; Walsh, J. Deep Learning vs. Traditional Computer Vision. Advances in Intelligent Systems and Computing, 2020, 943, 128–144.

[6] Nanni, L.; Ghidoni, S.; Brahnam, S. Handcrafted vs. Non-Handcrafted Features for Computer Vision Classification. Pattern Recognit., 2017, 71, 158–172.

[7] Chan, T.H.; Jia, K.; Gao, S.; Lu, J.; Zeng, Z.; Ma, Y. PCANet: A Simple Deep Learning Baseline for Image Classification? IEEE Transactions on Image Processing, 2015, 24, 5017–5032.

[8] Paneru, S.; Jeelani, I. Computer Vision Applications in Construction: Current State, Opportunities & Challenges. Autom Constr, 2021, 132.

[9] Guo, B.H.W.; Zou, Y.; Fang, Y.; Goh, Y.M.; Zou, P.X.W. Computer Vision Technologies for Safety Science and Management in Construction: A Critical Review and Future Research Directions. Saf Sci, 2021, 135, 105130.

[10] Wu, H.; Zhong, B.; Li, H.; Love, P.; Pan, X.; Zhao, N. Combining Computer Vision with Semantic Reasoning for On-Site Safety Management in Construction. Journal of Building Engineering, 2021, 42.

[11] Fang, W.; Ding, L.; Love, P.E.D.; Luo, H.; Li, H.; Peña-Mora, F.; Zhong, B.; Zhou, C. Computer Vision Applications in Construction Safety Assurance. Autom Constr, 2020, 110.

[12] Xu, S.; Wang, J.; Shou, W.; Ngo, T.; Sadick, A.M.; Wang, X. Computer Vision Techniques in Construction: A Critical Review. Archives of Computational Methods in Engineering, 2021, 28, 3383–3397.

[13] Xu, S.; Wang, J.; Wang, X.; Shou, W. Computer Vision Techniques in Construction, Operation and Maintenance Phases of Civil Assets: A Critical Review. Proceedings of the 36th International Symposium on Automation and Robotics in Construction, ISARC 2019, 2019, 672–679.

[14] Li, Y.; Lu, Y.; Chen, J. A Deep Learning Approach for Real-Time Rebar Counting on the Construction Site Based on YOLOv3 Detector. Autom Constr, 2021, 124, 103602.

[15] Fan, Z.; Lu, J.; Qiu, B.; Jiang, T.; An, K.; Josephraj, A.N.; Wei, C. Automated Steel Bar Counting and Center Localization with Convolutional Neural Networks. 2019.

[16] Wang, H.; Polden, J.; Jirgens, J.; Yu, Z.; Pan, Z. Automatic Rebar Counting Using Image Processing and Machine Learning. In 2019 IEEE 9th Annual International Conference on CYBER Technology in Automation, Control, and Intelligent Systems (CYBER); IEEE, 2019; pp. 900–904.

[17] Akanbi, L.A.; Oyedele, A.O.; Oyedele, L.O.; Salami, R.O. Deep Learning Model for Demolition Waste Prediction in a Circular Economy. J Clean Prod, 2020, 274, 122843.

[18] Fang, Q.; Li, H.; Luo, X.; Ding, L.; Luo, H.; Rose, T.M.; An, W. Detecting Non-Hardhat-Use by a Deep Learning Method from Far-Field Surveillance Videos. Autom Constr, 2018, 85, 1–9.

[19] Wu, J.; Cai, N.; Chen, W.; Wang, H.; Wang, G. Automatic Detection of Hardhats Worn by Construction Personnel: A Deep Learning Approach and Benchmark Dataset. Autom Constr, 2019, 106, 102894.

[20] Nath, N.D.; Behzadan, A.H.; Paal, S.G. Deep Learning for Site Safety: Real-Time Detection of Personal Protective Equipment. Autom Constr, 2020, 112, 103085.

[21] Yu, Y.; Li, H.; Yang, X.; Kong, L.; Luo, X.; Wong, A.Y.L. An Automatic and Non-Invasive Physical Fatigue Assessment Method for Construction Workers. Autom Constr, 2019, 103, 1–12.

[22] Yang, K.; Ahn, C.R.; Kim, H. Deep Learning-Based Classification of Work-Related Physical Load Levels in Construction. Advanced Engineering Informatics, 2020, 45, 101104.

[23] Kolar, Z.; Chen, H.; Luo, X. Transfer Learning and Deep Convolutional Neural Networks for Safety Guardrail Detection in 2D Images. Autom Constr, 2018, 89, 58–70.

[24] Pan, Y.; Zhang, G.; Zhang, L. A Spatial-Channel Hierarchical Deep Learning Network for Pixel-Level Automated Crack Detection. Autom Constr, 2020, 119, 103357.

[25] Yang, Q.; Shi, W.; Chen, J.; Lin, W. Deep Convolution Neural Network-Based Transfer Learning Method for Civil Infrastructure Crack Detection. 2020.

[26] Kang, D.; Benipal, S.S.; Gopal, D.L.; Cha, Y.-J. Hybrid Pixel-Level Concrete Crack Segmentation and Quantification across Complex Backgrounds Using Deep Learning. Autom Constr, 2020, 118, 103291.

[27] Yang, C.; Chen, J.; Li, Z.; Huang, Y. Structural Crack Detection and Recognition Based on Deep Learning. Applied Sciences, 2021, 11, 2868.

[28] Zheng, M.; Lei, Z.; Zhang, K. Intelligent Detection of Building Cracks Based on Deep Learning. Image Vis Comput, 2020, 103, 103987.

[29] Zhou, S.; Song, W. Deep Learning-Based Roadway Crack Classification Using Laser-Scanned Range Images: A Comparative Study on Hyperparameter Selection. Autom Constr, 2020, 114, 103171.

[30] Hacıefendioğlu, K.; Başağa, H.B. Concrete Road Crack Detection Using Deep Learning-Based Faster R-CNN Method. Iranian Journal of Science and Technology, Transactions of Civil Engineering, 2021.

[31] Zhou, C.; Xu, H.; Ding, L.; Wei, L.; Zhou, Y. Dynamic Prediction for Attitude and Position in Shield Tunneling: A Deep Learning Method. 2019.

[32] Xu, Y.; Bao, Y.; Chen, J.; Zuo, W.; Li, H. Surface Fatigue Crack Identification in Steel Box Girder of Bridges by a Deep Fusion Convolutional Neural Network Based on Consumer-Grade Camera Images. Struct Health Monit, 2019, 18, 653–674.

[33] Zhang, C.; Chang, C.; Jamshidi, M. Concrete Bridge Surface Damage Detection Using a Single-stage Detector. Computer-Aided Civil and Infrastructure Engineering, 2020, 35, 389–409.

[34] Wang, L.; Zhao, Z.; Xu, N. Deep Belief Network Based 3D Models Classification in Building Information Modeling. International Journal of Online and Biomedical Engineering (iJOE), 2015, 11, 57.

[35] Wang, L.; Zhao, Z.; Wu, X. A Deep Learning Approach to the Classification of 3D Models under BIM Environment. International Journal of Control and Automation, 2016, 9, 179–188.

[36] Rafiei, M.H.; Adeli, H. A Novel Machine Learning Model for Estimation of Sale Prices of Real Estate Units. J Constr Eng Manag, 2016, 142, 04015066.

[37] Rafiei, M.H.; Adeli, H. Novel Machine-Learning Model for Estimating Construction Costs Considering Economic Variables and Indexes. J Constr Eng Manag, 2018, 144, 04018106.

[38] Mocanu, E.; Nguyen, P.H.; Gibescu, M.; Kling, W.L. Deep Learning for Estimating Building Energy Consumption. Sustainable Energy, Grids and Networks, 2016, 6, 91–99.

[39] Rahman, A.; Smith, A.D. Predicting Heating Demand and Sizing a Stratified Thermal Storage Tank Using Deep Learning Algorithms. Appl Energy, 2018, 228, 108–121.

[40] Rahman, A.; Srikumar, V.; Smith, A.D. Predicting Electricity Consumption for Commercial and Residential Buildings Using Deep Recurrent Neural Networks. Appl Energy, 2018, 212, 372–385.

[41] Hacıefendioğlu, K.; Demir, G.; Başağa, H.B. Landslide Detection Using Visualization Techniques for Deep Convolutional Neural Network Models. Natural Hazards, 2021.

[42] Hacıefendioğlu, K.; Başağa, H.B.; Demir, G. Automatic Detection of Earthquake-Induced Ground Failure Effects through Faster R-CNN Deep Learning-Based Object Detection Using Satellite Images. Natural Hazards, 2021, 105, 383–403.

[43] Akinosho, T.D.; Oyedele, L.O.; Bilal, M.; Ajayi, A.O.; Delgado, M.D.; Akinade, O.O.; Ahmed, A.A. Deep Learning in the Construction Industry: A Review of Present Status and Future Innovations. Journal of Building Engineering, 2020, 32, 101827.

[44] Xu, Y.; Zhou, Y.; Sekula, P.; Ding, L. Machine Learning in Construction: From Shallow to Deep Learning. Developments in the Built Environment, 2021, 6, 100045.

[45] Long, J.; Shelhamer, E.; Darrell, T. Fully Convolutional Networks for Semantic Segmentation. 2014.

[46] Ronneberger, O.; Fischer, P.; Brox, T. U-Net: Convolutional Networks for Biomedical Image Segmentation. 2015.

[47] Rahman, M.A.; Wang, Y. Optimizing Intersection-Over-Union in Deep Neural Networks for Image Segmentation. In; 2016; pp. 234–244.

Effects of Ambient Temperature and Magnitude of the Vibration on the Dynamics of Pre-Stressed Precast Isolated Pedestrian Bridges

Fuat ARAS[1]

ABSTRACT

The dynamic properties of structures are known as inherent properties dependent on the mass and stiffness parameters. However, recent studies showed that the temperature and the magnitude of the vibrations also affect them. This study aims to reveal how the ambient temperature and human-induced vibrations alter the modal characteristics of pre-stressed precast isolated pedestrian bridges. For this aim, operational modal analyses have been applied to the Istanbul Medeniyet University pedestrian bridge. Three-bay pre-stressed precast and isolated bridge has been connecting the two campuses of the university for six years and its dynamic properties were investigated during its construction. In this study, the dominant frequencies of the bridge have been determined to see if they changed or not for its service life. Secondly, the dynamic response of the longest bay of the bridge has been evaluated under different temperatures and human-induced vibrations. Through a year, twelve acceleration measurements have been gathered in a temperature range of 5 - 33 °C and representing the different levels of human-induced vibrations, some jumping actions were applied and its response was recorded. While the performed analyses proved that, the dominant frequencies are dependent on the ambient temperature, no significant correlation was obtained between the amplitude of the vibration and the dominant frequencies of the bridge. High-amplitude vibrations have been used for the vibration serviceability check of the bridge, and it is seen that it satisfies the requirements set by different codes.

Keywords: pedestrian Bridge, dynamic response, field test, temperature effect, human-induced vibrations, vibration serviceability.

1. INTRODUCTION

The dynamic properties are inherent assets that are theoretically dependent on the mass and stiffness parameters of structures, but recent studies also proved their dependency on environmental effects, such as traffic, wind, humidity, solar radiation and, most importantly,

---

temperature. The level of change caused by the environmental effects in dynamic properties can mask the changes caused by structural damage. For this reason, considerable efforts were spent investigating the influence of environmental conditions on the dynamic properties of bridges.

The studies have pointed out that temperature is the most important environmental parameter affecting the dynamic parameters of bridges. Ni et al. [1] address the modeling of temperature effects on modal frequencies for a cable-stayed bridge. The authors found that the environmental temperature can change the modal frequencies with a variance range of 0.20% - 1.52% for the first ten modes. For the investigated modes, a decrease in modal frequency is observed with the increase in the temperature of the bridge. Çatbas et al. [2] monitored a long-span truss bridge in the USA for a year. The authors pointed out the importance of ambient temperature on structural reliability. Mosavi et al [3] investigated the effect of temperature variations on the modal characteristics of a two-span steel-concrete composite bridge and concluded that temperature variations can induce modal variability on a daily cycle. Another cable-stayed bridge was investigated by Ni et al. [4]. Both cables and bridge deck have been investigated. The authors reported that for the first mode dominant frequency is not sensitive to temperature change, while for the other modes, an explicit decrease in the modal frequencies has been determined with the increase of the temperature. This dependency arises another problem which is the elimination of temperature effects for structural health monitoring issues. In this direction, Sohn et al. [5] proposed a model to separate the temperature effects in the change of modal frequencies from the effects of structural damage. Peeters and De Roeck [6] used one-year-long monitoring data of a four-span post-tensioned concrete box girder bridge for the same aim. In a more recent study, Ni et al. [7] examined the performance of neural network models to eliminate the temperature-caused modal variability in vibration-based structural damage detection.

Another vital parameter studied in bridges is the magnitude of the vibration induced by human traffic. The importance of the factor mainly stems from the need for checking the serviceability of the bridges. Besides, the variation of the dominant frequencies according to the level of vibration can be another reason. In that respect, many studies can be found in the literature performed in existing bridges. Tubino et al. [8] conducted extensive field tests on two bridges with steel systems to determine their dynamic features and human-induced vibration level. The vibration measurements have been conducted under ambient conditions without human traffic, single pedestrian walking, 10 pedestrian walking, and 15 pedestrian walking conditions. The authors reported maximum acceleration values for each case. Ni et al. [9] applied ambient, forced, and free vibration tests on a pedestrian bridge at the City University of Hong Kong. The modal parameters, i.e., dominant frequencies and damping ratios obtained from the tests were compared. In a more recent study, Moutinho et al. [10] studied the dynamic properties of the historic Dom Luis I truss arch bridge in Portugal with the Peak Picking technique. The authors mainly determined the vibration levels of the bridge at different levels of human activity created in the feast days and athletic races. They also assessed the level of vibrations to human comfort limits. Chen et al. [11] obtained the dynamic properties of an eleven-span post-tensioned concrete bridge under ambient and hybrid excitations in which an artificial force was applied. The authors also used different modal identification methods, such as the autoregressive time series method, the eigensystem realization algorithm with observer/Kalman identification, and stochastic subspace

identification methods. The performed analyses showed that the hybrid excitation tests revealed the high-frequency modes that are not recognized in ambient vibration tests.

The literature survey showed that the investigation of the effects of temperature on the dynamic properties of the pre-stressed precast isolated pedestrian bridges has not been studied in detail. Moreover, the relation between the magnitude of the vibration and dominant frequencies was not studied either. To fill this gap in the literature, a field testing plan has been applied to the Istanbul Medeniyet University pedestrian bridge which is a pre-stressed precast isolated reinforced one. The dynamic properties of it were already investigated six years ago when it was taken under service immediately after its construction [12]. In this study, the dynamic properties of the bridge have been determined again and compared to those extracted by Aras [12] to see if they are changed for its six-year service life. A testing plan has been applied within the frame of the Structural Health Monitoring Laboratory course in the Civil Engineering Department of Istanbul Medeniyet University. Throughout the course, eight measurements have been recorded. To answer the specified questions proficiently, additional measurements, i.e., one before the semester on 30 July 2021, and two after the semester in May and June 2022, were conducted. Thereby, a wide temperature range was aimed. Different human-induced vibrations have been applied by the students of the course in different jumping scenarios. The analyses were performed in the vertical direction of the longest span of the bridge to present the results in the most relevant way.

The modal parameter estimation of a structural system based on its vibration response is very important and many signal processing techniques have been developed and validated. These techniques are ranging from frequency domain algorithms based on the Fourier transform, such as peak picking and frequency domain decomposition, to time domain algorithms, such as the Eigensystem realization algorithms and the stochastic system identification [13, 14]. A few studies used both methods to obtain the dynamic properties of structures and stated that they give similar findings [15-16]. The frequency domain methods are the most practical methods to apply in existing civil structures [17]. This study is mainly based on the monitoring of the dominant frequencies of the bridge since no change is expected in the mode shapes. For this reason, the presentation of the signals in the frequency domain enables to reach the intended aim. Hence, the peak-picking technique as a more practical and straightforward modal identification technique is preferred in this study.

The obtained data have been analyzed to see how the ambient temperature and human-induced vibrations affect the dynamic properties of the bridge and if the vibration serviceability requirements are satisfied or not. Before giving the details of the measurements and analysis, the structural details of the studied bridge have been presented in the next section.

2. THE STUDIED BRIDGE

The studied bridge is known as the Istanbul Medeniyet University pedestrian overpass and was constructed within the Istanbul Strait Road Tunnel Crossing Project. It connects two campuses of the university and many people use it to cross the main motorway D100. Figure 1 shows the bridge with its neighborhood. The structural system of the bridge contains two reinforced concrete abutments, two mid piers, elastomeric bearings, precast and pre-stressed reinforced concrete girders, reinforced concrete slab, and steel stairs. Two elevators with steel

frame systems also join the bridge abutments from two sides. Caps on the abutments and piers were designed to carry the girders. The abutments also support the steel stair systems. The bridge crosses 69.2 meters via three bays with the span lengths of L1 = 32.3 m., L2 = 22.1 m., and L3 = 12.8 m. The width of the bridge is 5.2 m and two different girder cross-sections are used through the bays. L1 and L2 bays are crossed by four precast pre-stressed girders of 1200 mm height and top flange width is 1275 mm, while L3 is crossed by six precast girders of 900 mm height and top flange width is 800 mm. Figure 2 shows the structural system details of the studied bridge with the locations of the accelerometers and jumping locations used in this study.

Figure 1 - Studied bridge: Istanbul Medeniyet University pedestrian overpass bridge
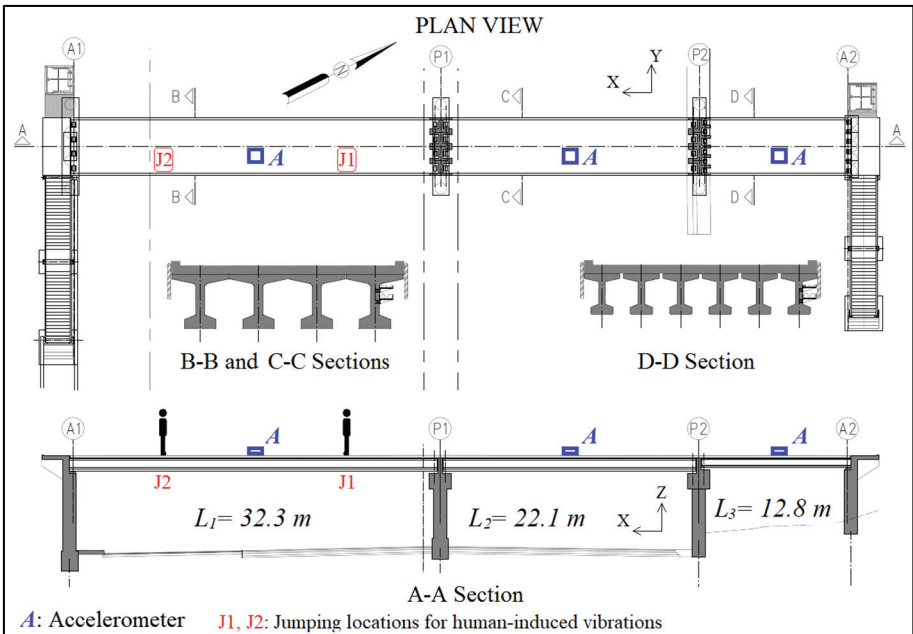
Figure 2 - Structural system of the studied bridge with accelerometer locations
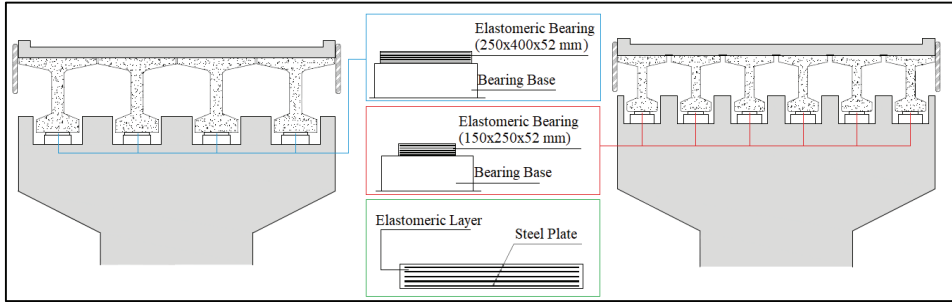
Figure 3 - Details of elastomeric bearings used under the girders

The C35 concrete class is used for all cast-in-place concrete members while C40 is preferred for precast and pre-stressed girders. S420 steel grade is used for all reinforcement. For the pre-stressing strands, 1862 MPa (270 ksi) grade strand is used with a 1.5 cm (0.6 inches) diameter. 21 strands are used for pre-stressing L1 girders, while 8 strands are used for L2 girders. No pre-stressing is applied to L3 girders [18].

Each girder sits on an elastomeric bearing composed of four rubber-type elastomer layers and five steel plates. The thickness of each elastomer layer is 8 mm whereas that of the steel plate is 2 mm. With the 5-mm top and bottom end layers, a total height of each elastomer reached 52 mm. The cross-section of the bearings used in L1 and L2 bays is 250 mm by 400 mm while it is 150 mm by 250 mm in L3 bays. The details of the elastomeric bearing are shown in Figure 3.

3. VARIATION OF THE DYNAMIC PROPERTIES OF THE BRIDGE IN SIX YEARS

Aras [12] determined the dynamic properties of the Istanbul Medeniyet University Pedestrian Bridge by applying operational modal analysis principles by presenting a relatively wide-literature survey on the modal testing of similar structures. The measurements had been recorded on 20 July 2017 at 34 °C ambient temperature and under 2 people/minute of human traffic. Three Kinemetrics, TSA-SMA accelerometers, with three sensors, were used for data collection. The linear acceleration range of each sensor is +-4 g. Each accelerometer has its data storage unit and works separately without a mutual data acquisition system.

Aras [12] has analyzed the recorded vibrations with the Matlab computer program [19] by simply representing each signal in the frequency domain. No filtering was applied to the data due to the high level of uncertainties related to the ambient sources of vibration like wind, vehicle traffic, and pedestrian-induced vibrations. Modal identification was performed between 0 Hz and 10 Hz which is considered adequate for the identification of the studied bridge. The mode shapes of the bridge in the vertical direction have been reported as illustrated in Figure 4 [12]. It is seen that, independent from the adjacent bays, each bay of the bridge formed its mode. The first dominant frequency of L1, L2, and L3 bays were reported as 2.99 Hz, 6.30 Hz, and 12.38 Hz, respectively.

Six years after Aras [12], the dynamic properties of the bridge were studied again with the same measurement equipment, analysis procedure, and under similar environmental conditions. The vibration measurements recorded on 12 July 2023, at 33 °C temperature and approximately 2 people/minute of traffic have been analyzed. Figure 5 shows the vibration recording while Figure 6 illustrates the FFT presentation of the signals recorded on each bay of the bridge. The first dominant frequency of L1, L2, and L3 has been determined as, 3.00 Hz, 6.29 Hz, and 11.63 Hz. A comparison of these values to those obtained by Aras [12] proves that the frequency of L1 bay has increased 0.01 Hz, the frequency of L2 bay has decreased 0.01 Hz, and the frequency of L3 bay has decreased 0.75 Hz. The frequency difference, 0.01 Hz, detected for L1 and L2 bays is such a small value that can stem from uncontrolled and unaccounted effects such as wind or vehicle traffic. For this reason, it can be concluded that the dynamic properties of L1 and L2 bays have not changed over the period of six years. However, a frequency drop, reaching 0.75 Hz is not a usual decrease. Detailed investigation for the frequency decrease and a regular structural health monitoring plan is suggested for the future of the bridge.

MODE 1 – Z, f = 2.99 Hz, oscillation of L_1 girders

MODE 2 – Z, f = 6.30 Hz, oscillation of L_2 girders

MODE 3 – Z, f = 12.38 Hz, oscillation of L_3 girders
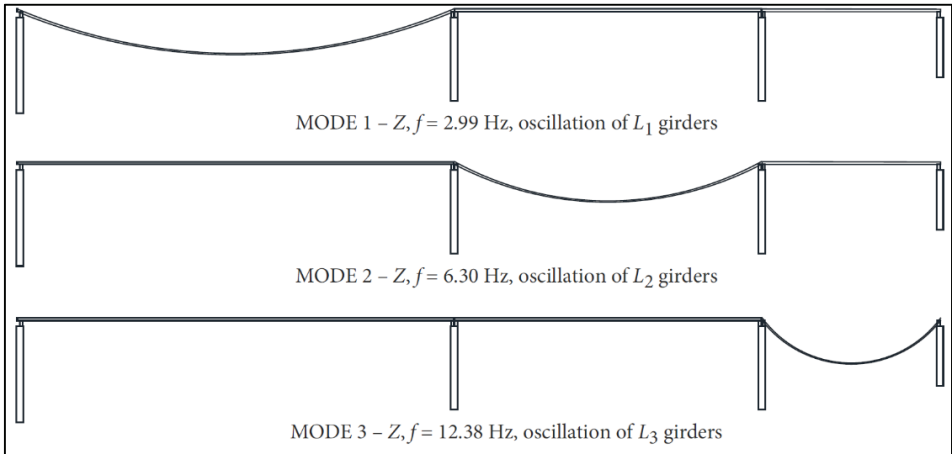
Figure 4 - Determined mode shapes of three-bay bridge on 20.07.2017 at 34 °C [12]

Figure 5 - Vibration recording and accelerometer
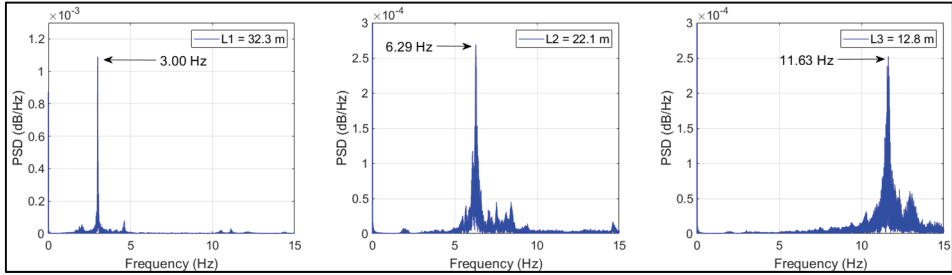
Figure 6 - FFT representations of the vertical accelerations recorded on L1, L2 and L3 bays on 12.07.2023 at 31 °C

4. MODAL TESTING TO REVEAL THE TEMPERATURE EFFECTS IN THE DYNAMIC PROPERTIES

Starting from 30 July 2021 to 30 June 2022, eleven measurements have been recorded from the mid-point of the longest bay of the bridge during the daytime under its normal function. The coldest date was 21 December 2021 at 5 °C and the hottest date is 30 July 2021.

The details of the measurements and analyses are the same as reported in the previous part. Since the amplitude of the vibration affects the dominant frequencies, the data recorded under rare human traffic have been used for the assessment. In this condition, the maximum acceleration reached 0.02 m/s^2 in the longest span. Figure 7 shows the acceleration data recorded at 33 °C. Figure 8 shows the dominant frequencies of the longest bay of the bridge obtained via the measurements recorded at 33 °C, 19 °C, and 5 °C.

Since the measurements were taken from the central location of the span, the out-of-horizontal plane mode could not be determined. For this reason, the vertical mode of the longest span of the bridge can be represented by a single dominant frequency. Figure 9 shows the relationship between the determined dominant frequencies and ambient temperature.

The dominant frequency of the longest span of the bridge varies between 2.98 and 3.11 Hz. The increase in temperature decreases the dominant frequencies. The ratio of the frequencies on the coldest day to the hottest day is 1.044. When the temperature range is widened, the ratio gets higher. The variation of the dominant frequencies has been linked to the decrease in the elastic modulus of the construction materials with an increase in the temperature by Ni et al. [4]. The authors investigated the amount of decrease in the dominant frequencies of the bridge cables made of steel and bridge deck made of concrete. A more evident decrease in the dominant frequencies of cables than that of the bridge deck was shown as one possible proof for their conclusion since steel is more sensitive to temperature variation than concrete. The obtained results also showed that the temperature–frequency relation is close to linear. It is seen that the temperature sensitivity of the dynamic properties of the studied bridge is similar to those of cable-stayed bridges tested by Ni et al. [4].
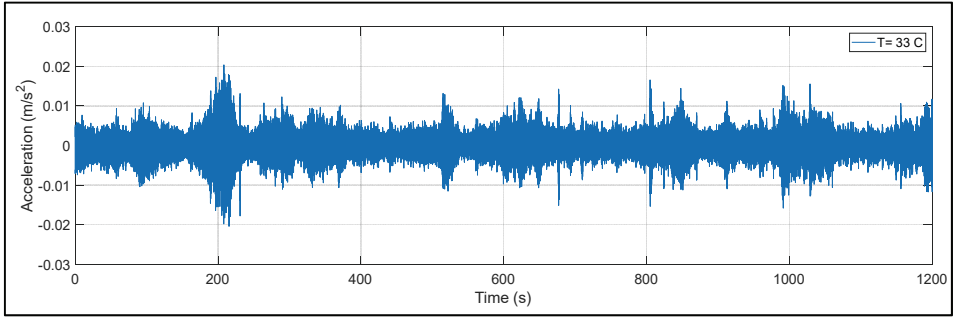
Figure 7 - Acceleration record used to determine the dominant frequency of longest span of the bridge to study temperature effect
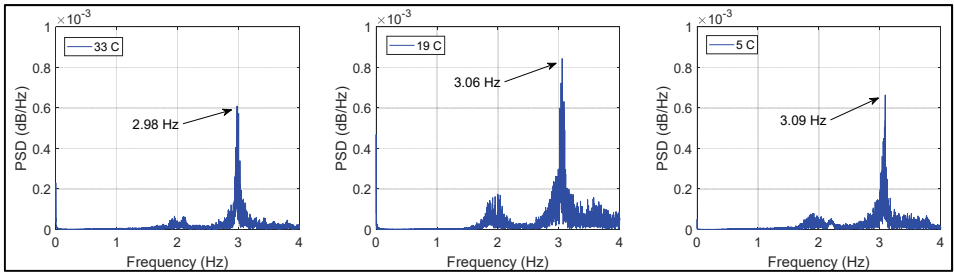
Figure 8 - FFT representations of the accelerations recorded at 33, 19 and 5 °C temperature
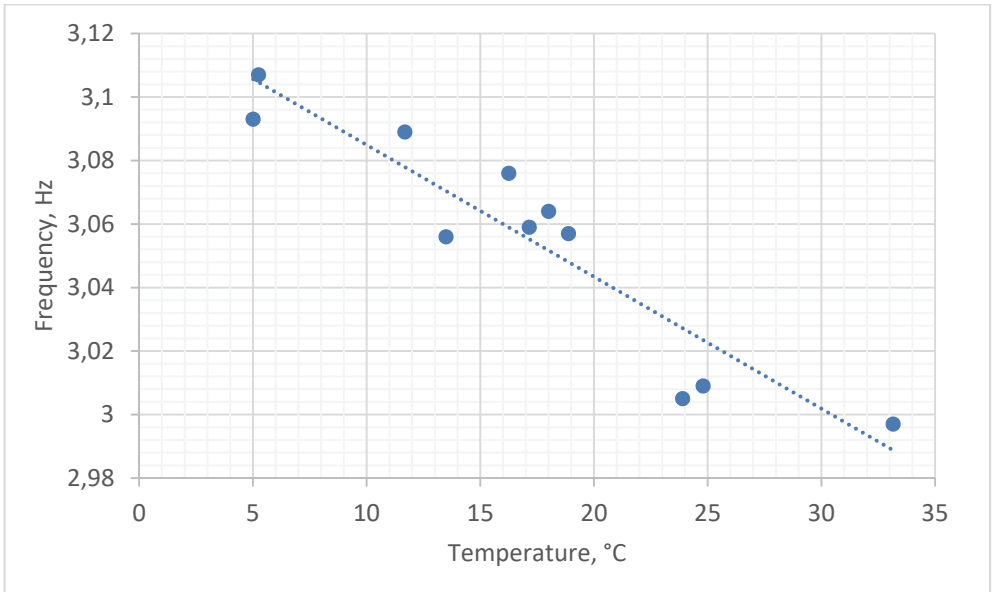
Figure 9 - Determined dominant frequencies and the temperature measured when the signal was recorded

5. INVESTIGATION OF HUMAN-INDUCED VIBRATIONS IN THE DYNAMIC PROPERTIES OF THE BRIDGE

The human-induced vibrations have been applied on the longest bay of the bridge as jumping protocols performed by the students of INS471 Structural Health Monitoring Laboratory course at 16.3 °C. The tests have been performed during normal service conditions. Therefore, the vibrations have been recorded under specifically created human vibrations and those created by pedestrians using the bridge to cross the motorway.

Figure 10 - Application of jumping protocol with five students on point J1
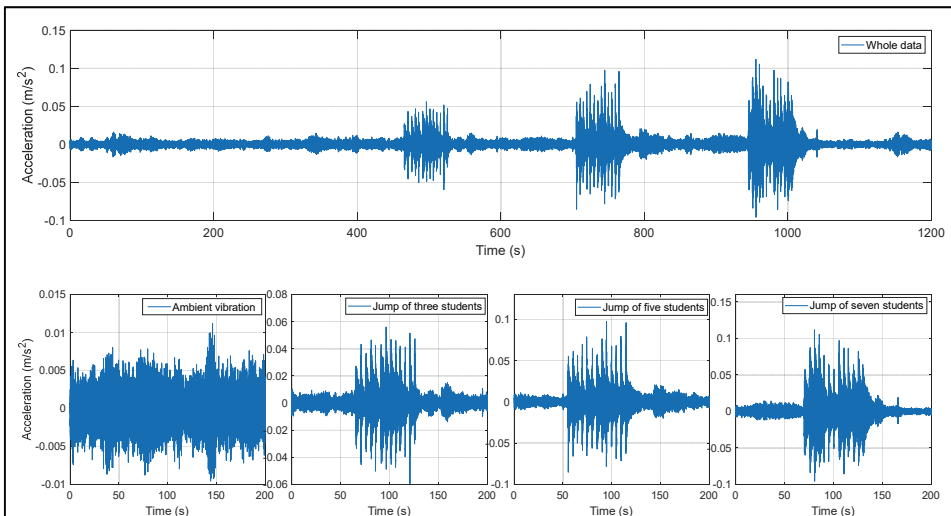
Figure 11 - Recorded vibrations during the jump of three, five and seven students on point J1

Six different jumping protocols have been applied on the bridge as the jumping of three, five, and seven students on point J1 and points J1 and J2 together. As can be seen in Figure 2, points J1 and J2 are located at the quarter-length of L1 measured from P1, pier, and A1, abutment, respectively. At each set, a group of students jumped at a five-second interval for a minute. Figure 10 shows the application of the jumping protocol on J1 while Figure 11 shows the recorded vibrations.

The acceleration record has been taken for 20 minutes which also includes the three jumping protocols. The increase in the magnitude of the acceleration has been seen as the result of the jumping. In ambient conditions, the maximum acceleration is about 0.011 m/s². The jump of three, five, and seven students increased it to 0.06 m/s², 0.1 m/s², and 0.11 m/s² respectively.

To see the variation of dominant frequencies, FFT analyses have been performed for the segmented signals with a length of 200 seconds shown in Figure 9. The dominant frequencies of the bridge were obtained as shown in Figure 10 under different levels of human-induced vibrations. It is also noted that the peak at around 2 Hz seen under ambient vibrations has vanished for the analyses under different jumping actions. The disappearance of the peak proves the bridge has no dynamic mode at around 2 Hz frequency and it must be ignored.
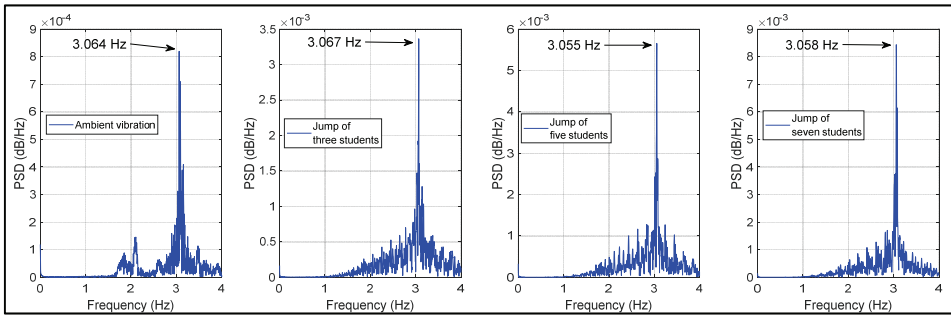
Figure 12 - Obtained dominant frequencies for the portion of the ambient case, the jump of three, five and seven students on Bridgepoint J1

Figure 13 - Application of jumping protocol with five students on points J1 and J2

Figure 13 shows the application of the jumping protocol with two groups of five students on J1 and J2 together while Figure 14 shows the recorded vibrations. As in the previous measurement set, the magnitude of the vibration has increased. In ambient conditions, the maximum acceleration is about 0.015 m/s^2. The jump of three, five, and seven students on J1 and J2 together increased it to 0.09 m/s^2, 0.14 m/s^2, and 0.12 m/s^2 respectively. Unexpectedly, the maximum acceleration measured for the jump of seven students on J1 and J2 points of the bridge is lower than that measured for the jump of five students on J1 and J2 of the bridge. The main reason may be the ordinary human traffic, which uses the bridge for crossing the motorway. Since the measurements have been recorded under normal traffic conditions, the analyses include the effects of ordinary human traffic as well.
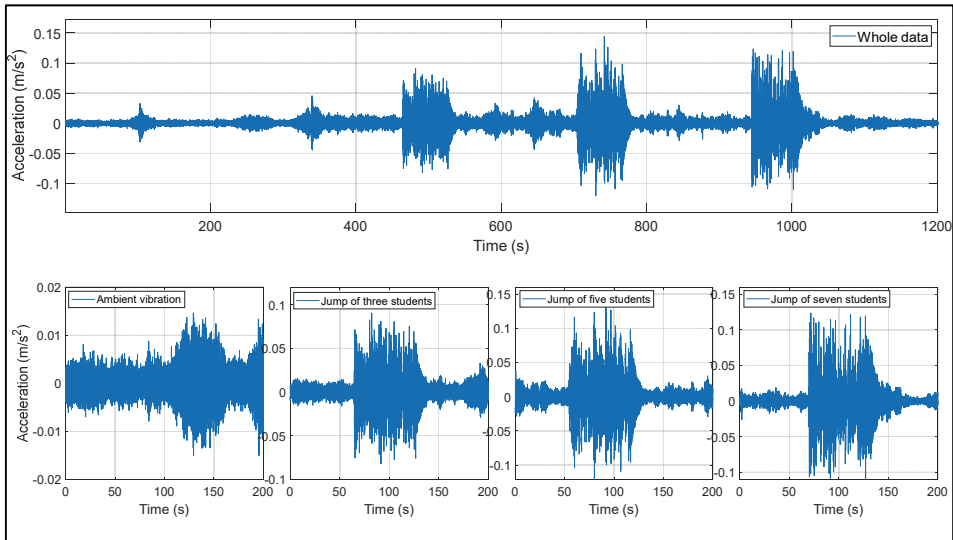
Figure 14 - Recorded vibrations during the jump of three, five and seven students on points J1 and J2
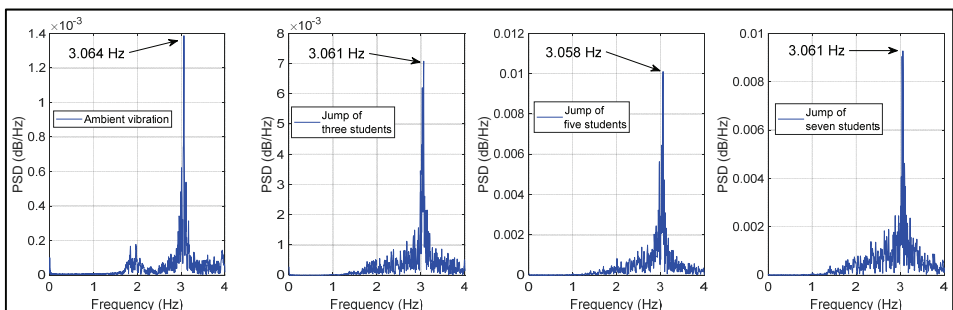
Figure 15 - Obtained dominant frequencies for the portion of the ambient case, the jump of three, five and seven students on points J1 and J2

33

Figure 15 shows the presentation of the signals shown in the second row of Figure 14 in the frequency domain. For the ambient part of the signal, the dominant frequency of the bridge has been determined as 3.064 Hz while for the jumps of three, five, and seven students on points J1 and J2, they have been extracted as 3.061 Hz, 3.056 Hz, and 3.061 Hz, respectively.

Figure 16 and Figure 17 show the relationship between the extracted dominant frequencies and the maximum magnitude of the acceleration and the Power Spectral Density of the signal at the dominant frequency, respectively. They contain the data in Figure 12 and Figure 15. Besides 100-second signal segments from the ambient parts and human-induced vibrations have been analyzed and their results are included in Figure 16 and Figure 17. The FFT analyses of 100-second signals, containing the 60-second human-induced vibration have resulted in raised signal power at the dominant frequency reaching 0.019 dB/Hz as can be seen in Figure 17. It is seen that the trend lines in Figure 16 and Figure 17 have such a small amount of negative slope that, the amplitude of the vibration does not affect the dominant frequency of the studied bridge.

The performed literature survey showed that the relationship between the magnitude of vibration and the dominant frequencies of the studied type of bridges has not been studied. However, the study performed by Ni et al. [9] can be interpreted to control the validity of the obtained result. Ni et al. [9] conducted field tests on a pedestrian bridge at the City University of Hong Kong (CityU) under (i) ambient conditions, (ii) forced with known pseudorandom excitation, (iii) forced with frequency resonant excitation and (iv) free vibration. Despite the difference in the maximum magnitude of the vibration in the acceleration time history of each test and the obtained dominant frequencies for the modes, no relation was grasped between the magnitude of the vibration and dominant frequencies. Hence, it is seen that the obtained results in this study are compatible with the results obtained by Ni et.al. [9].
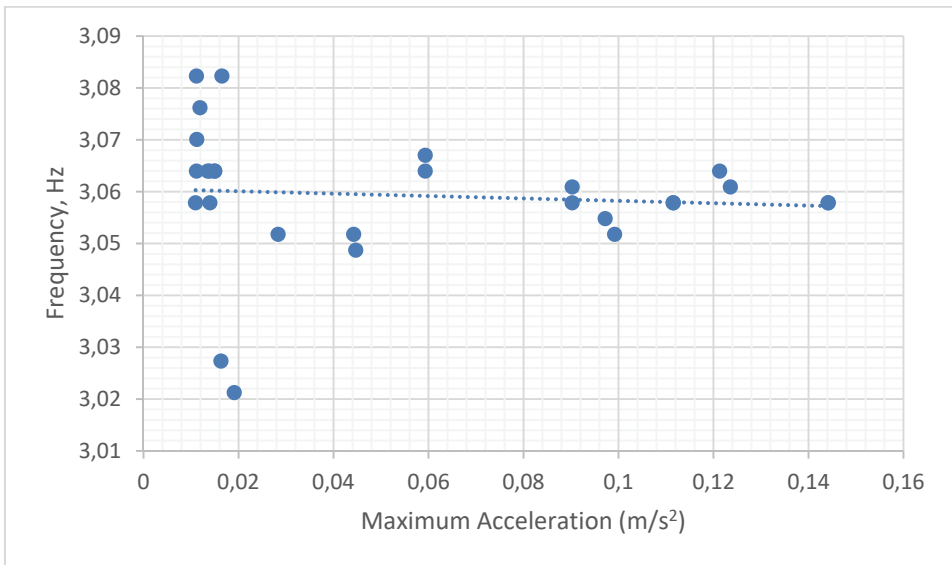
Figure 16 - Variation of dominant frequency with respect to maximum magnitude of the acceleration
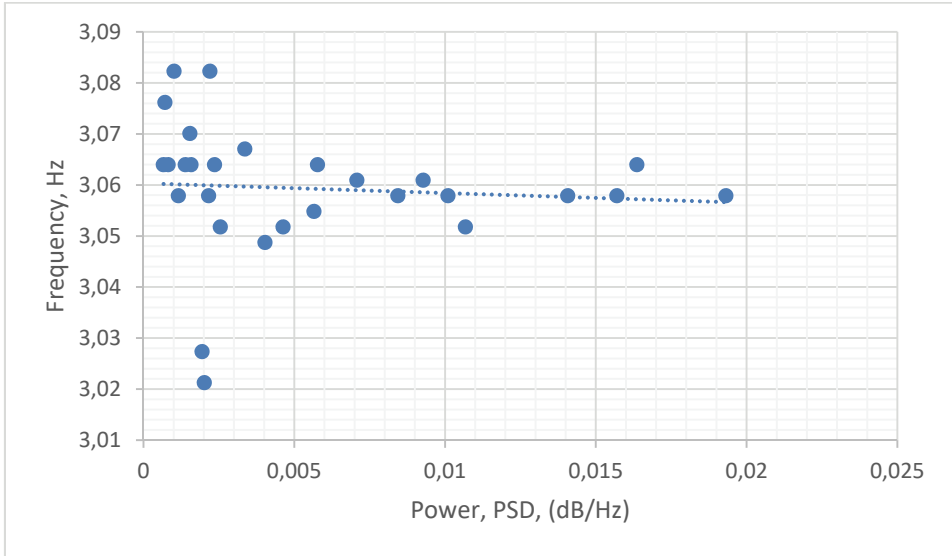
Figure 17 - Variation of dominant frequency with respect to Power Spectral Density (PSD) of the signal at the dominant frequency

6. VIBRATION SERVICEABILITY ASSESSMENT OF THE BRIDGE

Human comfort level is the main parameter setting the serviceability assessment. Živanović et al. [20] pointed out the acceleration response of the bridges as the best parameter to assess their serviceability due to its success in describing people's vibration perception. Indeed, the assessment in the codes is based on the indices derived from the acceleration response of the bridges. In this respect, a serviceability control has been performed in this study.

The vibration serviceability assessment of footbridges in the current codes, i.e., ISO 10137 [21], Eurocode 5 [22], BS 5400 [23], , and Setra [24] have been summarized by Dong et al. [25]. While ISO 10137 employs Root Mean Square (RMS) of the frequency-weighted accelerations, the others use the peak value of the acceleration response. Dong et al. [25] converted the RMS value of ISO 10137 [21] to an equivalent acceleration peak value by multiplying with $\sqrt{2}$ to present a comparative view. Finally, they illustrated the serviceability control of pedestrian bridges according to the mentioned codes in Figure 18 [25] (courtesy of corresponding author F. N. Çatbaş). As it is seen acceleration limits of BS 5400 and ISO 10137 are frequency dependent while Eurocode 5 sets a constant value, 0.7 m/s^2, for serviceability control. Setra [24] defines three serviceability degrees as extreme, medium, and low serviceability and assigns constant acceleration limits as 0.5 m/s^2, 1 m/s^2, and 2.5 m/s^2, respectively for each. The area under the lines is acceptable for the defined serviceability level and the area above the line is unacceptable.

The measurement presented for the longest span of the bridge indicates its frequency as 3 Hz while the maximum acceleration is determined as 0.145 m/s^2 under the combination of the jumping scenario and normal human traffic. This value proves the serviceability of the bridge

according to all mentioned codes and it satisfies the maximum comfort level according to Setra [24]. During the measurement, human vibration perception has also been assessed. A person, standing on the midpoint of the bay and concentrating on feeling the vibration, sensed it while another one walking through the bridge could not.
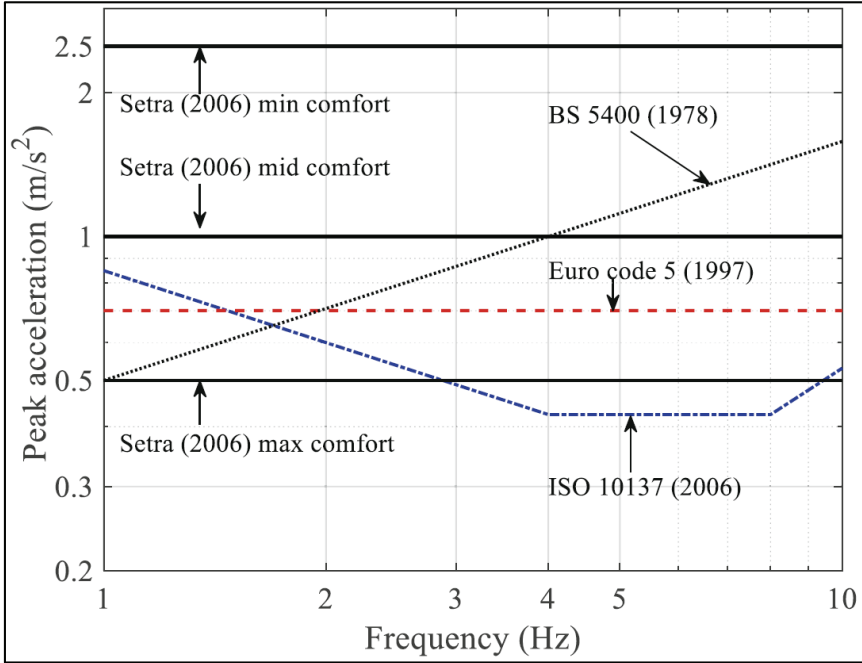
Figure 18 - Acceleration limits for vibration serviceability assessment of pedestrian bridges in different codes [25]

7. CONCLUSION

Operational modal analysis-based dynamic investigations have been applied to a 32.3-meter-long, isolated, precast, and pre-stressed pedestrian bridge in Istanbul. The tests aimed to see if the dominant frequencies of the bridge have changed during the six years of service life after its construction. Besides, the effects of the ambient temperature and human-induced vibrations in its dynamic properties were investigated. Finally, the vibration serviceability of the bridge was checked. The findings showed that;

- For the bridge's six-year service life, the dominant frequency of L1 and L2 bays has not changed while that of L3 has decreased 0.75 Hz. A regular structural health monitoring plan and detailed inspections are suggested for the future of the bridge.

- There is a strong dependency between the ambient temperature and dominant frequencies. The decrease in temperature increases the dominant frequencies. 28 °C temperature decrease (between 33 °C and 5 °C) resulted in a 4.4% dominant frequency increase.

- Human-induced vibrations do not cause a significant change in the dominant frequency of the studied bridge. This shows that the dominant frequencies of the studied bridge are independent from the magnitude of the vibration.

- The vibration serviceability control showed that the bridge satisfies the serviceability requirements of different codes.

Acknowledgement

References

[1] Ni, Y. Q., Hua, X. G., Fan, K. Q., and Ko, J. M. (2005). "Correlating modal properties with temperature using long-term monitoring data and support vector machine technique." Engineering Structures 27, 1762–1773.

[2] Catbas, F. N., Susoy, M., and Frangopol, D. M., (2008). "Structural health monitoring and reliability estimation: long span truss bridge application with environmental monitoring data." Engineering Structures. 30(9), 2347–59.

[3] Mosavi, A. A., Seracino, R., and Rizkalla, S. (2012). "Effects of temperature on daily modal variability of a steel-concrete composite bridge." Journal of Bridge Engineering 17(6). doi.org/10.1061/(ASCE)BE.1943-5592.0000372

[4] Ni, Y. C., Alamdari, M. M., Ye, X. W., and Zhang, F. L. (2021). "Fast operational modal analysis of a single-tower cable-stayed bridge by a Bayesian method," Measurement 174: 109048.

[5] Sohn, H., Dzwonczyk, M., Straser, E. G., Kiremidjian, A. S., Law, K. H., and Meng, T. (1999). "An experimental study of temperature effect on modal parameters of the Alamos Canyon Bridge." Earthquake Engineering and Structural Dynamics 28(8), 879–97.

[6] Peeters, B., and De Roeck, G. (2001a). "One-year monitoring of the Z24-Bridge: environmental effects versus damage events." Earthquake Engineering and Structural Dynamics, 30(2), 149–71.

[7] Ni, Y. Q., Zhou, H. F., and Ko, J. M. (2009). "Generalization Capability of Neural Network Models for Temperature-Frequency Correlation Using Monitoring data." Journal of structural engineering 135(10), doi.org/10.1061/(ASCE)ST.1943-541X.0000050

[8] Tubino, F., Carassale, L., and Piccardo, G. (2016). "Human-induced vibrations on two lively footbridges in Milan," Journal of bridge engineering, 21(8), C4015002

[9] Ni, Y. C., Zhang, F. L., and Lam, H. F. (2016). "Series of Full-Scale Field Vibration Tests and Bayesian Modal Identification of a Pedestrian Bridge. 21(8), C4016002. https://doi.org/10.1061/(ASCE)BE.1943-5592.0000857

[10] Moutinho, C., Pereira, S., and Cunha, A. (2020). "Continuous dynamic monitoring of human-induced vibrations at the Luiz I Bridge." Journal of Bridge Engineering, 25(8), 05020006 https://doi.org/10.1061/(ASCE)BE.1943-5592.0001580

[11] Chen, G. W., Chen, X., and Omenzetter, P. (2020). "Modal parameter identification of a multiple-span post-tensioned concrete bridge using hybrid vibration testing data." Engineering Structures 219, 110953, https://doi.org/10.1016/j.engstruct.2020.110953

[12] Aras, F. (2018). "Modal testing of an isolated overpass bridge in its construction stages. The Baltic Journal of Road and Bridge Engineering, 13(1), 67-76.

[13] Min, Z. H., and Sun, L. M. (2013). "Wavelet-based structural modal parameter identification." Structural Control and Health Monitoring, 20, 121-138. https://doi.org/10.1002/stc.474

[14] Peeters, B., and De Roeck, G. (2001b). "Stochastic system identification for operational modal analysis: a review." Journal of Dynamic Systems, Measurement, and Control, 123(12), 659-667. https://doi.org/10.1115/1.1410370

[15] B. Sevim, A. Bayraktar, A.C. Altunışık, S. Atamtürktür, F. Birinci, Finite element model calibration effects on the earthquake response of masonry arch bridges, Finite Elements in Analysis and Design 47 (2011) 621–634

[16] A.C. Altunışık, A. Bayraktar, B. Sevim, H. Özdemir, Experimental and analytical system identification of Eynel arch type steel highway bridge, Journal of Constructional Steel Research 67 (2011) 1912–1921.

[17] Michel, C., Gueguen, P., and Bard, P-Y. (2008). "Dynamic parameters of structures extracted from ambient vibration measurements: An aid for the seismic vulnerability assessment of existing buildings in moderate seismic hazard regions." Soil Dynamics and Earthquake Engineering, 28, 593-604. https://doi.org/10.1016/j.soildyn.2007.10.002

[18] Oruç, B,, Sarıkaya, A., and Küçük, Y. E. (2016). "Medeniyet University pedestrian overpass detailed design calculation report". Prepared for the Ministry of Transport, Maritime Affairs and Communications, Ankara.

[19] Matlab. (2012). The MathWorks, Inc., Natick, Massachusetts, United States.

[20] Živanović S, Pavic A and Reynolds P. (2005). "Vibration serviceability of footbridges under human-induced excitation: A literature review". J Sound Vib 2005;279:1–74. https://doi.org/10.1016/j.jsv.2004.01.019.

[21] ISO 10137 (2007). "Bases for design of structures -serviceability of buildings and walkways against Vibrations, 2nd ed.". International Organization for Standardization, Geneva, Switzerland.

[22] ECS. Eurocode 5, (1997). "Design of timber structures—part 2: bridges (ENV 1995-2)". European Committee for Standardization; 1997.

[23] BS 5400 (1978) "Steel, Concrete and Composite Bridges—Part 2: Specification for Loads". British Standards Association, London.

[24] Setra, Footbridges (2006). "Assessment of Vibrational Behavior of Footbridges Under Pedestrian Loading" (Technical guide), Paris; 2006.

[25] Dong C-Z, Baş S. and Catbas F.N. (2020) "Investigation of vibration serviceability of a footbridge using computer vision-based methods". Engineering Structures, 224, 111224.

High Temperature Effect on the Engineering Performance of Pumice Added Sand-Bentonite Mixtures

Esra GUNERI[1*]
Yeliz YUKSELEN-AKSOY[2]

ABSTRACT

Soils surrounding energy geo-structures must perform for long periods of time under high temperatures and thermal cycles. Engineering properties of soils are affected by temperature. Pumice is a thermally durable material and it may be used to increase thermal durability of soils. For this reason, it was aimed to develop thermally durable soil material by adding pumice additive to sand-bentonite mixtures. 10% and 20% pumice were added to 10% and 20% sand-bentonite mixtures and compaction, consolidation, direct shear and hydraulic conductivity tests were performed. The direct shear and hydraulic conductivity tests were performed both at room temperature and 80 °C. The consolidation test results showed that as pumice content was increased the total vertical deformation decreased at room temperature. Pumice additive reduced the maximum shear stress values when temperature increased for 10B-90S mixtures. However, the pumice additive increased the internal friction angle of the mixtures at high temperature. It was observed that the hydraulic conductivity increased with increasing temperature. Thermal conductivity measurements showed that pumice additive reduced the thermal conductivity value of the mixtures.

Keywords: Consolidation, permeability, pumice, sand-bentonite, strength, high temperature.

1. INTRODUCTION

The thermal behavior of soils has gained importance because of increase in number and type of energy geo-structures such as energy piles, nuclear waste repositories, waste handling facilities, electricity transmission and gas pipelines. The buffer (bentonite, bentonite-sand) barrier, which is used as a sealing material at underground depot for high-level radioactive waste, is exposed to high temperatures. Hence, change in hydraulic and mechanical properties of buffer is a matter to be considered in the design of nuclear waste repositories.

Moreover, the buffer material is needed which keeps its engineering parameters unchanged under different thermal conditions especially in nuclear waste repositories.

Previous studies have shown that engineering properties of clayey soils change under high temperatures [1]. High temperature alters soil physico-chemical properties; hydro-mechanical properties as well [2, 3]. Increase in temperature of saturated fine-grained soils to a level lower than the boiling point of water affects the permeability, compressibility and shear strength behavior [4]. Thermal effects on shear strength, stiffness and yielding behavior can be attributed to the volume change of soil [5]. The temperature increase in fine grained soils such as clay and unsaturated soils can cause permanent changes in volume [6, 7, 8, 9, 10]. The over-consolidated clays show the elastic expansion behavior, while the normally consolidated soil exhibits elasto-plastic thermal shrinkage (contraction) during heated consolidation [6, 7, 10, 11, 12, 13]. Also at same dry density, high temperature significantly reduces the swelling pressure of clayey soil, while diminishing swelling capacity vaguely [14].

The shear strength of the normally consolidated (NC) clay increases with increasing soil temperature [15]. For example, the axial stress in the peak deviatoric stress was lower than that of the specimen at elevated temperature for the sample that subjected to temperature history prior to shearing. However, the slope of the shear strength envelope is independent of temperature [15]. The heated normally consolidated clay showed contraction during the direct shear test. The reason for this behavior is thought to be the hardening of the clay during heating [16].

Previous studies have shown that hydraulic conductivity increased with increasing temperature [14, 17, 18]. The properties of pore water vary depending on temperature and viscosity of the liquids passing through the porous structure of soils [15]. In addition, the structural interaction of soil with water is also important.

In liner applications, due to the low hydraulic conductivity, bentonite is mixed with sand and used as a reinforced filling material with high thermal conductivity and stiffness [1]. Sand-bentonite mixture is more preferred as a filling material because of its low permeability and high swelling properties [19]. Pumice is an amorphous aluminum silicate formed as a result of volcanic activities. Chemical structure of pumice includes SiO_2, Al_2O_3, Fe_2O_3, CaO, MgO, Na_2O, K_2O. Aluminum oxide in the chemical structure of pumice is known to provide high heat resistance [20]. Due to its high heat resistance it can be used to improve engineering properties of soils under high temperatures. Pumice's spongy structure is formed by the outflow of gas from sudden cooling during pumice formation [21]. Since the gaps in the porous structure of the pumice are independent of each other, it is a material with low hydraulic conductivity [22]. The pumice does not undergo any volume changes below 760 °C and does not enter the chemical reaction with any acid other than hydrofluoric acid. Already the dissolution rate of pumice in an acid is maximum 2.9% [23, 24]. It was determined that the pumice samples had a glassy structure and when they were heated up to 850 °C, no thermal reactions occurred in their structure and the pumice did not undergo a structural deterioration [22].

Because of superior thermal features of pumice, the addition of pumice to sand-bentonite mixtures may improve the thermal durability of soils against high temperatures. The thermal durability defines the ability of soils to maintain their engineering properties unchanged

under temperature cycles or high temperatures. It is known that many properties of soils change such as compressibility, shear strength, hydraulic conductivity under temperature cycles and high temperatures. This change depends on many parameters such as soil type, rate of temperature increase, exposure time to temperature. In the present study, it was aimed to improve engineering properties of sand-bentonite mixtures with pumice additive. To this end; compaction, consolidation, direct shear and hydraulic conductivity tests were performed on the pumice added sand-bentonite mixtures. The direct shear and hydraulic conductivity tests were carried out both under the room and high temperature (80 °C). The effect of pumice and high temperature were analyzed.

2. MATERIAL CHARACTERIZATION AND TEST METHODS

2.1. Material Characterization

In this study, sand-bentonite mixtures were prepared with pumice additive. Pumice was supplied from local supplier. The used bentonite sample was Na-bentonite. According to the results of sieve analysis 20.7% of the sand is fine material. The sand was sieved through No.6 sieve. Sand and bentonite samples were oven dried at 105 °C for 24 hours before being used in the experiments. Pumice was used as it is (without drying) in order to keep its natural state since the natural water content of the pumice was very low, it was not subjected to drying process, however at each experiment the initial water content of pumice (2-3%) was determined and this amount of water was taken into account. The mixtures were prepared by adding pumice to sand-bentonite mixtures in two different bentonite ratios of 10% and 20%. The pumice additive was determined by weight as 10% and 20% of the total dry weight. The mixtures without pumice additives are referred as 10B-90S and 20B-80S, respectively. The physico-chemical properties of the materials were given in Table 1. The bentonite sample passed through No.200 sieve. The grain size distributions of bentonite, pumice and sand are given in Figure 1.

The X-Ray diffraction (XRD) analyses were performed in the focusing geometry from 0° to 89°, with a scanning speed at 0.1° 2θ/s and radiation at 60 kV, 5-60 mA on Thermo Scientific ARL X'TRA X-Ray diffraction equipment. The XRD analysis results of bentonite and pumice samples were given in Figure 2. According to the results, the calcium silicate, sodium calcium aluminum silicate was observed in the pumice sample. The bentonite sample contains montmorillonite, quartz and illite minerals.

Table 1 - The physico-chemical properties of the materials

Property	Material		
	Bentonite	Sand	Pumice
Specific gravity	2.70	2.63	2.50
Liquid limit (%)	476.0	-	37.0
Plastic limit (%)	70.0	-	Non-plastic
pH	9.50	-	8.86
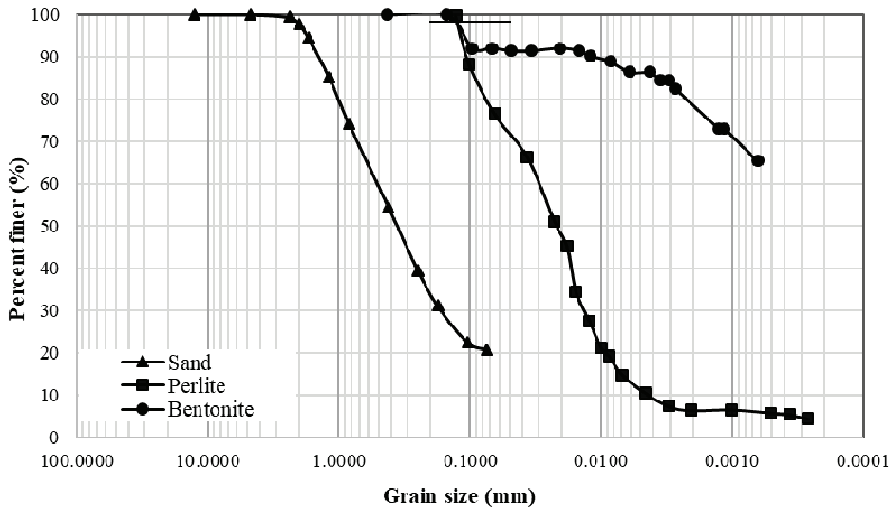
Figure 1 - Grain size distribution curves of bentonite, pumice and sand
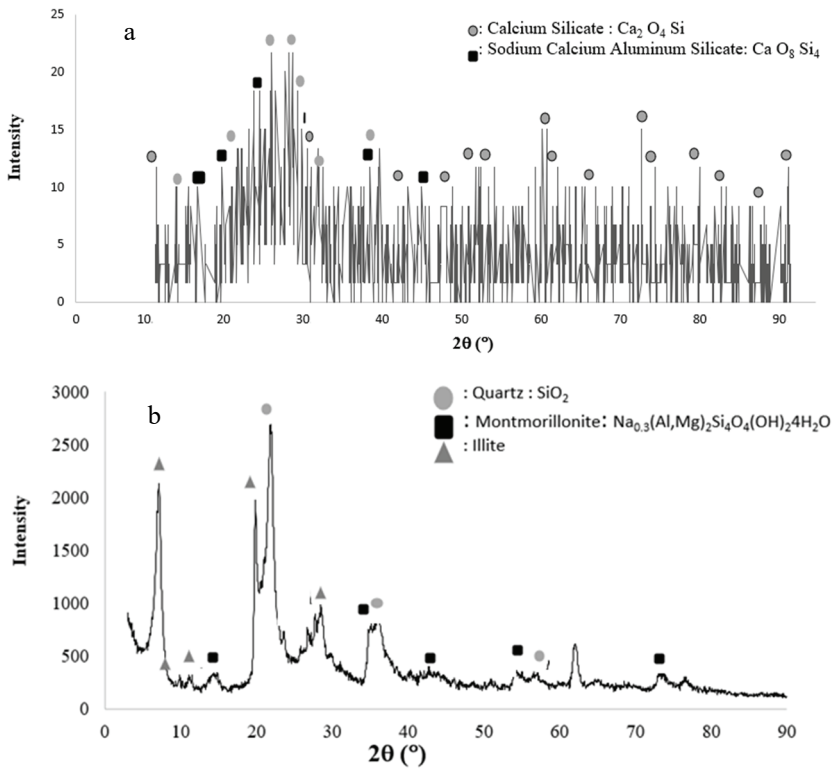
*Figure 2 - The X-Ray diffraction analysis (XRD) results of the samples
a) pumice, b) bentonite*

The scanning electron microscope (SEM) photos of the samples were taken with COXEM EM-30 Plus device. The samples were compacted at their dry unit weight and $w_{opt}+2\%$ water content then they were freeze-dried at least 24 hours in order to prevent shrinkage.

2.2. Test Methods

The samples were prepared by adding 10% and 20% pumice to 10B-90S and 20B-80S mixtures. The 10% and 20% of the total weight of the mixture was weighed as pumice, the remaining dry weight was sand-bentonite mixture. The water added and samples were mixed homogenously and they were kept in a closed container for 24 hours to ensure that the water was homogeneously dispersed in the mixture. For the compaction tests, samples were prepared in four different water contents and Standard Proctor Test was performed according to ASTM D698 [25].

The oedometer test samples were compacted at the 2% wet side of the optimum water content (w_{opt}) corresponding to the maximum dry unit weight (γ_{dmax}). The samples were kept under seating pressure (6.86 kPa) for 24 hours. The consolidation tests were performed to according to ASTM D2435 [26]. The load increment ratio (LIR) was 1.0 (24.5, 49, 98, 196, 392 and 784 kPa). After the completion of the loading stage, unloading stage was initiated. At the unloading stage the loads were decreased from 784 kPa to 196 kPa, then to 49 kPa.

Direct shear tests were performed according to ASTM D3080 [27]. The dry samples were mixed in a vessel until becomes homogeneous. Water was added to these mixtures so that the water content was at 2% wet side of the optimum water content. Each sample was compacted into three layers in the 6x6cm molds. The molds were kept submerged in a container for 24 hours. It should be noted that the water contents of the 10B-90S and 20B-80S samples were increased from 15% to 22.7% and 19.5% to 27.0%, respectively at the end of this process. The initial water contents of the samples increased and changed between 22.7-32.7% at the beginning of the tests. The initial water contents of the samples are given in Table 4. While the samples were kept in water, weight was placed on them to prevent swelling. After 24 hours, the mold was placed in the shear box and cell was filled with water. Three different normal stresses (49, 98, 196 kPa) were applied in the direct shear experiments and samples were consolidated and sheared under these stresses.
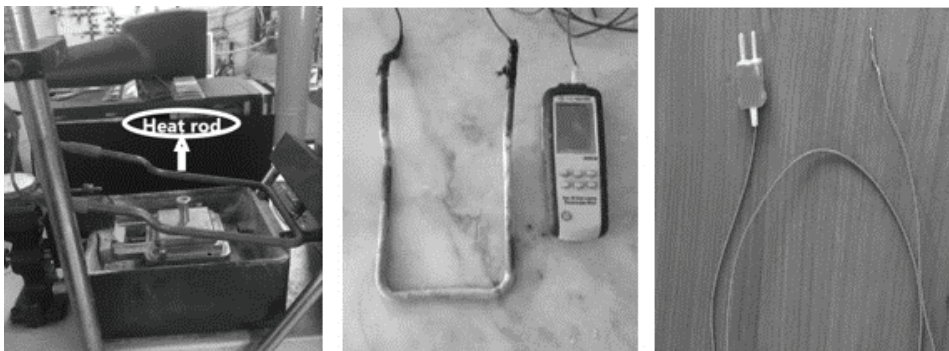
Figure 3 - Temperature controlled direct shear test equipment

The direct shear experiments were conducted under two different temperatures, at room temperature and 80 °C. The water in the shear box was heated with specially designed heat rod (Figure 3). The temperature of the water in the cell was kept constant at 80 °C by help of thermostat. Two K-type thermocouples and a digital thermometer measured and recorded the temperature of the water and soil sample (Figure 3). At the end of the experiments, the samples were placed in an oven at 105 °C to determine the water content.

Hydraulic conductivity tests were carried out according to ASTM D5084 [28] using flexible wall permeameters. The samples were kept in airtight plastic bags for 24 hrs. In order to compact samples with less energy, the samples were compacted at γ_{dmax} and $w_{opt}+2\%$ water content. The hydraulic conductivity tests were performed in two different temperatures: room temperature and 80 °C. During the tests, the temperature was provided using heat rod (Figure 4).
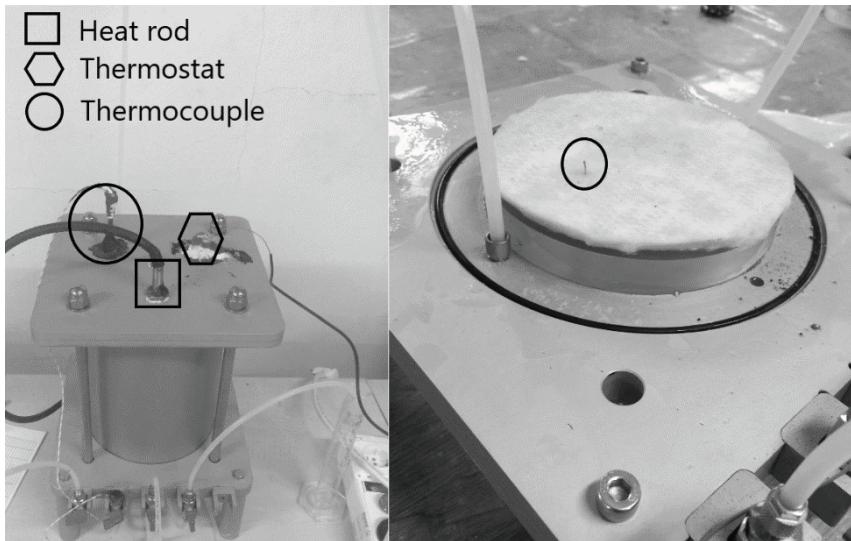
Figure 4 - Hydraulic conductivity test set-up

The soil was heated by heating the water in the cell. The deterioration in the structure of plexiglass cells, fragmentation or rupture may occur under high temperature. For that reason, the outer cell of flexible wall permeameters were made of aluminum in order to prevent temperature negative effects on the plexi-glass material. There were three separate holes at the top of the permeameter cell, for heat rod, thermostat and thermocouple. A hole was drilled in the bottom geotextile large enough for the thermocouple to pass through. With the use of geotextile in hydraulic conductivity tests, it was ensured that the soil sample was not dragged during the water flow. The water flow was distributed homogeneously on the sample by using geotextile. The thermocouple was inserted through a valve of the permeameter through this hole and soil temperature measurement was supplied. The temperature of the water was measured from the top of the permeameter cell with a thermocouple placed in the cell. Two thermocouples were connected to the digital thermometer and temperature values were recorded depending on time. With the help of a thermostat, the water temperature inside the

cell was kept at 80 °C. The hydraulic conductivity values of the mixtures were expressed in terms of pore volume of the flow. Thermal cycling was applied on the 8B-72S-20PU sample. The test was initiated under room temperature, a cycle was carried out by gradually increasing the temperature (25-50-80 °C) and then gradually lowering (80-50-25 °C) it back to room temperature. At each temperature level, the test was continued until the flow became stable.

The thermal conductivity values of sand-bentonite mixtures in the presence of pumice were measured with Shotherm QTM device. The ambient temperature indicated by the device during the measurements was recorded between 20~22°C. The samples were prepared and compacted at the same saturation degree. The samples were grouped into two groups. According to the bentonite content the sample properties especially optimum water content values became different. One of them was 10B-90S mixture and 10%-20% additives and the other 20B-80S mixture and 10%-20% additives. The void ratio and saturation degree values of the mixtures were determined, and then the samples were prepared at that water content. According to each group the average saturation degree values were obtained and the samples were prepared at their group saturation degree value. The samples kept closed in a plastic bag for 24 hours in order to distribute the water homogeneously in the mixture. The amount of samples to be compacted into the molds was calculated and the number of impacts was determined by trial and error. The needed number of impact was determined for each layer. All samples were compacted in the same compaction scheme. Then samples were compacted in three layers and 104 drops in a 12x12x4 cm^3 mold. Measurements were made from five different regions of each sample (Figure 5). The thermal conductivity values were determined by taking the average of these values.
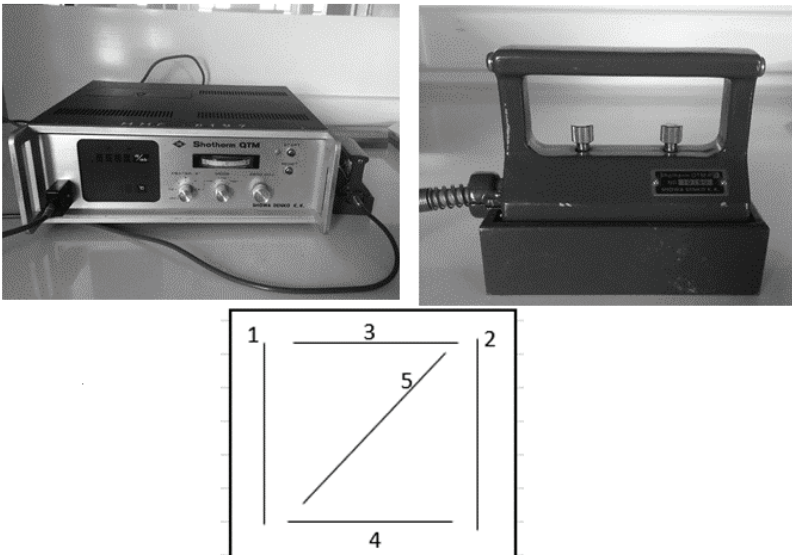
Figure 5 - Thermal conductivity equipment and measurement directions

3. RESULTS AND DISCUSSION

3.1. Compaction Test Results

The Standard Proctor tests were performed on the 10% and 20% bentonite-sand mixtures in the presence of 10% and 20% pumice additives. The compaction test results showed that the γ_{dmax} of 10% bentonite-sand mixture was 16.7 kN/m^3, then it decreased to 16.2 kN/m^3 and 15.6 kN/m^3 in the presence of 10% and 20% pumice, respectively (Table 2). It should be noted that, the γ_{dmax} of the pumice was determined to be 12.9 kN/m^3. The low dry unit weight value is a reason of decrease in dry unit weight values of bentonite-sand mixtures. On the other hand, pumice additive changes the w_{opt} values insignificantly. The maximum dry unit weight and optimum water content values were used in order to prepare compacted samples for oedometer and direct shear tests.

Table 2 - Compaction parameters of the 10% and 20% sand bentonite mixtures

Mixtures	Max. dry unit weight (kN/m^3)	Optimum water content (%)
100 PU	12.9	30.0
10B-90S	16.7	15.5
9B-81S-10PU	16.2	17.0
8B-72S-20PU	15.6	16.0
20B-80S	15.6	17.5
18B-72S-10PU	15.2	17.0
16B-64S-20PU	14.7	17.0

3.2. Volume Deformation of the Pumice Added Sand-Bentonite Mixtures Under Room Temperature

The oedometer tests were conducted and the volume deformation behavior of sand-bentonite mixtures in the presence of pumice were observed. The vertical strain (ε) versus logarithmic effective stress (σ') curves of the 10B-90S, 20B-80S mixtures and pumice were given in Figures 6 and 7. The total vertical deformation value of the 10B-90S mixture and 100% pumice were 4.6% and 4.0%, respectively. In the presence of 10% pumice additive of 10B-90S mixture, the vertical deformation value was determined as 3.7% and increased to 5.9% when the pumice content was increased to 20%. The vertical deformation value of 20B-80S mixture was found to be 10.1%. The vertical deformation values decreased to 17.1% and 16.7% with 10% and 20% pumice contents. According to the results, pumice additive increased the vertical deformation amount under room temperature.

The compression index (C_c) is an important parameter used to estimate the consolidation settlement. As can be seen in Table 3, as the pumice content was increased, the total deformation of the mixtures increased for 20B-80S mixtures.
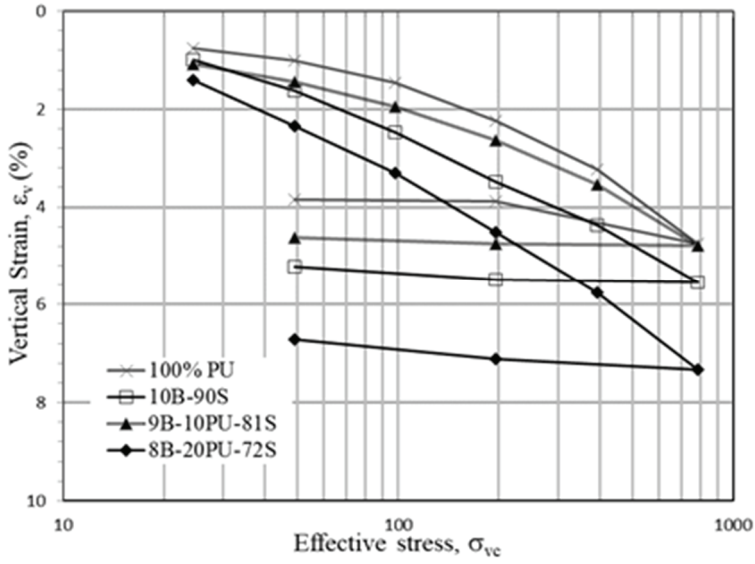
Figure 6 - ε-log σ' curves of 10B-90S mixtures with pumice additives under room temperature
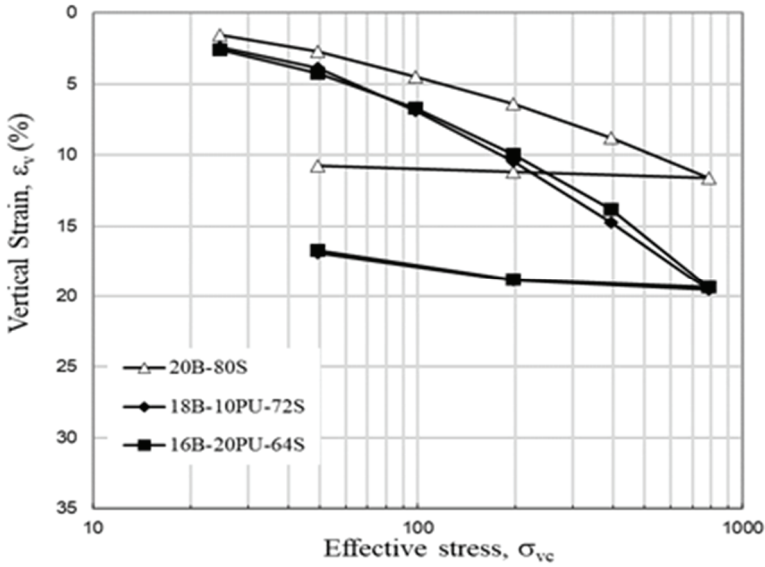
Figure 7 - ε-log σ' curves of 20B-80S mixtures with pumice additives under room temperature

Table 3 - C_c values of the 10% and 20% bentonite-sand mixtures with pumice additive

Sample	Compression index (C_c)
Pumice	0.083
10B-90S	0.056
9B-81S-10PU	0.056
8B-72S-20PU	0.079
20B-80S	0.153
18B-72S-10PU	0.265
16B-64S-20PU	0.259

3.3. Shear Strength Parameters of Sand-Bentonite Mixtures Under High Temperature

The 10% and 20% pumice were added to the 10B-90S and 20B-80S mixtures and direct shear tests were performed under room and high temperatures. It was observed that while the drained internal friction angle (ϕ') of the 10B-90S mixture at room temperature was 32.7°, it decreased to 31.5° under high temperature (80 °C). The ϕ' values did not change with 10% pumice but increased to 36.7° with 20% pumice content under room temperature. When 10% and 20% pumice were added to 10B-90S mixtures under high temperature, ϕ' values increased to 34.1° and 34.7°, respectively. It was observed that the ϕ' values increased as pumice was added for 10B-90S mixture under high temperature. The maximum shear stress value was 106.9 kPa of 10B-90S mixture at room temperature (Figure 8). Generally, the shear stress values of 10B-90S mixtures decreased slightly when temperature was increased from room temperature to 80 °C. In addition, maximum shear stress (τ_{max}) values of the 10B-90S mixture in the presence of 10% and 20% pumice additives increased by approximately 10 kPa under high temperature. Generally, increase in shear strength is reported as temperature increases. However, some studies reported decrease in shear strength depending on temperature increase. For example, as a result of unconsolidated-undrained (UU) and consolidated-undrained (CU) tests at 20, 50, 80 and 110 °C for a Boom clay, a significant decrease in strength was determined when the temperature increased [29]. Similarly, it was reported that temperature affects density and viscosity of water, a decrease in the strength of clayey soil sample and silt under 60 °C was determined [30]. Opposite to these findings, other studies have shown that the internal friction angle is not affected by temperature and the shear strength of soils reaches higher values when the specimens are heated [7]. According to the former studies, it is obvious that the changes on the shear strength depends on the soil mineralogy, stress and temperature levels, etc.

The internal friction angle of the 10B-90S mixture increased both at room and high temperatures in the presence of 20% pumice, while 10% pumice additive caused a slight increase only under high temperature (Figure 8). This effect also reflected on the shear strength and affected the maximum shear stress (10% pumice, 102.9 kPa and 20% pumice, 103.8 kPa) values to a negligible extent. Table 5.5 shows the internal friction angle and cohesion values of the 10B-90S and 20B-80S mixtures in the presence of 10% and 20% pumice additives.
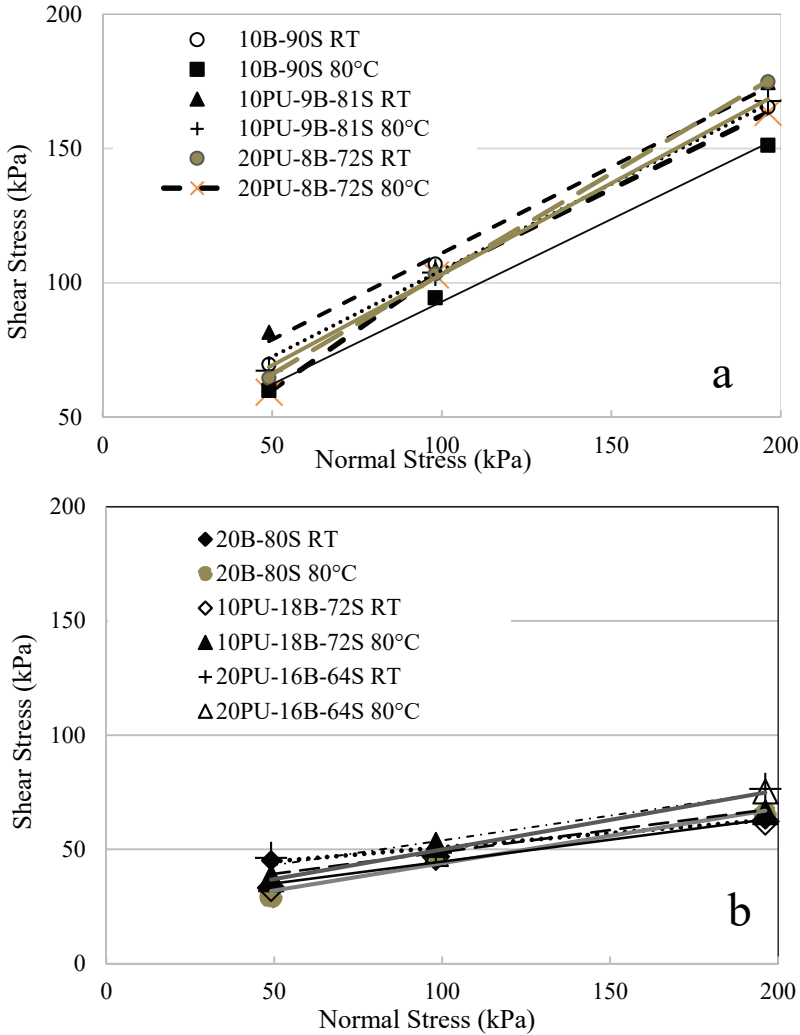
Figure 8 - Shear stress-normal stress relationship of sand-bentonite mixtures at room and high temperatures in the presence of 10% and 20% pumice additive a) 10B-90S, b) 20B-80S

Direct shear tests results of 20B-80S mixtures showed that pumice additive increased the internal friction angle values under room temperature. The ϕ' value of the 20B-80S mixture at room temperature was 7.0°, while this value increased to 11.1° and 12.2° with 10% and 20% pumice additives, respectively. The cohesion (c') value decreased with both 10% and 20% pumice addition to the 20B-80S mixtures under room temperature (Table 4). Under high temperature, the addition of 10% pumice reduced the internal friction angle from 13.6° to 11.6°. In contrast, the addition of 20% pumice increased the internal friction angle to 14.5°.
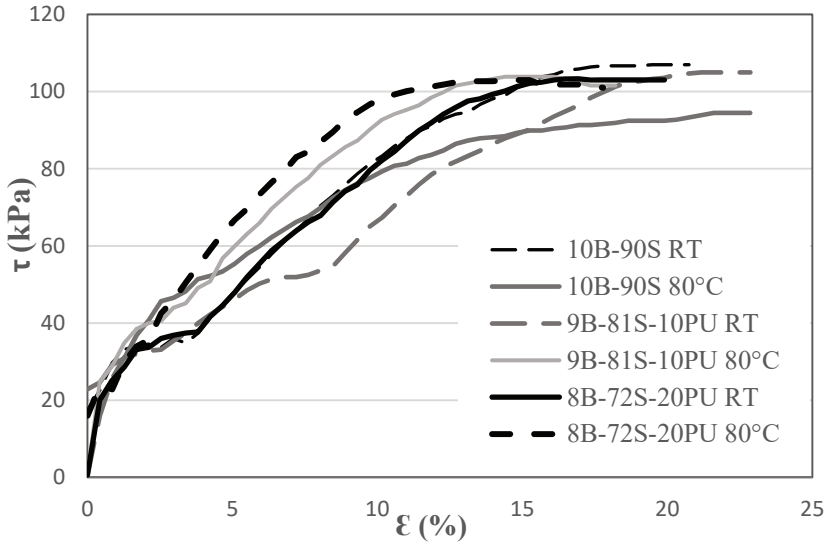
Figure 9 - τ- ε relationship of of 10B-90S mixtures under 98.1 kPa
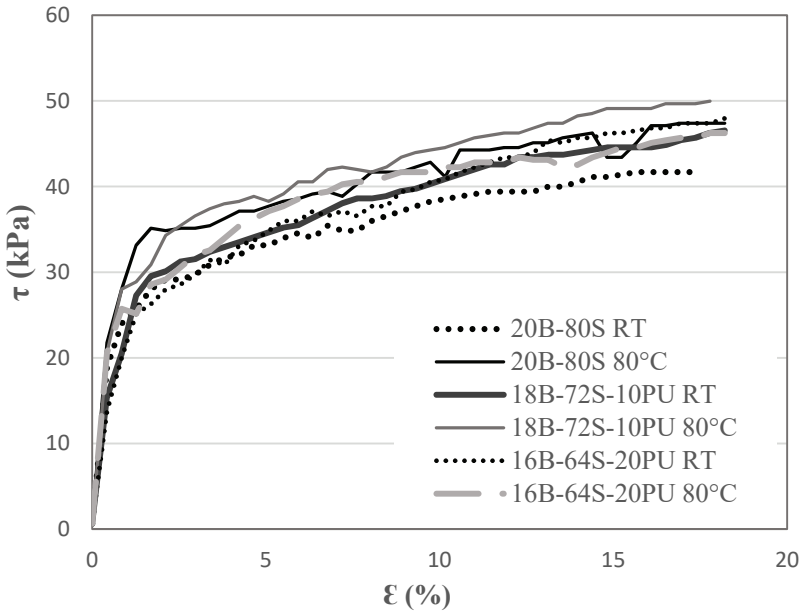
Figure 10 - τ- ε relationship of of 20B-80S mixtures under 98.1 kPa

The maximum shear stress values slightly increased for 20B-80S mixtures when temperature was increased from room temperature to 80 °C. However, it should be noted that the ϕ' values increased in the presence of 20% pumice additives under high temperature (Figure 9 and 10). The test results of the same mixtures are shown in Guneri and Yukselen Aksoy (2020) [31]. The tests on the same samples were repeated on the new device with new calibration. The angle of internal friction values did not change however cohesion values changed with compared to previous test results.

Table 4 - The shear strength parameters of the mixtures

Mixtures	Initial water content	Room Temperature		80 °C	
	w (%)	ϕ' (°)	c' (kPa)	ϕ' (°)	c' (kPa)
10B-90S	22.7	32.7	40.4	31.5	31.5
9B-81S-10PU	23.8	32.7	46.8	34.1	35.4
8B-72S-20PU	25.7	36.7	28.7	34.7	29.1
20B-80S	27.0	7.0	38.5	13.4	20.0
18B-72S-10PU	28.3	11.1	25.4	11.6	29.7
16B-64S-20PU	32.7	12.2	32.2	14.5	24.0
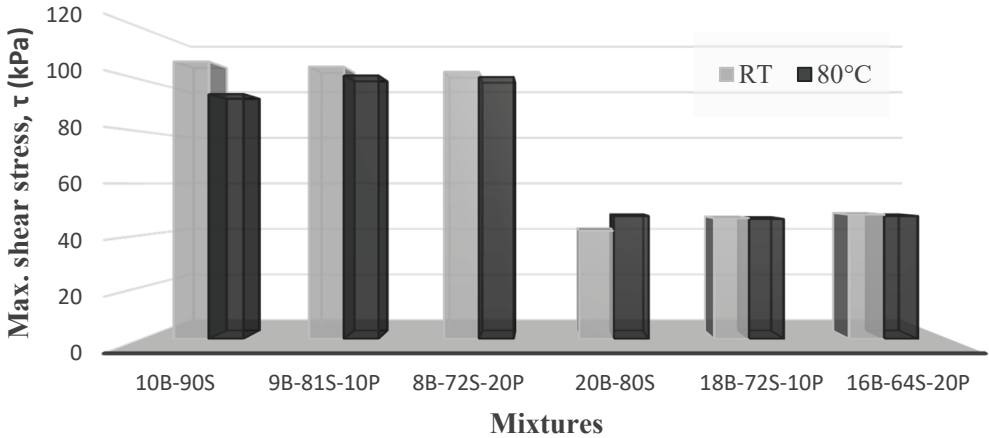
Figure 11 - Maximum τ_{max} values for all mixtures under room temperature and 80 °C (under 98.1 kPa)

The results have shown that pumice contributes to the shear strength of sand-bentonite mixtures under high temperature. Pumice has silanol (Si-OH) groups on its surface and this silanol group binds hydroxyl groups at the edges of the clay platelets [10]. As a result, the pumice is held by the clay surface and positive charge increase on the clay surface. Hence,

shear strength of bentonite increases. Another reason is when pumice is added to the sample, both the bentonite and sand content of the mixture decrease. With the decrease in the amount of bentonite, the shear strength increases.

The maximum shear stress values under room and high temperature for all mixtures were given comparatively in Figure 11. For all 10B-90S mixtures, the maximum shear stress value decreased with increase in temperature; however, τ_{max} values of 20B-80S mixtures increased under high temperature. According to the results obtained, the maximum shear stress decreased as pumice additive was added to 10B-90S mixtures at room temperature, while the addition of pumice to 10B-90S mixtures increased the shear stress values under high temperature. In 20B-80S mixtures, while the maximum shear stress increased with 10%-20% pumice at room temperature, only the maximum shear stress of 10% pumice added mixture increased at high temperature.

3.4. Hydraulic Conductivity Tests under High Temperature

The hydraulic conductivity (k) tests on the 10B-90S mixture under room and high temperature in the presence of 10% and 20% pumice were conducted. The water temperature was gradually increased to 25, 50 and 80 °C. The measured soil temperatures corresponding to these water temperature values were determined as approximately 20, 40 and 60 °C, respectively. Hydraulic conductivity tests were expressed as the pore volume of flow. Inflow and outflow amounts were recorded during the tests and Q_{out}/Q_{in} values were between 0.75 and 1.25. The dashed lines show the 0.75 and 1.25 Q_{out}/Q_{in} values, respectively. Figures 12 and 13 show the hydraulic conductivity-pore volume of flow graphs of 10B-90S mixtures in terms of hydraulic conductivity-pore volume of flow in the presence of 10% and 20% pumice additive. Temperature versus k values of the 9B-81S-10PU mixture are given in Table 5. When the water temperature was increased from 25 to 50 °C, the k value increased 4.5fold and followed by when temperature was increased from 50 to 80 °C the k value increased 1.5fold. The results showed that the hydraulic conductivity of the mixture increased with increasing temperature. This is mainly due to the decrease in the viscosity of the water as the temperature increases. However, it was reported structural changes in the body of soil may cause change in hydraulic conductivity as well [13].
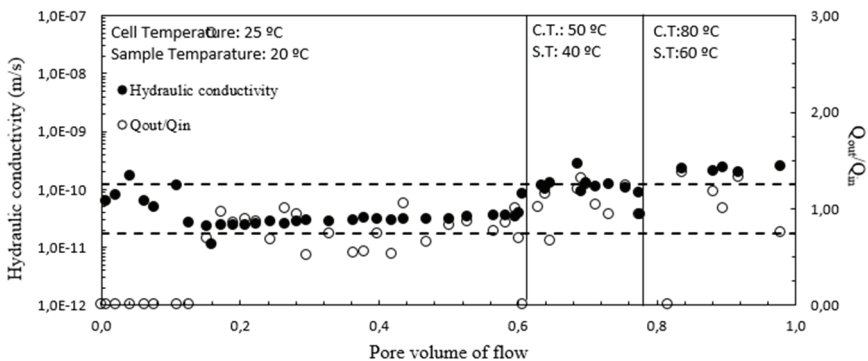
Figure 12 - Hydraulic conductivity graph in terms of pore volume of flow for 9B-81S-10PU mixture

Table 5 - The change of hydraulic conductivity values of the 9B-81S-10PU mixture with the temperature

Temperature (°C)	k (m/s)
25	$3.1×10^{-11}$
50	$1.4×10^{-10}$
80	$2.1×10^{-10}$

Table 6 shows the hydraulic conductivity values of the 8B-72S-20PU mixture under high temperature and temperature cycles. As mentioned above, the hydraulic conductivity increased with increase in temperature. Although the hydraulic conductivity values decreased when the sample was cooled (returned to room temperature), it could not return to the initial hydraulic conductivity value. This is explained not only by the change in water viscosity but also structural changes in bentonite [14, 17, 18].
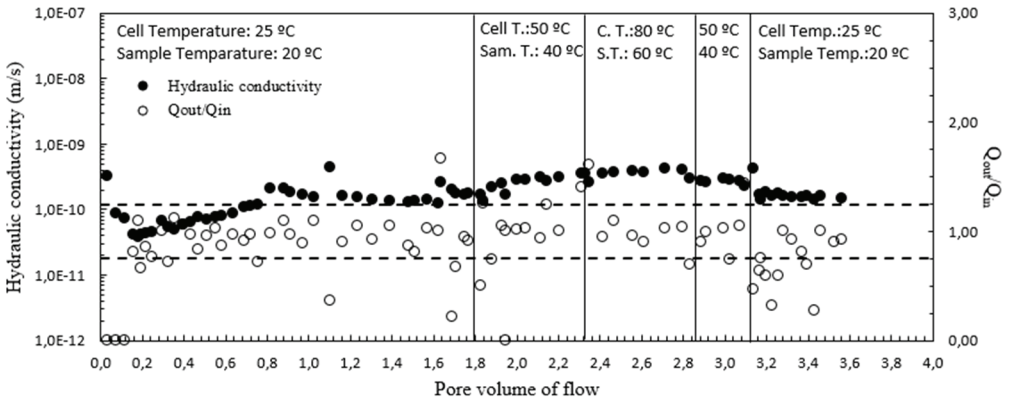
Figure 13 - Hydraulic conductivity graph in terms of pore volume of flow for 8B-72S-20PU mixture

Table 6 - The change of hydraulic conductivity values of the 8B-72S-20PU mixture with the temperature cycle

Temperature (°C)	k (m/s)
25	$1.4×10^{-10}$
50	$2.0×10^{-10}$
80	$3.8×10^{-10}$
50	$2.9×10^{-10}$
25	$1.6×10^{-10}$

3.5. Thermal Conductivity

The thermal conductivity values of 10B-90S mixtures and 20B-80S mixtures were measured in the presence of 10% and 20% pumice. The thermal conductivity value of 100% pumice was measured to be 0.878 W/mK. Thermal conductivity values of additive free (sand-bentonite) mixtures were higher than this value, and as the pumice added to the mixtures, the conductivity value of the mixtures decreased (Table 7). In the nuclear waste repositories double layer model was used by [32]. Near canister there is a thermally conductive barrier. However, in order to protect host rock there is a need for a thermally insulating layer.

Table 7 - The measured thermal conductivity values of the mixtures

Mixtures	Thermal Conductivity (λ, W/mK)
10B-90S	1.779
9B-81S-10PU	1.588
8B-72S-20PU	1.426
20B-80S	1.461
18B-72S-10PU	1.950
16B-64S-20PU	1.776
100PU	0.878

Previous studies show that sand can reduce the shrinkage of clay to a certain extent [33] and increase the thermal conductivity [1, 16]. In this case, it is expected that the thermal conductivity value of the 10B-90S mixture should be higher than the 20B-80S mixture. As the pumice additive was increased the thermal conductivity of the mixture decreased, indicating that pumice, which is already used in thermal insulation, can be used as a thermal insulating barrier.

Previous studies report that the thermal conductivity of the mixture increases as the percentage of sand increases. However, in one study it is shown that, depending on the sample's dry density and water content, the thermal conductivity may remain constant or even decrease with the increase of the sand content (at values above the limit value it will reach) [34]. In this case, the thermal conductivity value of the 10B-90S mixture is expected to be higher than the 20B-80S mixture. While measurement results based on the constant void ratio and saturation degree support this behavior.

3.6. Scanning Electron Microscope (SEM) Analyses

The SEM photos of the pumice samples which were prepared under room and 80 °C temperatures were taken. The flake shaped particles of the pumice can be seen clearly from the SEM photo in Figure 14. The gaps in the structure of pumice increase its water adsorption capacity [35]. But at the same time, its hollow structure reveals that any liquid that will pass through it can find a way in the mixture and provide a transition to the fluid and cannot have a reducing effect on hydraulic conductivity.
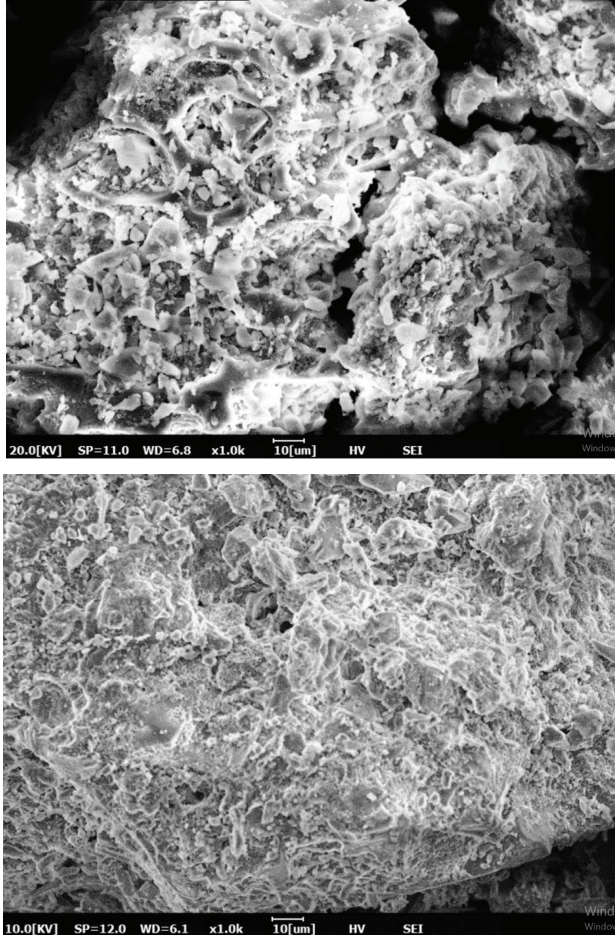
Figure 14 - Scanning electron microscope photos of the samples (x1000) (a) pumice sample at room temperature, (b) pumice sample at 80 °C

4. CONCLUSIONS

In the present study, compaction, consolidation, shear strength and hydraulic conductivity behaviors of pumice-added sand-bentonite mixtures were investigated. The shear strength and hydraulic conductivity behavior of the mixtures were also investigated under high temperature. The compaction test results showed that the addition of pumice reduced the maximum dry unit weight values of the 10B-90S and 20B-80S mixtures due to the very low dry unit weight of the pumice. The optimum water content values did not change significantly. The pumice addition to the 20B-80S mixtures decreased vertical deformation. However, this effect was not observed in 10B-90S mixtures. According to the direct shear test results, maximum shear stress values decreased when the temperature increased from room temperature to 80 °C for 10B-90S mixtures. On the other hand, the maximum shear

stress of 20B-80S mixtures generally increased with the effect of high temperature. The angle of internal friction values of mixtures generally increased under high temperature in the presence of pumice. Hydraulic conductivity test results show that as temperature increased, the hydraulic conductivity increased. The test results of 8B-72S-20PU with thermal cycling showed that the hydraulic conductivity decreases with cooling and at the end of thermal cycling the sample hydraulic conductivity value did not return to its initial value. The thermal conductivity values of the mixtures were measured and it was determined that the pumice additive reduced the thermal conductivity value of the mixtures.

In line with all this data, it was observed that the hydraulic conductivity values of the 20B-80S mixture exceeds the barrier limit value (1×10^{-11} m/s) for nuclear waste repositories or municipal solid waste landfills. However, the bentonite amount can be increased in the mixture in order to maintain the hydraulic conductivity limits. Considering the thermal conductivity values, the pumice additive increases the insulating property. Besides the thermally insulative characteristic of the pumice, it has the positive contributions to the engineering properties of the sand-bentonite mixtures. For that reason, pumice and a material thermally conductive like graphite can be used together. Also, it can be used as a second layer (in double layer systems) in order to protect the host rock. The pumice additive has a positive effect on compression behavior of 20B-80S mixtures. In terms of shear strength pumice additive can be used for increasing shear strength of 20B-80S mixtures under high temperatures.

Symbols

C_c	is the compression index
ϕ	is the internal friction angle
c	is the cohesion
τ_{max}	is the maximum shear stress
σ'	is the effective stress
ε	is the strain
k	is the coefficient of permeability
λ	is the value of thermal conductivity
100PU	is the 100% pumice
10B-90S	is the 10% bentonite and 90% sand mixture
20B-80S	is the 20% bentonite and 80% sand mixture
9B-81S-10PU	is the 9% bentonite, 81% sand and 10% pumice mixture
8B-72S-20PU	is the 8% bentonite, 72% sand and 20% pumice mixture
18B-72S-10PU	is the 18% bentonite, 72% sand and 10% pumice mixture
16B-64S-20PU	is the 16% bentonite, 64% sand and 20% pumice mixture

References

[1]   Zheng, L., Rutqvist, J., Birkholzer, J. T. and Liu, H. H., On the Impact of Temperatures up to 200°C in Clay Repositories with Bentonite Engineer Barrier Systems: A Study with Coupled Thermal, Hydrological, Chemical, and Mechanical Modeling. Eng. Geol., Volume 197, 2015.

[2]   Kale, R. C., Ravi, K., Influence of Thermal Loading on Index and Physicochemical Properties of Barmer Bentonite. Appl. Clay Sci., Volume 165, 2018.

[3]   Karnland, O., Bentonite Swelling Pressure in Strong NaCl Solutions. Correlation between Model Calculations and Experimentally Determined Data. 1997.

[4]   Laloui, L., Thermo-Mechanical Behaviour of Soils. Revue Française de Génie Civil. 5:6, 809-843, 2001. DOI: 10.1080/12795119.2001.9692328

[5]   Abuel-Naga, H.M., Bergado, D.T. and Bee Fong Lim., Effect of Temperature on Shear Strength and Yielding Behavior of Soft Bangkok Clay. Soils and Foundations. Volume 47, 3,423-436, 2007.

[6]   Campanella, R. and Mitchell, J., Influence of Temperature Variations on Soil Behavior. Journal of the Soil Mechanics and Foundations Division. 94, 609-734, 1968.

[7]   Cekerevac, C. and Laloui, L., Experimental Study of Thermal Effects on the Mechanical Behaviour of a Clay. International Journal for Numerical and Analytical Methods in Geomechanics. 28, 209-008, 2004.

[8]   Salager, S., Francois, B., Youssoufi, M. S. E., Laloui, L. and Saix, C., Experimental Investigations of Temperature and Suction Effects on Compressibility and Pre-Consolidation Pressure of a Sandy Silt. Soils and Foundations. 48, 4, 453-466, 2008.

[9]   Tang, A. M., Cui, Y. J. and Barnel, N., Thermo-Mechanical Behaviour of a Compacted Swelling Clay. Geotechnique. 58:1, 45-54, 2008.

[10] Uchaipichat, A., and Khalili, N., Experimental Investigation of Thermo-Hydro-Mechanical Behaviour of an Unsaturated Silt. Geotechnique. 59:4, 339-353, 2009.

[11] Coccia, C., Russell, J. and S. McCartney, J., Thermal Volume Change of Poorly Draining Soils I: Critical Assessment of Volume Change Mechanisms. Computers and Geotechnics. 80, 26-40, 2016. https://doi.org/10.1016/j.compgeo.2016.06.009.

[12] Cui, Y.J., Le, T.T., Tang, A.M., Delage, P. and Li, X.L., Investigating the Time-Dependent Behaviour of Boom Clay under Thermomechanical Loading. Geotechnique. 2009.

[13] Delage, P., Sultan, N. and Cui, Y.J., On the Thermal Consolidation of Boom Clay. Canadian Geotechnical Journal. Volume 37, 2012.

[14] Villar, M.V. and Lloret, A. Temperature Influence on the Mechanical Behaviour of a Compacted Bentonite. in Elsevier Geo-Engineering Book Series. Volume 2, 305-310, 2004.

[15] Abuel-Naga, H.M., Bergado, D.T., Ramana, G. V., Grino, L., Rujivipat, P. and Thet, Y. Experimental Evaluation of Engineering Behavior of Soft Bangkok Clay under Elevated Temperature. Journal of Geotechnical and Geoenvironmental Engineering. 132, 7, 2006.

[16] Yazdani, S., Helwany, S. and Olgun, G., Influence of Temperature on Soil–Pile Interface Shear Strength. Geomechanics for Energy and the Environment. 18, 69-78, 2019.

[17] Romero, E., Gens, A. and Lloret. A., Temperature Effects on the Hydraulic Behaviour of an Unsaturated Clay. Geotechnical and Geological Engineering. 19, 311–332, 2001.

[18] Towhata, I., Kuntiwattanaku, P., Seko, I. and Ohishi, K., Volume Change of Clays Induced by Heating as Observed in Consolidation Tests. Soils and Foundations. Volume 33, Issue 4, p. 170-183. 1993.

[19] Komine, H., Simplified Evaluation on Hydraulic Conductivities of Sand-Bentonite Mixture Backfill. Applied Clay Science. Volume 26, Issues 1–4, 13-19, 2004.

[20] Depci, T., Kul, A.R., Onal, Y., Disli, E., Alkan, S. and Turkmenoglu,. Z.F., Adsorption of Crystal Violet from Aqueous Solution on Activated Carbon Derived from Gölbaşi Lignite. Physicochemical Problems of Mineral Processing. 48, 1, 253-270, 2012.

[21] Sarıiz, K. and Nuhoğlu, İ., Endüstriyel Hammadde Yatakları ve Madenciliği. Eskişehir. Eskişehir. 1992

[22] Kılınç Aksay, E., İzmir-Menderes Yöresi Pomza Cevherinin Kullanımına Yönelik Teknolojik Özelliklerinin Araştırılması. Dokuz Eylül Üniversitesi. 2005.

[23] Gündüz, L., Sarıışık, A., Tozaçan, B., Davraz, M., Uğur, İ. and Çankıran, O., Pomza Teknolojisi (Pomza Karakterizasyonu). Isparta. 1998.

[24] Sezgin, M., Davraz, M. and Gündüz, L., Pomza Endüstrisine Sektörel Bakış. edited by L. Gündüz and V. Deniz. 2005.

[25] ASTM:D698-12. Standard Test Methods for Laboratory Compaction Characteristics of Soil Using Standard Effort. ASTM International. 2012.

[26] ASTM International. 2011. ASTM D2435 / D2435M - 11: Standard Test Methods for One-Dimensional Consolidation Properties of Soils Using Incremental Loading.

[27] ASTM. 2011. D3080/D3080M-11. Standard Test Method for Direct Shear Test of Soils under Consolidated Drained Conditions. ASTM International.

[28] ASTM. 2001. ASTM D5084-16 'Standard Test Methods for Measurement of Hydraulic Conductivity of Saturated Porous Materials Using a Flexible Wall Permeameter. ASTM International.

[29] De Bruyn, D., Thimus, J.F., The influence of temperature on mechanical characteristics of Boom clay: the results of an initial laboratory programme. Eng. Geol., 41, 1 – 4, 117 – 126, 1996.

[30] Noble, C. A., Demirel, T., Effect Of Temperature On Strength Behavior Of Cohesive Soil. Proceedings of an International Conference Held at Washington, D.C., January 16 With the Support of the National Science Foundation, Issue 103, 204-219, 1969.

[31] Güneri, E, Yukselen-Aksoy, Y., Shear strength behaviour of sand-bentonite mixtures with pumice additivite under high temperature. E3S Web of Conferences. 205. 04004. 10.1051/e3sconf/202020504004, 2020.

[32] Xue Y., Sun D., Wang L., Xu Y., A Double-Layered Model For Near-Field Temperature In A Nuclear Waste Repository, Progress in Nuclear Energy, 133, 103646, ISSN 0149-1970, https://doi.org/10.1016/j.pnucene.2021.103646, 2021.

[33] Wersin, P., Lawrence H. J., Snellman, M., Impact of Iron Released from Steel Components on the Performance of the Bentonite Buffer: A Preliminary Assessment within the Framework of the KBS-3H Disposal Concept. In Materials Research Society Symposium Proceedings, Volume 932, 2006.

[34] Xu, Y., Jiang, L., Liu, J., Zhang, Y., Xu, Jinxia and He, G., Experimental study and modeling on effective thermal conductivity of EPS lightweight concrete. Journal of Thermal Science and Technology. Volume 11, 11. 10.1299/jtst.2016jtst0023. 2016.

[35] Gökalp Z., Taş İ., Uzun O., et al., Yeralti Suyu Kirliliğini Önlemeye Dönük Bariyer Tasarımı.34, 122-131, 2017. https://doi: 10.13002/jafag4414

Zayıf Kayada Çivi Destekli Kazı Davranışının 1:1 Ölçekli Model Deneyi ile İncelenmesi

Arif ÇINAR[1*]
Havvanur KILIÇ[2]
M. Mehmet BERİLGEN[3]

ÖZ

Bu makalede, ayrışmış kumtaşı birimlerde yapılan derin kazıda uygulanan çivili destekleme sisteminin davranışı 1:1 ölçekli bir saha model deneyi ile incelenmiştir. Deney sahasında yapılan geoteknik araştırmalardan belirlenen kaya özellikleri dikkate alınarak yapılan limit denge ve sayısal analizler ile saha model deneyi tasarlanmıştır. Bu tasarıma göre yatayla 85° açı yapan, düşeyde 5 ve yatayda 7 sıra çivi ile desteklenen bir derin kazı yapılmıştır. Çiviler yatayda 15° açı ile yapılan 13 cm çaplı delgilere yerleştirilen ve enjeksiyonlanan 14 mm çaplı nervürlü inşaat çeliği ile imal edilmiştir. Deneyde nihai kazı kotuna kadar kademeli kazı yapılarak kesitin davranışı ölçüm ekipmanları ile gözlenmiş ve nihai kazı kademesinde kesit üzerine sürşarj yükü uygulanmıştır. Aletsel gözlemler çivilerin kafalarına yerleştirilen yük hücreleri (load cell), gövdelerine kaynaklanan şekil değiştirme ölçerler (strain gauge), düşey inklinometreler ve püskürtme beton kaplama üzerine yerleştirilen optik reflektörler ile gerçekleştirilmiştir. Deney sonuçlarını daha iyi değerlendirebilmek için proje sahasında 28 mm çaplı nervürlü inşaat çeliğinden imal edilen ve üzerine şekil değiştirme ölçerler yerleştirilen bir çivi elemanı üzerinde sıyrılma deneyi ile enjeksiyon betonu üzerinde serbest basınç deneyleri yapılmıştır. Kazı kademeleri ve uygulanan sürşarj yükü altında yapılan aletsel gözlem sonuçları grafik ve çizimler ile değerlendirilmiştir. Yapılan değerlendirmeler ışığında ayrışmış kaya birimlerde çivilerin güvenle uygulanabileceği, çivi destekli kazının tasarımının yerel ve genel stabilitesinin ayrıntılı saha ve laboratuvar deneyleri ile belirlenemeyen kaya özellikleri dolayısı ile aşırı güvenli tarafta kaldığı sonuçlarına ulaşılmıştır.

Anahtar Kelimeler: 1:1 ölçekli model deney, zayıf kaya, derin kazı, aletsel gözlem.

ABSTRACT

Investigation of Behavior of Nail-Supported Excavation in Weak Rocks by 1:1 Model Experiment

This paper investigated the behavior of a nail-supported deep excavation in a weathered sandstone unit using a 1:1 scale field model experiment. The 1:1 scaled model experiment was designed by the limit equilibrium and numerical analysis considering the rock properties determined from the geotechnical investigations in the area. So the deep excavation supported by 5 vertical rows and 7 horizontal rows nail was made. The nails are built with 14 mm diameter ribbed construction steels, which are placed and injected into 13 cm diameter drilled holes at a 15° angle. The excavation was performed step by step after the nail construction and geotechnical observation were conducted. A pull-off test on a nail and unconfined compression tests on grout samples were performed to assess the test results better. The pull-off test was performed on a nail that was 28 mm diameter ribbed construction steel, and the strain gauges were placed on it. The data of the instrumental observations made under the excavation stages and the applied surcharge load were evaluated with graphics and drawings. In light of the evaluations, it was concluded that nails could be applied safely in weathered rock units and that the local and general stability of the nail-supported excavation design remains on the extremely safe side due to the rock characteristics that could not determined by detailed field and laboratory experiments.

Keywords: 1:1 model test, weak rock, deep excavation, instrumental observation.

1. GİRİŞ

Derinliği 1.75 m'den fazla olan kazıların yapılması için uygun şev açısı ile şevli kazı yapılması veya güvenli kazı için iksa destekleme yöntemi seçilmesi gerekmektedir [1]. Terzaghi derinliği genişliğinden fazla olan kazıları veya yüksekliği 6.00 m'den fazla olan kazıları derin kazılar olarak tanımlamış ve destekleme ihtiyacından bahsetmiştir [2]. Zeminlerde yapılan derin kazılarda genellikle destekleme yapılması gerekli iken kaya ortamlarda destekleme ihtiyacı kayanın ayrışma ve süreksizlik durumuna göre değişmektedir. Geoteknik mühendisliğinde önemli yer tutan iksalı kazılar için 1930'lardan bu yana birçok arazi ve laboratuvar çalışmaları gerçekleştirilmiş ve günümüzde geçerli olan güncel tasarım ve uygulama yöntemlerine ulaşılmıştır. Kayalarda zemin ortamlardaki kadar araştırma olmadığı için yapılan iksalı kazılarda ya stabilite problemleri yaşanmakta ya da aşırı güvenli tarafta kalınmaktadır.

Kaya ortamlarda yapılan kazılarda stabilite sorunu yaşanmaması için kayanın ayrışma ve eklem durumu dikkate alınarak tasarlanan bir destekleme sistemine ihtiyaç olabilir. Güncel uygulamalarda kayada açılan derin kazılarda destekleme sistemi olarak genelde çivi veya öngerme ankrajlı sistemler tercih edilmektedir. Özellikle kalıcı iksa yapılarında bakım ve onarım zorluğu sebebiyle öngermeli ankrajlardan ziyade çivi yapılması yoluna gidilmektedir. Çivi ilk olarak Fransa'da zemin ortamında yapılan karayolu yarmalarının desteklenmesi için kullanılmıştır. Genellikle basit inşaat çeliği kullanılması, bakıma ihtiyaç duyulmaması, desteklediği birim ile kompozit bir sistem oluşturması ve deprem etkisinde performansının iyi olması zemin çivilerini tercih edilir kılmıştır. Özellikle Almanya [3] ve Fransa'da [4], [5] zemin çivileri ile alakalı birçok araştırma yapılmış ve zemin çivilerinin davranışı

aydınlatılmıştır [6]. Son yıllarda ise özellikle bilgisayar teknolojisinin gelişmesine paralel olarak birçok çalışmada yapay sinir ağı teknolojisi kullanılarak zemin çivilerinin davranışı incelenmiştir [7].

Kaya ortamlarda doğal ve yarma şevlerde çivilerin kullanımı yaygın olsa da literatürde zemin çivilerine oranla daha az çalışmaya rastlanmaktadır. Windsor [8], yılda 500.000.000 birim donatı kullanıldığını ve güçlendirme donatılarının kullanımında önemli ilerlemelere rağmen, bunların çeşitli kaya mühendisliği problemlerine uygulanabilirliği konusunda hala çelişki ve kafa karışıklığı bulunduğunu belirterek kaya güçlendirme donatıları ve teknikleri ile bunlara ilişkin kavramları açıklamıştır. Windsor [8] kayada kullanılan donatıları 1) *kaya bulonu* (genellikle 3.00 m'den daha kısa) 2) *halat bulon* (genellikle 3.00 m ile 15.00 m aralığındaki uzunlukta) 3) *zemin ve kaya ankrajları* (*ground anchors*) olarak sınıflandırılmış ve bunların uygulamadaki yerleşim düzenleri, aralıkları ve öngerme durumları ile kapasitelerini karşılaştırmıştır. Kaya bulonu, halat bulon ve ankraj ile imal edilen kaya donatıları aynı ekipman ile benzer şekilde üretilseler de karşıladıkları kuvvetler ve yük aktarma mekanizmaları birbirinden farklıdır. Kaya bulonu ve ankrajlara yüksek öngerme kuvvetleri uygulanırken halat bulonu olarak da tanımlanan kaya çivilerinde öngerme genellikle yapılmamakta veya çok düşük kuvvetlerde uygulanmaktadır.

Ma vd. [9], bir hidroelektrik santral projesinde kaya şevlerinin stabilitesini mikro sismik gözlem ve bunlara dayalı yapılan 3D sayısal analizler ile incelemiştir. Baraj gövdesinin oturtulduğu dik şevli nehir vadisi zayıf mekanik özelliklere sahip olduğundan temel kazıları çiviler ile takviye edilen palyeli şevler ile yapılmıştır.

Kaya güçlendirme sanatı hala gelişmektedir. Zheng vd. [10], ters eğimli süreksizlikleri olan kaya şevleri için akıllı ve hızlı donatı tasarımı için önerdikleri yaklaşım buna iyi bir örnektir. Bu çalışmada, ilk olarak, bir limit denge modeli kullanılarak kaya bulonları ile güçlendirilmiş ters eğimli süreksizlikleri olan kaya şevlerinin stabilitesini değerlendirmek için teorik bir yöntem önerilmiştir.

Literatürde kayalarda yapılan derin kazılarda kayanın güçlendirilmesi için çivi olarak tanımlanan donatı elemanı üzerine çok fazla çalışma olmadığı görülmektedir. Bu durum dikkate alınarak bu makalede zayıf kaya ortamında çivilerle desteklenerek açılan bir derin kazı davranışının 1:1 ölçekli saha model deneyi ile incelenmesi amaçlanmıştır. 1:1 ölçekli saha model deneyinde kademeli kazı yapılarak püskürtme beton ile kaplama ve çiviler imal edilmiş, her kazı-çivi imalatı kademesi sonunda aletsel ölçümler gerçekleştirilmiştir. Bu kapsamda çivi kafasında eksenel kuvvet, çivi boyunca şekil değiştirme ve kazı kesitinde yatay yer değiştirmeler ölçülmüştür. Deneyde nihai kazı kademesine ulaşıldıktan sonra kazı arkasında sürşarj uygulanmış ve sürşarj etkisinde kazının ve çivilerin davranışı gözlenmiştir. Çivilerin nihai taşıma gücü çivi çekme (sıyrılma) deneyi ile belirlenmiştir. Yapılan tüm deneysel çalışmaların ayrıntıları ve alınan ölçüm verileri ile ulaşılan sonuçlar aşağıda sunulmuştur.

2. ZEMİN KOŞULLARI VE DENEY SAHASI

1:1 ölçekli saha model deneyi, Sakarya'nın Adapazarı İlçesi'nde inşası planlanan katı atık arıtma tesisi için yapılan bir derin kazı destekleme projesi kapsamında gerçekleştirilmiştir. Proje alanının konumu ve çivili derin kazı imalatı Fotoğraf 1'de gösterilmiştir. Fotoğraf 1'de

görülen kesimde kazı kademeli olarak yatayla 54° açı ile (1Y:1.4D) şevli kazılmıştır. Palye genişliği 5.00 m ve kazı kademeleri sırasıyla altta 15.00 m ve üstte 10.00 m'dir. Kazı derinliğinin 25 m'lere ulaştığı bu projede kazı stabilitesinin kalıcı çiviler ile arttırılmasının uygun bir mühendislik çözümü olduğu görülmüştür.

Fotoğraf 1 - İnceleme alanı a) uydu görüntüsü b) çivili iksa uygulama görüntüsü

Model deneyin gerçekleştirildiği proje alanında detaylı jeolojik ve geoteknik etütler yapılmış ve bölgenin genelde Çakraz Formasyonuna ait kumtaşı birimlerden oluştuğu belirlenmiştir. Karasal çökellerden oluşan Çakraz Formasyonu, kahve-kızılımsı renge sahip olup çakıltaşı, kumtaşı ve çamurtaşlarından oluşmaktadır. Yapılan sondajlarda üst seviyelerde 4-5 m derinliğe kadar W5, 10-12 m derinliğe kadar W2-W3 ayrışma dereceli kumtaşı birimlere rastlanmıştır. Saha deneyleri için önemli olan ilk 10 m derinlikte RQD değerleri %0-33 arasında elde edilmiş olup bu durum sahadaki birimin ayrışma derecesinin ileri düzeyde olduğunu göstermektedir. Yapılan sismik deneylerde nebati toprak ve altında yapay dolgu ile çok ayrışmış kumtaşı ilk tabaka için ortalama V_s=280 m/s ve sonraki tabaka için ortalama V_s=570 m/s ölçülmüştür. Sahada yapılan sondajlara ait örnek karot sandığı Fotoğraf 2'de ve elde edilen idealize zemin profili Şekil-1'de sunulmuştur.
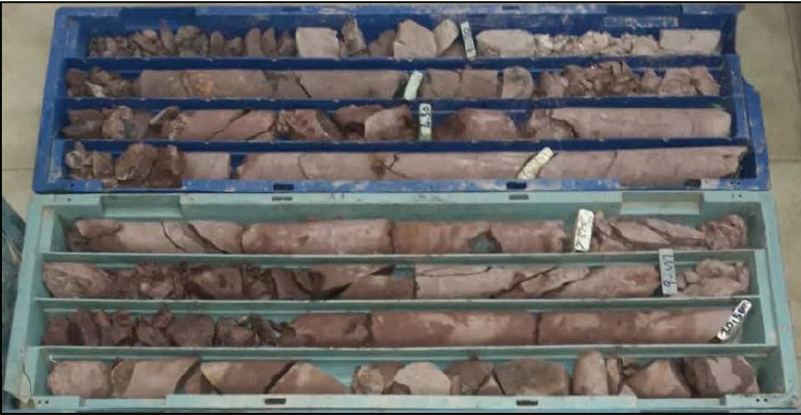
Fotoğraf 2 - Model deney alanındaki karot sandıklarından biri
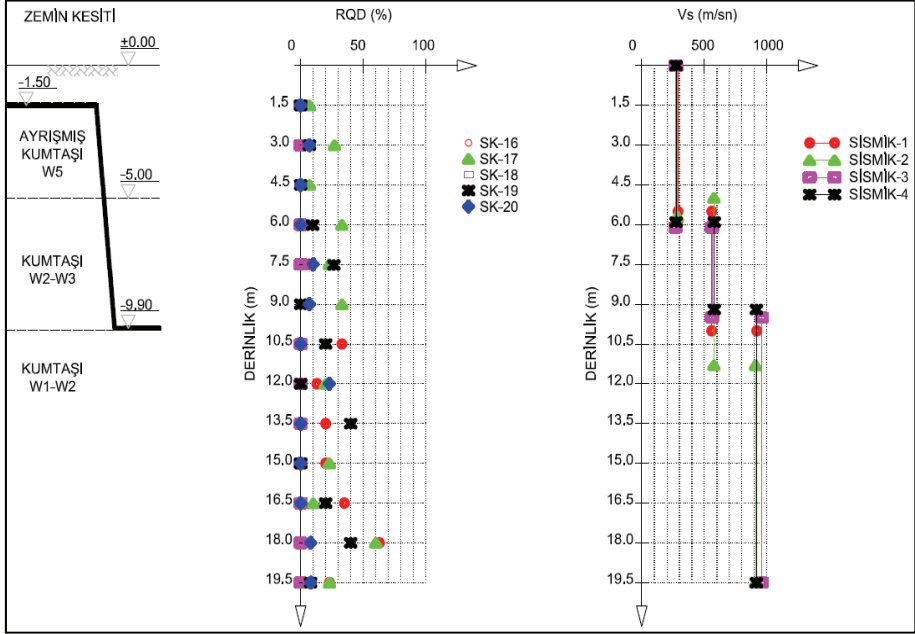
Şekil 1 - İdealize geoteknik model, RQD'ler ve sismik saha deneyi sonuçları

Deney alanında yapılan sondajlardan alınan numuneler üzerinde birim hacim ağırlık, nokta yükleme ve tek eksenli basınç deneyleri yapılmıştır. Tablo 1'de bu deneylerin sonuçları verilmiştir.

Tablo 1 - Deney alanında bulunan kaya parametreleri özet tablosu

Sondaj No	Sondaj Kotu (m)	Derinlik (m)	RQD (%)	γ (kN/m³)	I_{s_50} (MPa)	q_u (MPa)
SK-16	105.00	0.0-5.0	0			
		5.0-10.0	7	25.5		40.37
SK-17	112.00	0.0-5.0	14	26.6	2.36	
		5.0-10.0	33	27.0		13.79
SK-18	130.00	0.0-5.0	0			
		5.0-10.0	0	25.6	1.02	
SK-19	139.85	0.0-5.0	2			
		5.0-10.0	12	24.7	1.54	
SK-20	116.00	0.0-5.0	2	21.5	0.94	
		5.0-10.0	3	24.8	0.41	

Tablo 1'de görüldüğü gibi deney sahasında kumtaşı-çamurtaşı birimin numune (intact) birim hacim ağırlığı (γ) 21.5-27.0 kN/m³ arasında değişmektedir. Nokta yükleme mukavemetleri (I_{ss50}) 0.41-2.36 MPa arasındadır. Deneylerde serbest basınç mukavemeti (q_u) 13.79-40.37 MPa arasında elde edilmiştir. RQD değerlerine göre ilgili birim "zayıf kaya" olarak sınıflandırılmıştır [11].

3. 1:1 ÖLÇEKLİ SAHA MODEL DENEYİ

Zayıf kayada çivi davranışını incelemek için kumtaşı-kiltaşı formasyonlu proje sahasında 1:1 ölçekli bir model deney yapılmıştır. Model deneyin tasarımı sonlu elemanlar yöntemine dayalı gerilme şekil değiştirme analizleri ve limit dengeye dayalı stabilite analizleri ile gerçekleştirilmiştir. Bu tasarımda 4.20 m x 4.20 m alanda 170 kPa sürşarj basıncı ve maksimum 8.40 m kazı yüksekliği göz önüne alınmış, "FHWA-Zemin Çivili Duvar Tasarımı [6]" referansı esas alınarak çiviler boyutlandırılmıştır (Şekil 2). Bu kapsamda yapılan stabilite analizleri çivi davranışını eğilme ve kesme dayanımını dikkate alarak Basitleştirilmiş Bishop Dilim Yöntemini esas alan Talren 4 ticari yazılımı ile gerçekleştirilmiştir. Sürşarj basıncı, reaksiyon ankrajları ve çelik yükleme kirişleri kullanılarak oluşturulan yükleme sisteminde betonarme başlık plağı ve kirişler arasına yerleştirilen hidrolik kriko ile uygulanmıştır. Tasarımda Tablo 2'de verilen parametreler kullanılmıştır. Kayma mukavemeti parametreleri RMR (rock mass rating) sistemi [12] dikkate alınarak RocLab [13] ticari yazılımı yardımı ile belirlenmiştir. RocLab yazılımında kaya sınıflandırması RMR kaya sınıflandırma sistemine göre genelleştirilmiş Hoek-Brown Göçme Kriteri kırılma zarfı ve malzeme parametreleri (m_b, s ve a) belirlenmekte ve kaya kütlesi için eşdeğer Mohr-Coulomb Göçme Kriteri'nin kayma mukavemeti parametrelerini (kohezyon ve sürtünme açısı) hesaplanmaktadır.

Tablo 2 - Model deneyin tasarımında kullanılan kaya parametreleri

Tabaka	Tabaka kalınlığı (m)	Birim hacim ağırlık (γ) kN/m³	Kayma mukavemeti açısı (ϕ) (°)	Kohezyon (c) kPa	Birim sürtünme direnci (q_s) kPa
Kumtaşı-1	4.0	21	26	5	75
Kumtaşı-2	4.4	26	31	85	200

Kazının çivilerle takviye edilmeden yapılması ve sürşarj yüküne maruz bırakılması durumunda Tablo 2'de verilen parametrelerle Basitleştirilmiş Bishop Dilim Yöntemi ile limit dengeye göre yapılan stabilite hesabında güvenlik sayısı FS=0.77 olduğu belirlenmiştir. Kazı stabilitesini artırmak için yapılan analizler sonucunda çapı 14 mm olan nervürlü inşaat çeliğinden yapılan çivilerin 1.40 m yatay ve düşey aralıklar ile kazı derinliğince 5 sıra tatbik edilmesi uygun bulunmuştur. Yapılan ön analizlerde yeterli güvenliği sağlamak için çivi boyları üstteki üç sıra çivide 6 m ve alttaki iki sıra da ise 4 m seçilmiştir. Çivilerin boyutları ve tasarımda dikkate alınan birim sürtünme direnci (q_s) ve çivi donatısı akma dayanımı (f_{yk}) değerlerine göre güvenli taşıma gücü (N_{maks}) değerleri Tablo 3'te verilmiştir.
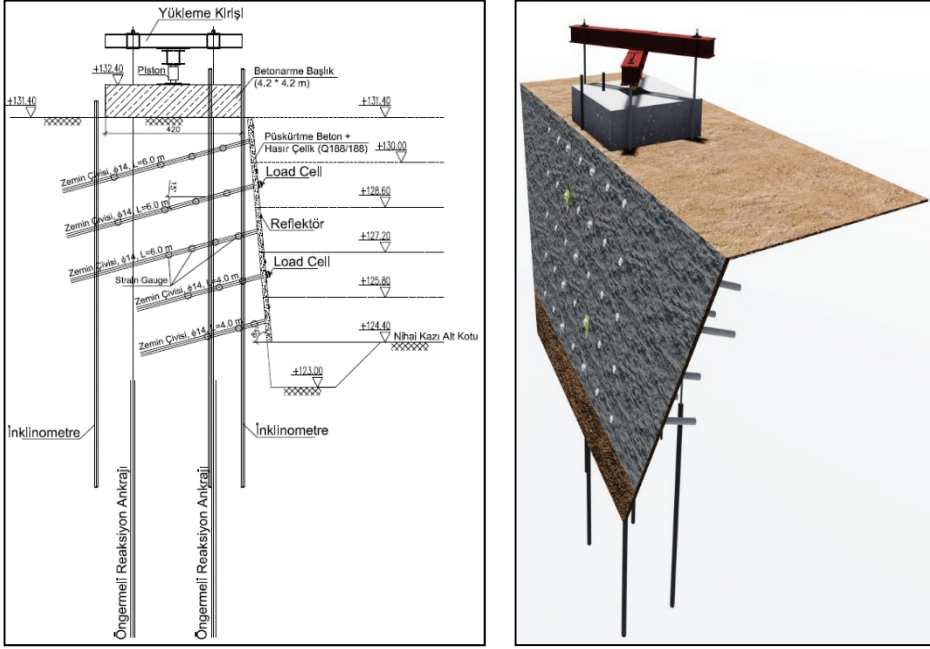
Şekil 2 - 1:1 ölçekli model deney a) En kesit b) Perspektif görünüşü

Tablo 3 - Çivi tasarımında kullanılan parametreler

Çivi No	Çivi kotu	Çivi boyu (L, m)	Çivi açısı (β, °)	Güvenli taşıma gücü (N_{maks}, kN)
1. Sıra (T1)	130.70	6	15	56.2
2. Sıra (T2)	129.30	6	15	56.2
3. Sıra (T3)	127.90	6	15	56.2
4. Sıra (T4)	126.50	4	15	56.2
5. Sıra (T5)	125.10	4	15	56.2

Limit denge çözümlerinde çivilerdeki eksenel yükler tanımlanırken hem çivinin etrafındaki sürtünme direncini (q_s) hem de çivi donatısının akma dayanımını (f_{yk}) dikkate alacak şekilde eksenel yük dağılımı kullanılmıştır. Maksimum çivi yükü olarak donatının akma dayanımına FS=1.15 güvenlik katsayısı uygulanarak hesaplanan N_{maks}=56.2 kN değeri kullanılmıştır. Buna göre çivilerin boyutlandırılmasında dikkate alınan sıyrılma, çekme ve kaplama yükü kapasiteleri ile sıyrılma yükü zarfı Şekil 3'te gösterilmiştir [6]. Şekilden de anlaşılacağı üzere zemin türüne göre çivinin taşıyabileceği maksimum yük çivinin sıyrılma kapasitesi veya donatının kopma kapasitesi ile sınırlanmaktadır.
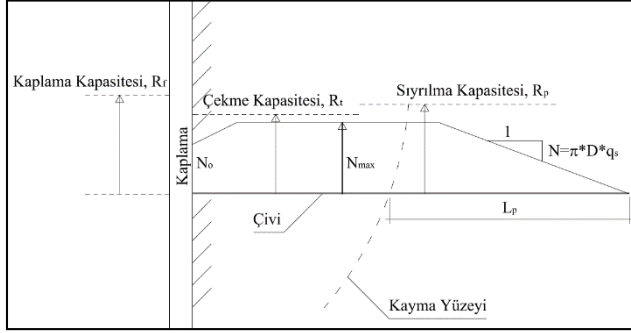
Şekil 3 - Çivi boyutlandırılmasında dikkate alınan yük kapasiteleri ve sıyrılma yükü zarfı

Kazı yüzeyleri hasır çelik ve püskürtme beton (shotcrete) ile kapatılmıştır. Kazının limit denge durumuna ulaşması ve çivilerin daha fazla yüklenmesini sağlamak için en son kademede püskürtme beton uygulanmadan 1.40 m ilave kazı yapıldıktan sonra sürşarj uygulanmıştır. Sürşarj uygulaması zemin yüzeyinde tesis edilen özel bir yükleme düzeneği ile yapılmıştır. Bu düzenek 4.20 m x 4.20 m boyutlarında inşa edilen betonarme bir plak üzerine yerleştirilen 300 tonluk hidrolik kriko ile 4 adet reaksiyon ankrajları ve yükleme kirişleri kullanılarak oluşturulmuştur. Bu yükleme düzeneği ile kazı arkasında betonarme plak vasıtası ile 170 kPa mertebelerinde bir sürşarj basıncı oluşturulması planlanmıştır. Sürşarj basıncı kademeli olarak uygulanmış ve boşaltılmıştır (Şekil 2 ve Fotoğraf 3). Nihai kazı ve sonrasında uygulanan ortalama 170 kPa mertebesindeki sürşarj basıncı altında önemli deformasyon ve stabilite problemlerinin ortaya çıkmadığı görülmüştür.
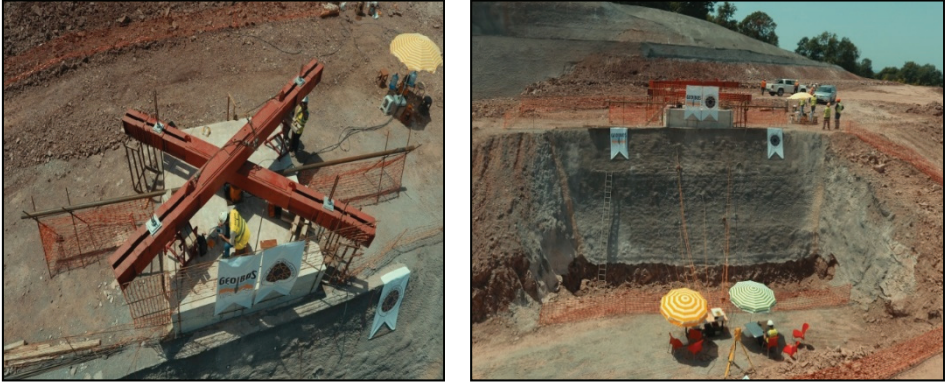
Fotoğraf 3 - Model deney a) Sürşarj yükleme düzeneği b) Kazı sonrası önden görünüş

3.1. Ölçüm Aletleri

Model deneyde kazı ve sürşarj etkisi ile kazı ortamının, yüzey kaplama betonunun ve çivilerin davranışını incelemek için bu elemanlara çeşitli ölçüm aletleri yerleştirilmiştir. Bu ekipmanlar, çivi başlarında yük hücreleri (load cell), çivilerin üzerine yerleştirilen şekil değiştirme ölçerler (strain gauge), püskürtme beton yüzeyine yerleştirilen optik ölçme

noktaları (reflektörler), başlık kirişi deplasmanını ölçmek için komparatörler ve inklinometre kuyularıdır. Çivilerin üzerine yerleştirilen şekil değiştirme ölçerler Şekil 2'de gösterildiği gibi her çivide 3 veya 4 farklı noktada olmak üzere toplam 32 adettir. Şekil değiştirme ölçerler çivilerin üzerine Fotoğraf 4'te gösterildiği gibi kaynaklanmış ve bir veri toplama sistemi (data logger) yardımı ile şekil değiştirme ölçümleri bilgisayara aktarılmıştır.
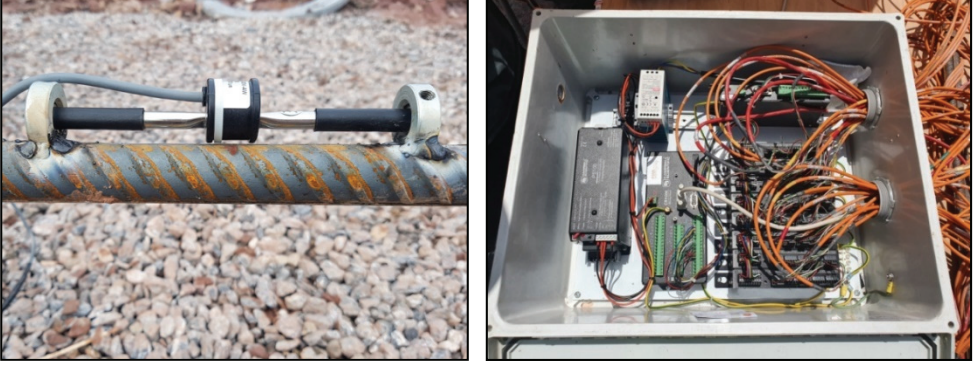
Fotoğraf 4 - Kaynaklı şekil değiştirme ölçer ve çok kanallı data logger görüntüsü

Çivilerin karşıladığı eksenel yükü belirlemek için 2 çivinin başlığına Fotoğraf 5'te gösterildiği gibi yük hücreleri (load cell) yerleştirilmiştir.

Fotoğraf 5 - Yük hücresi

Kazı yapılan ortamın yer değiştirmelerini ölçmek için kazı kesitine ardı ardına 3 adet inklinometre ve shotcrete yüzeyine 30 adet reflektör yerleştirilmiştir (Fotoğraf 6).

Fotoğraf 6 - Reflektör ve inklinometre ölçüm görüntüleri

3.2. Çivi Çekme Deneyi

Çivi çevresindeki jeolojik ortam ile enjeksiyon ara yüzünün sürtünme direnci (q_s) tasarıma yön veren önemli bir parametredir. Sürtünme direnci, jeolojik ortam türü, delgi yöntemi, enjeksiyon özellikleri, düşey efektif gerilme, ortamın birim hacim ağırlığı gibi birçok değişkene bağlıdır. Bu parametrelerin belirlenmesinde en doğru yaklaşım yerinde çivi çekme deneylerinin yapılmasıdır. Bu sebeple 1:1 ölçekli saha deneyinde kazıyı destekleyen çivilerin davranışlarını belirlemede yardımcı olmak üzere bir çivi üzerinde çekme deneyi yapılmıştır. Bu deney, 5.00 m delgi boyu ve 4.00 m enjeksiyon boyuna sahip bir çivi üzerine şekil değiştirme ölçerler yerleştirilerek bir hidrolik kriko ile çivinin kafasına eksenel çekme uygulanarak yapılmıştır. Çivideki uzama miktarı hidrolik pistonun hareketine bağlı olup piston ucuna yerleştirilen bir yer değiştirme ölçer vasıtası ile ölçülmektedir (Fotoğraf 7).

Fotoğraf 7 - Çivi çekme deneyi düzeneği

Çekme deneyinde, reaksiyon bölgesinde oluşacak gerilmelerin çivi gövdesini etkilememesi için çivinin yüzeyden itibaren ilk 1.00 m'lik kısmı enjeksiyonlanmadan serbest boy olarak bırakılmıştır. Çekme deneyi uygulanan bir çivinin detayı Şekil 4'te verilmiştir.
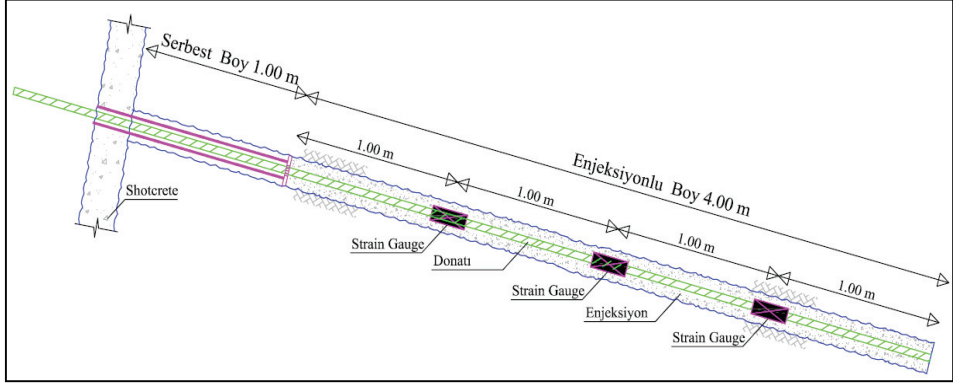
Şekil 4 - Çekme yapılan çivi detayı

Şekil değiştirme ölçerler çivi üzerine Fotoğraf 4'de gösterildiği şekilde kaynakla tutturulmuştur. Kullanılan şekil değiştirme ölçerler kalibrasyon sertifikalarına göre kalibre edildikten sonra doğru şekil değiştirme ölçüldüğü Yıldız Teknik Üniversitesi Yapı Laboratuvarı'nda doğrulama testleri ile kontrol edilmiştir.

Çivi çekme deneyi "FHWA-Zemin Çivili Duvar Tasarımı-Doğrulama Testi Prosedürü" dikkate alınarak çivide göçme (sıyrılma, akma veya kopma) olana kadar yükleme yapılarak gerçekleştirilmiştir [6], [14], [15]. Deneyde çivi donatısı olarak D=28 mm çapında S420 sınıfı nervürlü inşaat çeliği kullanılmıştır. Çekme deneyi uygulanan çivinin model deneyde kullanılan 14 mm çapındaki donatıdan daha kalın olması tercih edilmiştir. Böylece daha kalın donatıların dayanımından faydalanarak daha yüksek çekme yüklerine çıkılması ve enjeksiyon/zemin arasında sürtünme direncinin yenilmesi hedeflenmiştir. Çekme deneyi yapılan çivi model deney sahasında D=130 mm çapında, havalı tabancalı delgi yöntemi ile imal edilmiştir. Çivi imalatında ağırlıkça 2/3 oranında su/çimento kullanılmıştır. Sahada imal edilen enjeksiyonlardan numuneler alınarak laboratuvarda serbest basınç deneyine tabi tutulmuştur. Deney sonucunda elde edilen elastisite modülü değerleri Tablo 4'te verilmiştir.

Tablo 4 - Enjeksiyon numuneleri deney sonuçları

Numune Yaşı	Elastisite Modülü	Poisson Oranı	Birim Hacim Ağırlık
(gün)	E (GPa)	ν (−)	γ (kN/m³)
7	2.89	0.28	17.15
14	4.71	0.26	17.10
Ort.	3.80	0.25	17.10

Çekme deneyi sonunda elde edilen yük-şekil değiştirme diyagramı ϕ28 mm çaplı nervürlü inşaat çeliğinin yük-şekil değiştirme diyagramı ile birlikte Şekil 5'te verilmiştir. Çelik donatının laboratuvar çekme deneyi sonuçlarını saha çivi çekme deneyi sonuçları ile karşılaştırabilmek için yüklerin dikkate alındığı düşey eksen logaritmik ölçeklendirilmiştir. Şekil 5'ten görüldüğü gibi çivi çekme deneyi yük-şekil değiştirme ilişkisi çelik donatınınkinden farklıdır. Bu farklılık çelik donatıyı kaplayan enjeksiyonun çevresindeki kaya ile etkileşiminden kaynaklanmaktadır.
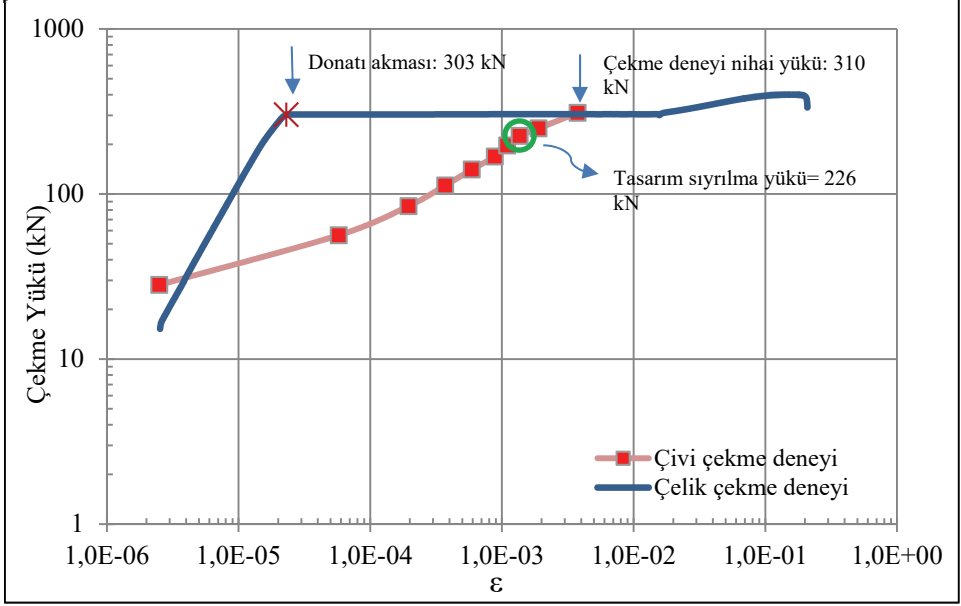
Şekil 5 - Çivi çekme deneyinde yük-şekil değiştirme grafiği

Çivi ekseni boyunca ölçülen normal şekil değiştirmeler (ε_x) dikkate alınarak aşağıdaki eşitlik ile çivi boyunca eksenel kuvvet (N) değişimi hesaplanmıştır.

$$N = \varepsilon_x E_k A_k \tag{1}$$

Bu eşitlikte E_k ve A_k kompozit kesitin elastisite modülü ve enkesit alanıdır. Kompozit kesitin elastisite modülü enjeksiyon ve çeliğin elastisite modülleri alanları oranında dikkate alınarak belirlenen kompozit elastisite modülü ile hesaplanmıştır. Buna göre çivi elemanının kompozit elastisite modülü;

$$E_k = \left\{ \frac{(E_{enj}*A_{enj})+(E_d*A_d)}{A_{enj}+A_d} \right\} \tag{2}$$

eşitliğinden belirlenmiştir. Burada E_k kompozit kesitin elastisite modülünü, E_{enj} ve E_d çivi enjeksiyonunun ve donatının elastisite modülünü temsil etmektedir. A_{enj} ve A_d ise sırasıyla çivi enjeksiyonu ve donatının kesit alanıdır. Kompozit kesitin elastisite modülü (E_k) ve strain gaugelerde okunan normal birim şekil değiştirme (ε) değerleri kullanılarak kesit üzerindeki gerilmeler (σ) ve kesit alanı kullanılarak eksenel yükler (N) hesaplanmıştır. 250 kN eksenel çekme yükü altında 4.00 m enjeksiyon boyuna sahip çivide hesaplanan eksenel yük değişimleri Şekil 6'da verilmiştir.
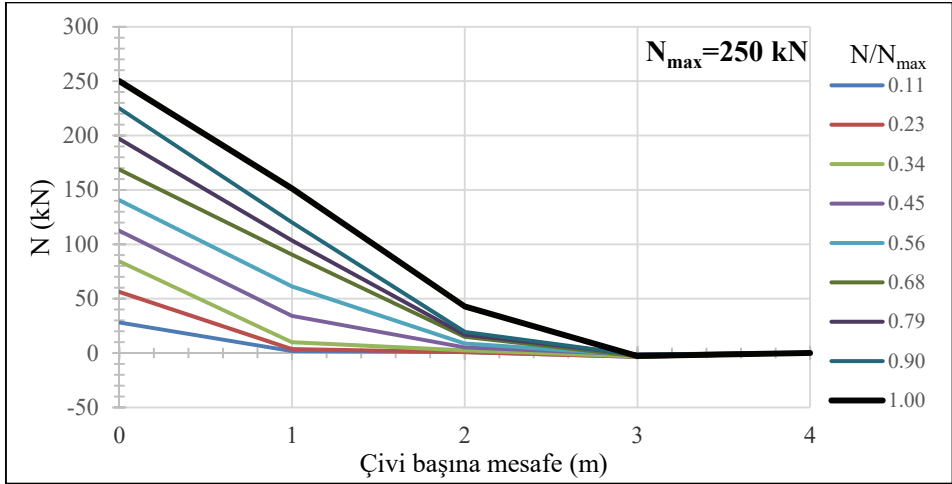
Şekil 6 - Çivi çekme deneyinde eksenel yükün çivi boyunca değişimi

Eksenel yük değişimleri ve aşağıdaki eşitlik kullanılarak kaya/enjeksiyon betonu arasındaki kayma gerilmeleri (τ) belirlenebilir:

$$N = \pi D \int_0^L \tau dl \tag{3}$$

Bu eşitlikte L çivi boyu olup Şekil 6'da verilen N değerleri kullanılarak kayma gerilmeleri (τ) Şekil 7'de gösterildiği gibi belirlenmiştir.

Şekil 7'de verilen eksenel çekme altında kayma gerilmelerinin çivi boyunca değişimleri literatürle uyumlu olup enjeksiyon başlangıcından uzaklaştıkça azalmakta 3.00 m mertebelerinde sıfırlanmaktadır. Buna göre sıyrılma gerilmesi (bond stress, τ) çivi başında hesaplanırken uzunluk dl=3.00 m alınmıştır. Bu durum donatının kopma durumuna ulaşması durumunda çivinin 2/3'ünün uygulanan eksenel çekme kuvvetini karşıladığını veya diğer bir deyişle kumtaşı-kiltaşı birimde 3.00 m mertebelerindeki S420 nervürlü donatı çeliğinde akma dayanımına ulaşılmakta fakat donatı sıyrılmasının olmadığını göstermektedir.

Deneyde belirlenen maksimum kayma gerilmesi 265 kPa olup güncel literatürde kumtaşı için önerilen sürtünme direnci q_s=200-300 kPa aralığı ile uyumludur [6]. Model deneyin tasarımında çivi sürtünme direnci bu aralığın alt sınırında (200 kPa) öngörülmüş olup deneyde ölçülen maksimum sürtünme direncinin bir miktar altında kalmıştır.
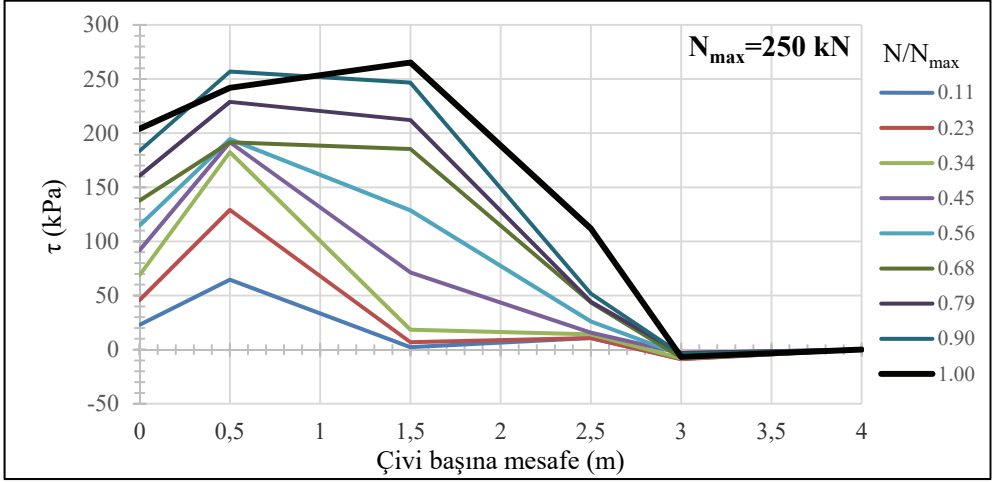
Şekil 7 - Çivi çekme deneyinden elde edilen çivi boyunca kaya/enjeksiyon arayüzünde kayma gerilmeleri değişimi

3.3. Ölçümler ve Değerlendirmeleri

Deneye başlamadan önce tüm ölçüm aletleri veri toplama sistemine (data logger) bağlanarak başlangıç okumaları alınmıştır. Deneye 1.40 m derinlikte ilk kazı yapılarak başlanmış, ilk kademe çivi delgileri 15° eğimli imal edilmiş, deliklere nervürlü çelik yerleştirilmiş ve enjeksiyonlama işlemi yapılmıştır. Daha sonra ilk kademe kazı yüzeylerine hasır çelik yerleştirilmiş ve püskürtme beton ile kaplanmıştır. Kazı kademesi açıldıktan sonra inklinometrelerden okuma alınarak yatay deplasmanlar kontrol edilmiştir. Çivi enjeksiyonlarının en az 7 gün priz süresini tamamlaması sonrasında 1.40 m yüksekliğindeki

Tablo 5 - Deney aşamaları

Sıra	Deney Aşamaları	Kazılan kalınlık (m)	Kazı Derinliği (m)	Ölçümler			
				İnklinometre	Şekil Değiştirme	Optik Ölçüm	Yük Hücresi
1	1. Kademe kazı	1.40	1.40	✓			
2	2. Kademe kazı	1.40	2.80	✓	✓		
3	3. Kademe kazı	1.40	4.20	✓	✓		✓
4	4. Kademe kazı	1.40	5.60	✓	✓		✓
5	5. Kademe kazı	1.40	7.00	✓	✓		✓
6	6. Kademe kazı	1.40	8.40	✓	✓		✓
7	Bekleme (30gün)		8.40	✓	✓		✓
8	Sürşarj		8.40	✓	✓	✓	✓

ikinci kademe kazı yapılmıştır. Bu aşamada ilk kademe zemin çivilerinde yer alan şekil değiştirme ölçerlerden (strain gauge) ve inklinometrelerden ölçümler alınmıştır. Yapılan işlemler her kazı kademesinde tekrarlanarak nihai kazı kademesine ulaşılmıştır. Son kazı kademesinde iksa sisteminin daha fazla yer değiştirme yapması ve sistemin göçmeye yakın davranış sergilemesi için kazı yüzeylerine püskürtme beton uygulaması yapılmamıştır. Nihai kazı kademesinde yaklaşık 30 gün beklenmiş, ara okumalar alınarak bekleme süresince kazıda oluşacak hareketler ve çivilerde oluşacak yük değişimleri ölçülmüştür. Daha sonra kesit üzerine 4.20 x 4.20 m boyutlarında, 1.00 m yüksekliğinde başlık kirişi imal edilmiş ve bir hafta sonra sürşarj uygulaması yapılmıştır. Deney adımları Tablo 5'te verilmiştir.
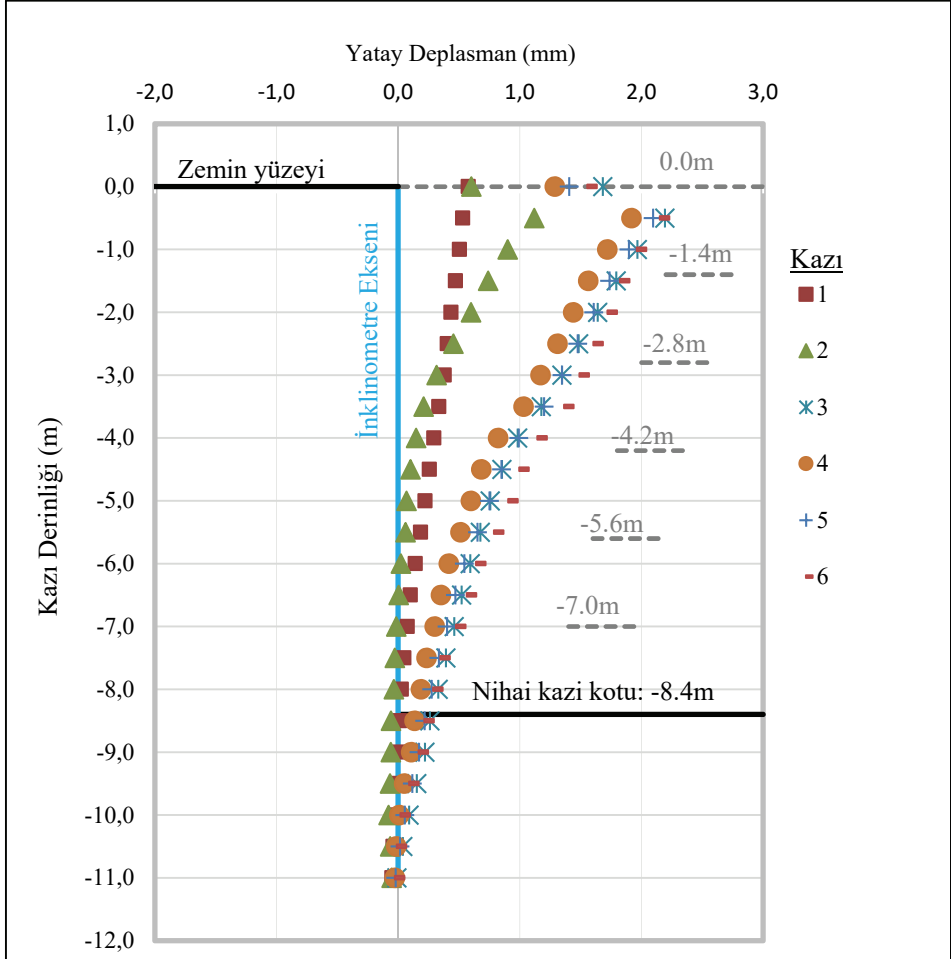
Şekil 8 - İnklinometre ölçümleri

Kazı kademeleri ve sürşarj yüklemesi sırasında alınan inklinometre ölçümleri Şekil 8'de verilmiştir. Şekilden görüldüğü gibi nihai kazı kademesine ulaşıldığında 2 mm mertebesinde

yatay yer değiştirme ölçülmüştür. Alınan inklinometre ölçümlerine göre bekleme süresince ve sürşarj uygulaması sırasında yatay yer değiştirmelerde artış gözlemlenmemiştir.

Çivilerde kazı kademeleri sonrasında alınan şekil değiştirme ölçümlerinden yararlanılarak çivi boyunca eksenel kuvvetler hesaplanmıştır. Hesaplanan çivi normal kuvvetlerinin (N) kazı kademelerine göre, çivi boyunca değişimleri kazı enkesiti üzerinde Şekil 9'da verilmiştir. Şekil 9'da gösterilen kazı kademelerine bağlı çivi boyunca eksenel kuvvet değişimlerinin, çivi konumu, geometrisi ve kazı derinliğine bağlı olduğu anlaşılmaktadır. Buna göre kazı yapıldıkça artan yanal gerilmelere bağlı olarak çivilerin şekil değiştirmelerinin ve üzerine etkiyen eksenel yüklerin (N) arttığı gözlenmiştir. Bu durum kazı derinliğine bağlı olarak şekil değiştirmelerin meydana geldiği ve böylece çivilerin çalışmaya ve yük taşımaya başladığını göstermektedir. Nihai kazı kademesinde çivilerin shotcrete yüzeye bağlı kafa bölgelerinde daha çok şekil değiştirme ve eksenel kuvvete sahip olduğu, çivinin gömülü ucuna gidildikçe şekil değiştirme ve eksenel kuvvetlerin azaldığı görülmüştür. Planlanan nihai kazı derinliğinde çivilerin maruz kaldıkları eksenel yük tasarımda dikkate alınan güvenli taşıma gücü (N_{maks}) ile normalize edilerek karşılaştırıldığında Şekil 10'daki grafik elde edilmiştir. Buna göre nihai kazı kotuna ulaşıldığında eksenel kuvvet değerleri çivi boyunca değişmektedir. 1. ve 2. sıra çivilerde en büyük eksenel kuvvet çivi başında görülürken 3. ve 5. sıradakilerde çivi boyunun 1/4 mesafesinde ve 4. sıradakinde ise çivi başından itibaren boyunun 2/3 mesafesinde görülmektedir. Nihai kazı kotuna ulaşıldığında en büyük eksenel yük 4. sıra çivide ölçülmüş olup güvenli taşıma gücünün yaklaşık %40'ı oranındadır.
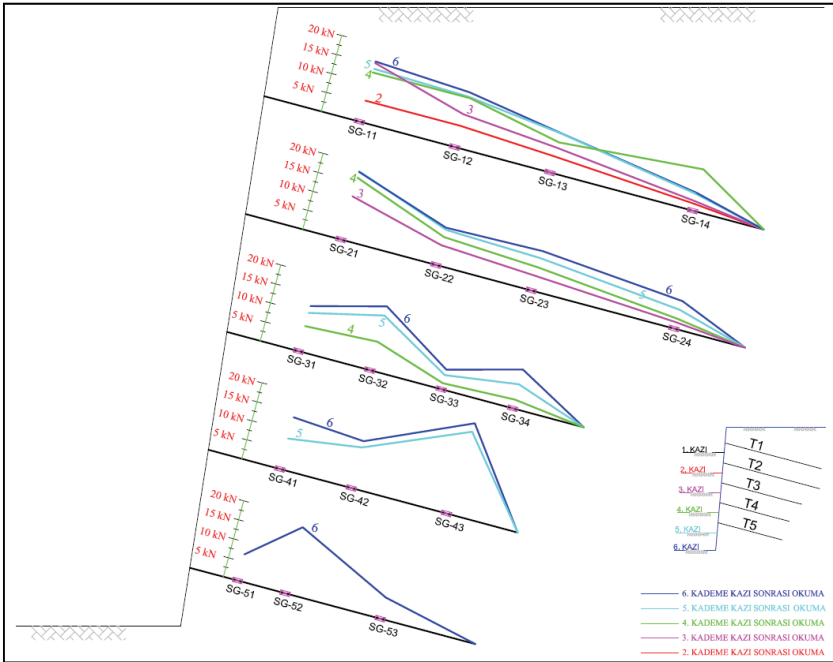
Şekil 9 - Çivilerde kazı seviyesine bağlı eksenel yük değişimi
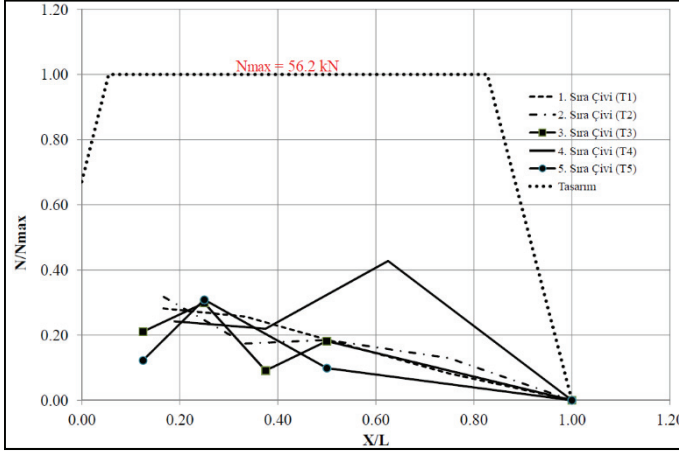
Şekil 10 - Nihai kazı durumunda çivilerdeki en büyük eksenel yükler
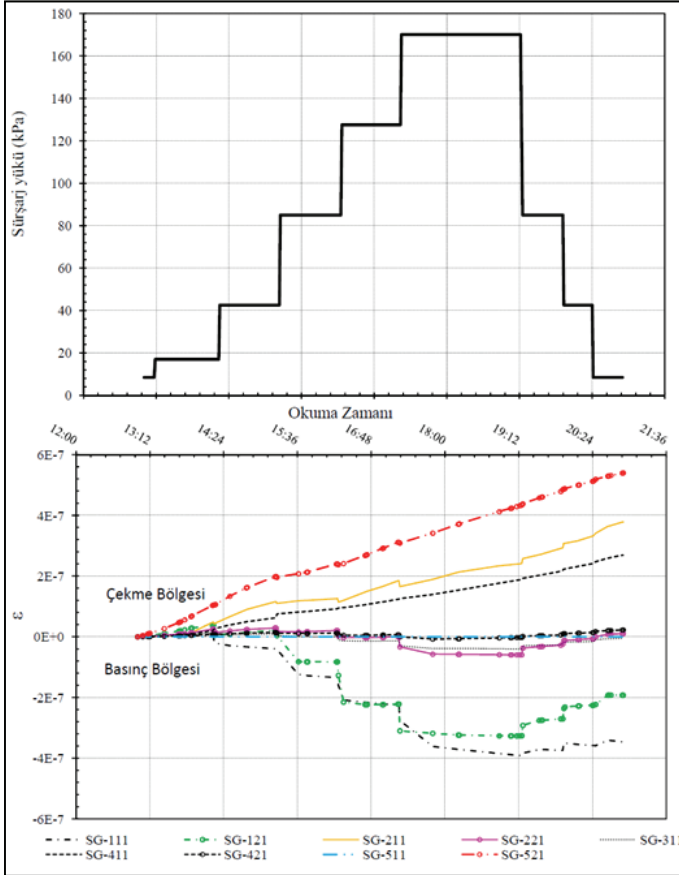
Şekil 11 - Uygulanan sürşarj yükleri ve kafa bölgelerinde ölçülen şekil değiştirmeler

Kazı kademeleri tamamlandıktan sonra yaklaşık bir ay beklenmiş ve çivilerde oluşabilecek eksenel yük artışları izlenmiştir. Sonrasında kesit üzerinde yer alan 4.20x4.20 m boyutlarındaki başlık kirişine 300 ton sürşarj yükü uygulanmıştır. Bu yükleme ile 170 kPa mertebelerinde bir sürşarj basıncı altında çivili kazının davranışı izlenmiştir. Sürşarj yükü Şekil 11'de gösterildiği şekilde 6 kademede uygulanmış ve 4 kademede boşaltılmıştır. Uygulanan sürşarj basıncına göre çivilerin kafa kısmına yakın bölgelerindeki şekil değiştirme ölçümleri Şekil 11'de verilmiştir. Bu şekilde verilen şekil değiştirmeler sadece sürşarj yükünden kaynaklanmakta ve kazı kademelerinde alınan şekil değiştirmeleri içermemektedir.

Şekil 11'de verilen çivilerin şekil değiştirme değerlerine göre sürşarja yakın olan çivilerin kafa bölgesinde negatif şekil değiştirme değerleri ölçülmüştür. Buna göre 1 ve 2 nolu çiviler sürşarj etkisinde bir miktar kısalmaya çalışmış yani basınca maruz kalmıştır. Tüm kazı tamamlandıktan sonra sadece sürşarj yükünden kaynaklanan, çivi boyunca alınan şekil değiştirme ölçümleri dikkate alınarak çivi boyunca oluşan normal kuvvetler hesaplandığında Şekil 12'de verilen normal kuvvet değişimleri elde olunmuştur. Sadece sürşarj basıncı altında yüzeye yakın çivilerin eğilmeye çalışmasından dolayı bu çivilerde basınç kuvvetleri oluşabileceği görülmüştür.
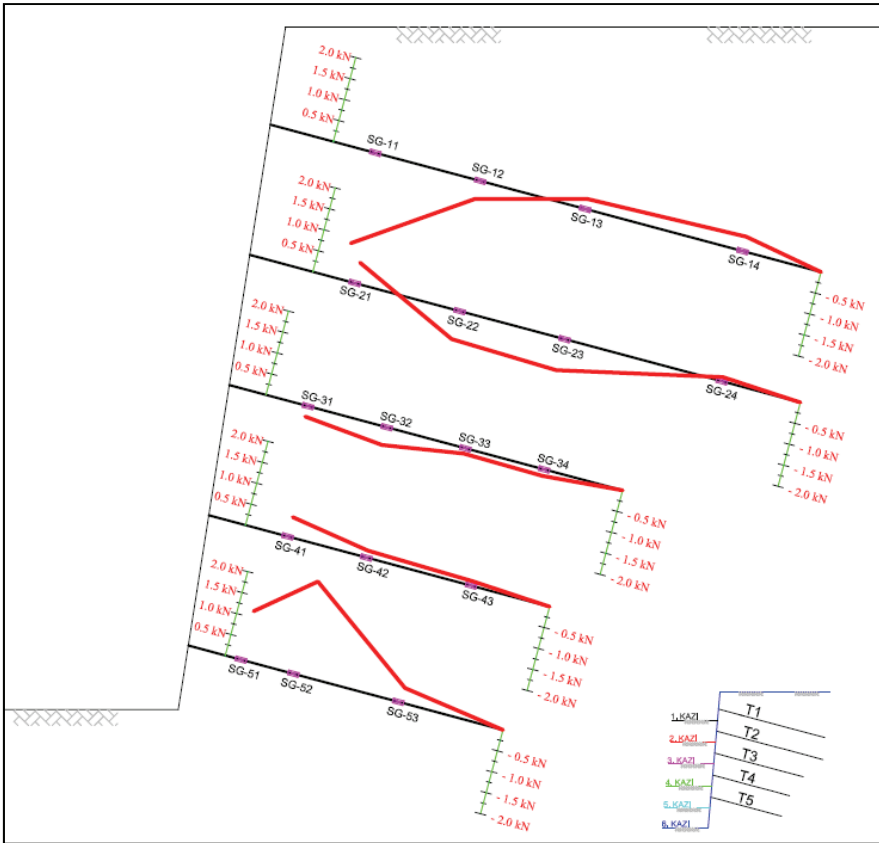
Şekil 12 - Sürşarj yüklemesinden kaynaklanan ilave çivi yükleri

Sürşarj yüklemesi sırasında yük kademeleri arttıkça püskürtme betonlu kazı yüzeyinde bulunan reflektörlerde deplasman artışları gözlenmiştir (Şekil 13). Kazı yüzeyinin üst kotlarında püskürtme beton yüzeyde 5.2 mm mertebesinde yatay deplasman ölçülürken kazı tabanında deplasman ölçülmemiştir. Yükleme sırasında başlık plağının yapılan ölçümlerde sistemin 3.7 mm mertebesinde oturma yaptığı belirlenmiştir (Şekil 13).

Şekil 13 - Sürşarj yüklemesi altında ölçülen yatay ve düşey yer değiştirmeler

Şekil 14 - Nihai kazı, bekleme süresi ve sürşarj sırasındaki çivi toplam eksenel yükleri

Sürşarj yüklemesi sırasında çivilerin kafa bölgelerine yerleştirilen yük hücrelerinden (load cell) okumalar alınmıştır. Kazı sırasında ve yükleme sırasında yük hücrelerinde herhangi bir değişiklik gözlenmemiştir. Bu durumun hidrolik yük hücrelerinin yük değişimine karşı yeterli derecede hassasiyete sahip olmamasından kaynaklandığı tahmin edilmektedir.

Çivilerde kazı, bekleme ve sürşarj etkisinde oluşan maksimum normal kuvvetlerin nihai kapasite de dikkate alınarak karşılaştırılması Şekil 14'de verilmiştir. Bu şekilden görüldüğü gibi çivilerin kazı ve sonrasındaki bekleme süresi ile 170 kPa sürşarj yüklemesi altında maruz kaldıkları toplam normal kuvvetler tasarımda dikkate alınan değerlerin altında kalmıştır.

4. SONUÇLAR VE DEĞERLENDİRMELER

Bu çalışmada kırıklı-çatlaklı kumtaşı, kiltaşı birimlerde uygulanan çivili iksa sistemlerinde çivi/jeolojik ortam etkileşimi gerçek ölçekli arazi deneyleri ile incelenmiştir. 8.40 m derinlikte, düşeyde 5 sıra çivilerden oluşan destekleme sisteminde yüzey püskürtme betonla kaplanmış ve kademeli kazılar yapılarak çiviler imal edilmiştir. Kazı sırasında ve sürşarj yüklemesi sırasında çatlaklı kırıklı kaya ortamın yer değiştirme davranışı ile buna bağlı çivilerde oluşan şekil değiştirmeler ve eksenel yükler ölçüm ekipmanları tesis edilerek ölçülmüştür. Bu ölçüm ekipmanlarından alınan ölçümler yukarıda değerlendirilmiştir. Yapılan bu değerlendirmelerden şu sonuçlar çıkarılabilir;

1. Kırıklı çatlaklı kiltaşı-kumtaşı birimde yapılan çivi destekli derin kazı dolayısı ile dikkate değer şekil değiştirmeler meydana gelmemiş, herhangi bir yerel ve genel stabilite sorunu ile karşılaşılmamıştır.

2. Kazı sırasında ölçülen yatay yer değiştirme (2-3 mm) literatürde önerilen yatay yer değiştirme-derinlik oranının (deformasyon) ($\Delta y = \%(0.1-0.5)H$) oldukça altında ($\Delta y = \%0.02H$) gerçekleşmiştir [16].

3. Çivilerdeki şekil değiştirme ölçerlerde kazı seviyesine bağlı olarak en fazla 300×10^{-6} birim eksenel şekil değiştirme (ε) ölçülmüş olup çivilerin bulunduğu seviyeye bağlı olarak en fazla $N=30$ kN mertebelerinde eksenel yük aldığı tespit edilmiştir.

4. Kazı, bekleme ve yükleme sırasında çivilerde oluşan en büyük toplam eksenel kuvvet (~30 kN) güvenilir çivi kapasitesinin (~56 kN) ancak %50'sine ulaşabilmiştir.

5. Yukarıdaki tespitler model deney tasarımında kırıklı çatlaklı kumtaşı birim için öngörülen kayma mukavemeti ve rijitlik parametrelerinin çok güvenli tarafta seçildiğini göstermektedir. Bu durum eldeki geoteknik araştırmaların nitelik ve sayısı ile kumtaşı birimin süreksizlik ve ayrışma durumunun göz önünde bulundurulmasından kaynaklanmıştır.

6. Çivi çekme deneyinde belirlenen maksimum kayma gerilmesi güncel literatürde kumtaşı için önerilen sürtünme direnci q_s=200-300 kPa aralığındadır [6]. Model deneyin tasarımında öngörülen çivi sürtünme direnci bu aralığın alt sınırında (200 kPa) olup ölçülen maksimum sürtünme direnci olan q_s=265 kPa'ın altındadır. Sahadaki çatlaklı zayıf kaya özelliklerindeki mekansal değişim dikkate alınarak bu değerin güvenli tarafta seçilmesinin uygun bir mühendislik yaklaşımı olduğu söylenebilir.

7. Çivilerdeki şekil değiştirmeler ve buna bağlı olarak hesaplanan eksenel kuvvetler çivi boyunca kafadan uca doğru gidildikçe azalmaktadır. Ayrıca çivi boyunca oluşan eksenel şekil değiştirmeler kazı derinliğine bağlı olarak artmaktadır. Bu tespitler literatür ile uyumludur.

8. Sürşarj yüklemesinde çivilerde eksenel yük artışları gözlenmiştir. Bu artışlar çivilerin konumlarına göre değişkenlik göstermektedir. Sürşarja yakın olan çivilerin kafa bölgelerinde eksenel basınç oluştuğu görülmüştür.

9. Limit dengeye dayalı stabilite analizleri ve gerilme şekil değiştirmeye dayalı sayısal analizler ile geri analizler yapılarak bu zayıf kaya ortamındaki çivilerle destekli kazının davranışı ve çivilerin performansına ilişkin yararlı bilgiler elde olunabilir ve buradan tasarıma yönelik çıkarımlarda bulunulabilir.

10. Yukarıda belirtilen sonuçlar ışığında çatlaklı-eklemli kayalarda yapılan derin kazılarda zemin çivisi kullanımının uygun ve güvenli bir mühendislik çözümü olduğu anlaşılmaktadır.

Semboller

RQD (%)	Kayaç kalite değeri
I_{s_50}	Nokta yükleme indisi
E_s	Elastisite modülü
q_s	Sürtünme direnci
ε	Birim şekil değiştirme
T_{ult}	Çivi çekme yükü
L_{enj}	Enjeksiyonlu çivi boyu
A_{enj}	Enjeksiyon kesit alanı
T_{fark}	Eksenel yük farkı
E_{dk}	Kompozit kesit elastisite modülü
γ	Kaya birim hacim ağırlığı
q_u	Serbest basınç dayanımı
V_{s30}	Kayma dalga hızı
Δy	Yatay deplasman oranı
σ	Eksenel gerilme
D_{enj}	Çivi delgi çapı
E_{enj}	Enjeskiyon elestisite modülü
E_d	Donatı elastisite modülü
N_{maks}	Güvenli çivi kapasitesi
N	Çivi eksenel yükü
m_b, s, a	Heok-Brown sabitleri

Kaynaklar

[1] "Kazı Destek Yapıları Tasarım ve Uygulama Esasları (2022)". T.C. Çevre ve İklim Değişikliği Bakanlığı.

[2] Chang-Yu Ou, (2006)."Deep Excavation, Theory and Practice". Vol. 3, p.57, Taipei, Taiwan.

[3] Stocker, M.F., Korber, G.W., Gässler, G., and Gudehus, G. (1979). "Soil Nailing". International Conference on Soil Reinforcement I, Paris, France, Vol. 2, 469-474.

[4] Schlosser, F. (1983). "Similarities and differences in the behavior and design of retaining structures of reinforced earth and soil nailing", Annales de L'Institut Technique de Bâtiment et des Travaux Publics, No. 418, Series: Sols et Fondations, Paris, France.

[5] French National Research Project Clouterre. "Recommendations Clouterre", vol.2, 1991.

[6] Lazarte, C.A. et al. (2015). "Geotechnical Engineering Circular No. 7: Soil Nail Walls-Reference Manual" Report No. FHWA-NHI-14-007, Federal Highway Administration, Washington, DC 20590.

[7] Lin P., et al. (2020). "Mapping soil nail loads using Federal Highway Administration (FHWA) simplified models and artificial neural network technique". Canadian Geotech. J. 00: 1−19 (0000) dx.doi.org/10.1139/cgj-2019-0440.

[8] Windsor C.R. (1997). "Rock reinforcement systems". International Journal of Rock Mechanics and Mining Sciences. https://doi.org/10.1016/S1365-1609(97)80004-4

[9] Ma Z., et al. (2017). "Rock burst assessment and prediction by dynamic and static stress analysis based on micro-seismic monitoring". International Journal of Rock Mechanics and Mining Sciences. https://doi.org/10.1016/j.ijrmms.2017.01.005

[10] Zheng H., et al. (2023). "A shear constitutive model and experimental demonstration considering dual void portion and solid skeleton portion of rock". International Journal of Rock Mechanics and Mining Sciences. https://doi.org/10.1016/j.engfracmech.2023.109066

[11] Sabatini, P. J., Pass, D. G., Bachus, R. C., (1999). "Ground Anchorages And Anchored Systems", FHWA Technical Report, FHWA-IF-99-015.

[12] Bieniawski, Z.T. (1989). Engineering rock mass classifications. New York: Wiley.

[13] RocLab 1.031. (2007). Rocscience Inc. Toronto, Canada.

[14] Luo, S. Q., Tan, S. A., and K.Y.Yong. (2000). "Pull-out resistance mechanism of a soil nail reinforcement in dilative soils." Soils and Foundation, Vol.40,(1).

[15] Lum W. C. W. (2007). "Static Pullout Behaviour of Soil Nails in Residual Soil". National University Of Singapore.

[16] Peck RB (1969) "Deep excavation and tunneling in soft ground". Proceedings of the seventh international conference on soil mechanics and foundation engineering, Mexico City, state of the art.

Dynamic-Mechanic Analysis and Rheological Modelling of Waste Face Mask Modified Bitumen

Ahmet Münir ÖZDEMİR[1*]
Erkut YALÇIN[2]
Mehmet YILMAZ[3]
Baha Vural KÖK[4]

ABSTRACT

Due to the Covid-19 global pandemic, the use of face masks has increased considerably in recent years. Used face masks are released into our environment and become a severe environmental threat. Therefore, researchers have focused on the recycling of waste face masks. Recently, studies have been carried out on the use of waste face masks as additives in bituminous materials, but a detailed rheological characterization has not been made. In this study, modified bitumens were obtained by adding 1%, 1.5%, 2%, 2.5%, and 3% waste face mask (WFM). Subsequently, frequency sweep test was performed on modified bitumen samples through a Dynamic Shear Rheometer (DSR). Thus, the viscoelastic behavior of WFM modified bitumen was investigated at different temperatures and loading rates. Performance analysis was conducted with rheological master curves, which were characterized according to analytical and mechanistic models. In this study, rheological evaluations were performed according to the Christensen-Anderson (CA) Model, Christensen-Anderson-Marasteanu (CAM) Model, Sigmoidal Model (SM), and finally, the mechanistic Huet-Sayegh Model (HSM). According to the results, it was determined that WFM significantly increased the rutting resistance of bitumen and performed better at low and high loading rates than the pure bitumen at each WFM ratio.

Keywords: Bitumen, waste face mask, dynamic shear rheometer, rheology, huet-sayegh model.

1. INTRODUCTION

Recently, the world has been facing a significant crisis due to the coronavirus (Covid-19) pandemic. To reduce the spread of Covid-19 and minimize its infectivity, personal protective equipment (PPE) (mask, gloves, face shield, etc.) is used. Due to the directives of the World Health Organization (WHO) and the rules enforced by governments, the use of masks has become almost proportional to the population. According to the WHO, 89 million masks are required each month to meet the demand due to Covid-19 [1,2]. China has increased the number of masks it produces daily to 14.8 million [3]. Fifty million face masks are produced weekly in Turkey [4]. The use of PPE reduces the spread of the virus; however, since the used equipment is disposable unless planned and adequate waste management is done, it causes environmental pollution and threatens the living spaces. It is estimated that 129 billion masks were discharged into the environment per month in June 2020 [5]. The daily use of masks is estimated to be 3.7 billion in Asia, 951 million in Africa, 891 million in Europe, 781 million in North America, and 591 million in South America. In addition, if expressed as tons per day, 11,308 masks are thrown in Asia, 2,855 in Africa, 2,674 in Europe, 2,346 in North America, and 1,776 in South America [6,7]. For more detailed statistical mask usage information, the study of Nzediegwu et al. can be examined [7]. Face masks are generally produced from polymers such as polypropylene, polyurethane, polyacrylonitrile, polystyrene, polycarbonate, polyethylene, and polyester [8]. This situation significantly contributes to the plastic waste problem in the world.

The first thing that comes to mind as waste material in our environment is plastic derivative materials. Plastic wastes can be partially used as aggregate in building materials. Waste materials are used in many construction materials and systems, from brick production to ground material [9–27]. Asphalt mixtures consist of non-renewable resources, especially binder. Thus, it is environmentally crucial to improve its properties or partially use the waste materials in the mixture. Bituminous binders are modified with various additives. Although polymers such as SBS, SEBS, and EVA are commonly preferred, organic and inorganic wastes are also used. Performance improvements can be achieved by using both bituminous binder and plastic waste in the mixture. In their study, Verapalumbo et al. used different percentages of waste plastic in bitumen and determined that waste plastic improved aging resistance, elasticity, and strength [28]. In another study, Genet et al. modified bitumen by adding waste LDPE plastic. Consequently, the mixture prepared with LDPE-modified bitumen presented a 33% higher stability value than the pure mixture [29]. Haider et al. investigated the moisture damage properties of mixtures obtained using waste plastic materials. Test results showed that adding high-density polyethylene increased the adhesion properties and moisture damage resistance [30]. Li et al. investigated the usability of waste plastics in asphalt mixtures as an anti-stripping agent. The results showed that the waste plastic increases the moisture resistance of the mixture; thus, it can be used as an anti-stripping agent [31]. In another study, researchers investigated the mechanical and thermal behavior of the bitumen by adding two different types of waste polyethylene. The results showed significant improvements in high-temperature performance parameters such as rutting compared to commercial polymer modified binders [32]. Yu et al. emphasized that energy savings can be achieved by using waste plastics in mixtures, and they examined the performance of direct-input waste plastic microscopically. According to the results, the direct-input waste plastic modifier can achieve micron-level dispersion in the bitumen [33]. Dalhat and Al-Abdul Wahhab investigated the effects of different plastic types such as

polypropylene, high- and low-density polyethylene (PP, HDPE, and LDPE)-recycled plastic wastes (RPW) on the viscoelastic properties of bitumen. It has been observed that all plastic wastes meet the specification limits and give better results than pure bitumen [34].

WFMs, resulting from the Covid-19 pandemic, has significant adverse effects on our environment. This case has led scientists to investigate the waste management of WFMs. Various studies have been carried out recently on the evaluation of waste masks released due to the Covid-19 pandemic in asphalt materials. Wang et al. added waste face masks to the asphalt mixture in their study and concluded that high resistance to rutting resistance was obtained. When the waste mask addition rate was 1.5%, the rutting depth value of the mixture decreased from 3.0 mm to 0.93 mm [35]. Zhang et al. carried out a study involving the use of waste masks with waste cooking oil. It was determined that the addition of the mask significantly increased the high temperature resistance, but decreased the low temperature performance. It was concluded that the use of waste cooking oil can relatively eliminate the low temperature disadvantage [36]. In another study, Zhao et al. obtained modified bitumen by adding waste masks to binder in various proportions. As a result of the rheological and physical experiments on pure and modified bitumen, it was determined that the addition of mask increased the complex modulus values of the bitumen, but decreased the phase angle values. In addition, as a result of imaging analysis, it was seen that asphalt and waste mask additive interacted well and formed a homogeneous mixture [37]. Yalçın et al. investigated the effect of waste mask addition on the performance properties of bitumen. It was observed that the rutting parameters increased as a result of the addition of masks at different rates by bitumen weight. In addition, the authors emphasized that mask addition of more than 2% gave better results than 3% SBS [38].

In the previous study of the research team, the effect of mask addition on the rheological behavior of the material was investigated with various experiments [38]. Rheology can be analyzed in two classes: experimental and theoretical. While experimental rheology explains the relationship between stress and strain rate in the laboratory environment, theoretical rheology explains the behavior of the material with mathematical models independent of its microscopic structure. For non-newtonian materials, these mathematical equations become more complex [39,40]. Since the waste face masks used in the study are polymer materials and polymer materials have non-newtonian character, their effects on bitumen behavior should be examined rheologically in detail. As seen in the literature, no detailed rheological characterization has been found in the studies on the addition of masks to bituminous materials. Based on this, a detailed rheological modeling and characterization of waste mask modified bitumen was made in this study. Waste face masks were divided into small pieces and added to bitumen at 1%, 1.5%, 2%, 2.5%, and 3% ratios. Frequency sweep test was applied through Dynamic Shear Rheometer to simulate different temperatures and loading rates. From the data, master curves were obtained to expand the frequency range further and analyze a wide frequency range. Afterwards, these master curves were interpreted with various rheological models.

2. MATERIALS AND METHOD

2.1. Bitumen

B 50/70 bitumen with a density of 1.015 g/cm^3 was utilized as a pure binder. The bitumen used in the study was obtained from TÜPRAŞ Batman Refinery. Conventional binder experiments were performed on the bituminous binder, including penetration, softening point, and rotational viscometer (RV). RV test was performed at 135°C and 165°C. The test results and the properties of bitumen are presented in Table 1.

Table 1 - Properties of B50/70 bitumen

Test	Unit	Standard	Results
Penetration	0.1 mm	AASHTO T 49	57
Softening Point	°C	AASHTO T 53-06	56.1
Flash Point	°C	TS EN ISO 2719	245
Density	g/cm^3	ASTM D70-18a	1.015
Solubility	Percentage	TS EN 12592	100
Rotational Viscosity			
135°C	cP	AASHTO T316	675
165°C	cP	AASHTO T316	175

2.2. Waste Face Mask (WFM)

Disposable face masks are manufactured using polymers including polyurethane, polyacrylonitrile, polycarbonate, polystyrene, polypropylene, polyester, polyethylene [41]. These masks consist of 3 layers: the outer layer (made up of nonwoven fibers that are mostly colorful and water-resistant), middle layer (i.e. melt-blown filter), and inner layer (i.e. soft fibers). The outer layer is composed of spunbond or thermo-nonwoven polypropylene fabric [42]. The outer layer, which should be water-repellent or impermeable, is usually harder and more colorable. The middle layer is made of melt-blown or spunbond non-woven propylene, PES (polysulfone) or their mixtures. The middle layer has a high fiber density and is a fluffy layer in order to ensure better filtration. The inner layer is composed of spunbond or thermo nonwoven propylene, PES, or their mixtures. The inner layer directly contacts the skin of the individual. There may be differences in the composition of the product among manufacturers. Masks used to obtain modified bitumen were collected in waste collection containers. As a result of preliminary studies on the persistence of the COVID-19 virus in homes, hospital environments, and on surfaces, it was revealed that the virus can live on surfaces or plastic items up to 72 hours following direct exposure [43]. For this reason, after the collected waste masks were kept in an isolated environment for 96 hours, they were completely ground except for the metal strips in the masks. The dimensions of the ground masks were 2-4 mm on average (Figure 1).

Figure 1 - Waste face mask (WFM) used in the study

2.3. Modification Process of Bitumen

In the study, modified bitumen was obtained by adding 1%, 1.5%, 2%, 2.5% and 3% WFM by weight of pure bitumen. The modification started by heating the pure bitumen at 180±5°C for half an hour to liquefy. Afterwards, the liquefied bitumen was poured into a 500 g metal mixing pot, which was kept at 180°C. Pure bitumen and WFM were mixed for 1 hour at 1000 rpm to obtain the modified bitumen [38].

2.4. Frequency Sweep Test via Dynamic Shear Rheometer (DSR)

Viscoelastic responses of the bituminous binder are characterized by determining the complex shear modulus (G*) and phase angle (δ) through the DSR test. G* is a measure of the resistance to deformations caused by repeated shear stresses in the binder. The complex shear modulus is defined by two parts: elastic modulus (G') and viscous modulus (G") [44]. These parts are associated with the G* and δ values. The phase angle equals the time difference between the applied stress and the resulting deformation. The material's behavior is assumed to be completely elastic when the phase angle is 0° and downright viscous when it is 90° [45] (Figure 2).

The frequency sweep test can simulate the speed of a vehicle moving on asphalt pavement. A loading frequency of 10 Hz corresponds to a speed of 60 km/h, while a loading frequency of 15 Hz corresponds to a speed of 90 km/h. The complex modulus and phase angle values vary significantly with temperature and frequency [46]. In this study, DSR tests were carried out on pure and WFM modified bitumen samples at four different temperatures (40°C, 50°C, 60°C, 70°C) and ten different frequencies (0.01-10Hz). Thus, the effect of waste mask addition on the viscoelastic character of bitumen was determined under different frequencies and temperatures. The sample geometry was determined to be 25mm in diameter and 1mm in height.
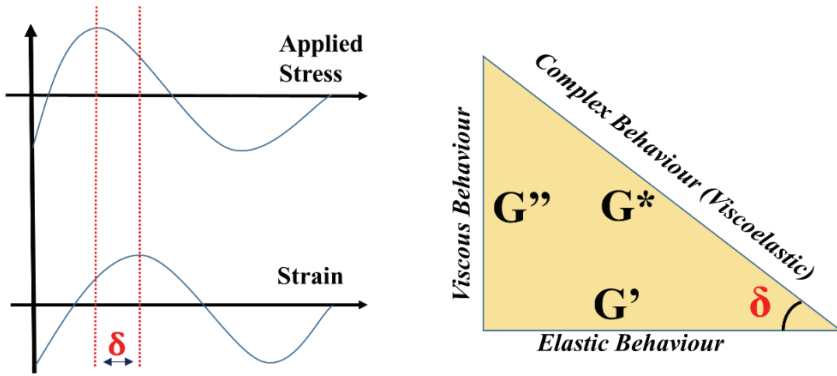
Figure 2 - Viscoelastic behaviour of bitumen

2.5. Christensen-Anderson (CA) Model

Cristensen and Anderson developed an empirical-analytical model in 1992 under the Strategic Highway Research Program (SHRP) to describe the rheological behavior of asphalt. In this model, presented in Equation 1, the rheological behavior is explained in terms of G* values as a function of the frequency applied to the bitumen. Although the model's primary purpose is to characterize pure bitumen, it has recently been used to describe the behavior of modified bitumen. Numerous studies have been conducted with the CA model [47–49]. CA model parameters are beneficial for analyzing conditions such as the effect of the additive used for modification, the effect of aging, and the effect of experimental inputs. Model parameters have physical meanings; thus, more meaningful evaluations can be made. A graphical representation of the CA model is given in Figure 3. It can be said that Figure 3 is also valid for the CAM model that is to be mentioned in Section 2.6.
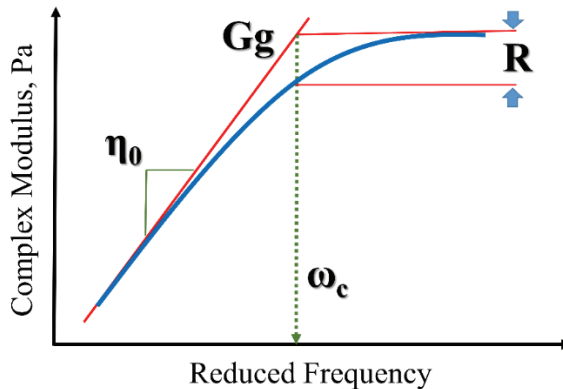
Figure 3 - Graphical representation of CA Model

$$|G^*| = G_g \left[1 + (\frac{\omega_c}{\omega})^{\frac{log2}{R}}\right]^{\frac{-R}{log2}} \qquad (1)$$

where G* is the complex shear modulus (Pa); G_g is the maximum G* (glassy modulus) (Pa); ω_c is the crossover frequency at the cross point; ω is the reduced frequency; R is the rheological index.

ωc represents the frequency at which the viscous and elastic modulus is the same. Furthermore, this point is where the viscous asymptote and the glassy asymptote overlap. ωc characterizes the overall hardness of bitumen. R is the difference between the complex modulus at ωc and the intersection asymptotes, which is also called shape factor. The increase in the R value indicates that the viscous properties of the binder decrease and become brittle at intermediate loading times and temperatures.

2.6. Christiensen-Anderson-Marasteanu (CAM) Model

The CAM model is an enhanced version of the CA model. CA model was modified to improve fitting performance at lower and higher frequency ranges, resulting in the CAM model. Many successful studies of the rheological characterization of binders use the CAM model [50–53]. The CAM model is presented in Equation 2:

$$|G^*| = G_g \left[1 + (\frac{\omega_c}{\omega})^v\right]^{\frac{-w}{v}} \qquad (2)$$

where *v* is the fitting parameter (equals log2/R seen in Equation 1); w is the parameter that deals with how fast or slow |G*| data. For example, when the frequency approaches zero, a bitumen with w>1 will reach the 90° asymptote faster than a bitumen with w<1.

2.7. Sigmoidal Model (SM)

The sigmoidal model is one of the most common models used to describe the rheological properties of bituminous binders. G* was characterized through SM as a function of frequency, as in the previously mentioned models. The SM is relatively simple compared to complex models, yet it adapts with sufficient accuracy. SM is given in Equation 3:

$$log|G^*| = v + \frac{a}{1+e^{\beta+\gamma(\log(\omega))}} \qquad (3)$$

where G* is the complex modulus; ω is the reduced frequency; *v* is the lower limiting modulus; α is the difference between upper and lower horizontal asymptote; β is the factor that controls the horizontal position of the inflection point; γ is the slope of the curve.

2.8. Huet-Sayegh Model (HSM)

In addition to empirical models, mechanistic models can describe the complex shear modulus thanks to their physical elements [54]. Maxwell, Kelvin, and Burger models are the main

mechanistic models explaining the behavior of asphaltic materials, generally viscoelastic materials. The Huet-Sayegh model is a mechanistic model with non-classical linear viscoelastic elements whose structural properties are defined by fractional derivatives. Fractional derivatives are used in solving physical problems and describing the rheological behavior of viscoelastic materials [55,56]. The structure of the HSM is shown in Figure 4, and the model equation is given in Equation 4 [57].
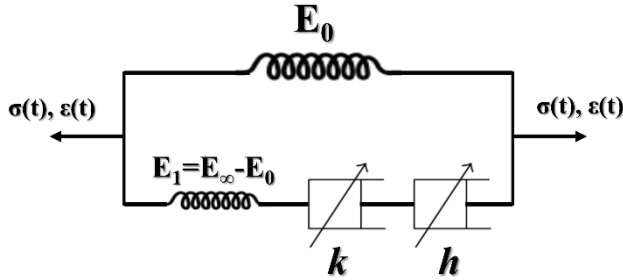
Figure 4 - The Huet-Sayegh model

The Huet-Sayegh model consists of two parallel branches, an elastic spring (E_0), and a branch consisting of three elements connected in series. While the elastic spring (E_0) represents the long-term elastic modulus when the frequency is zero, the other elastic spring (E_1) is the difference in instantaneous elastic modulus E_1 (frequency is infinite) and long-term modulus E_0 and two parabolic dashpots.

$$E^* = E_0 + \frac{E_1 - E_0}{1 + \delta(i\omega\tau)^{-k} + (i\omega\tau)^{-h}} \tag{4}$$

where ω is the reduced frequency; E_0 is the static modulus ($\omega \to 0$); E_1 is the glass transition modulus ($\omega \to \infty$); k and h are paremeters ($0 < k < h < 1$); δ is a dimensionless constant and τ is the characteristic time; and $i^2 = -1$.

3. EXPERIMENTAL STUDY

DSR tests were applied to pure and WFM modified bitumen at four different temperatures (40°C, 50°C, 60°C, and 70°C) and ten different frequencies in the 0.01-10 Hz frequency range. Afterwards, the results were processed according to the time-temperature superposition (TTSP) principle, and master curves were obtained at 40°C reference temperature (Fig. 5(a)). Furthermore, G* values at four different frequencies are presented in Figure 5 (b). Figure 6 shows a black diagram plotting phase angle values versus complex modulus values.

Figure 5 (a) shows that the complex shear modulus values increased with increasing frequency (loading speed). As the WFM content increased, the complex modulus values of bitumen increased. While the effect of the mask was more pronounced at low frequencies,
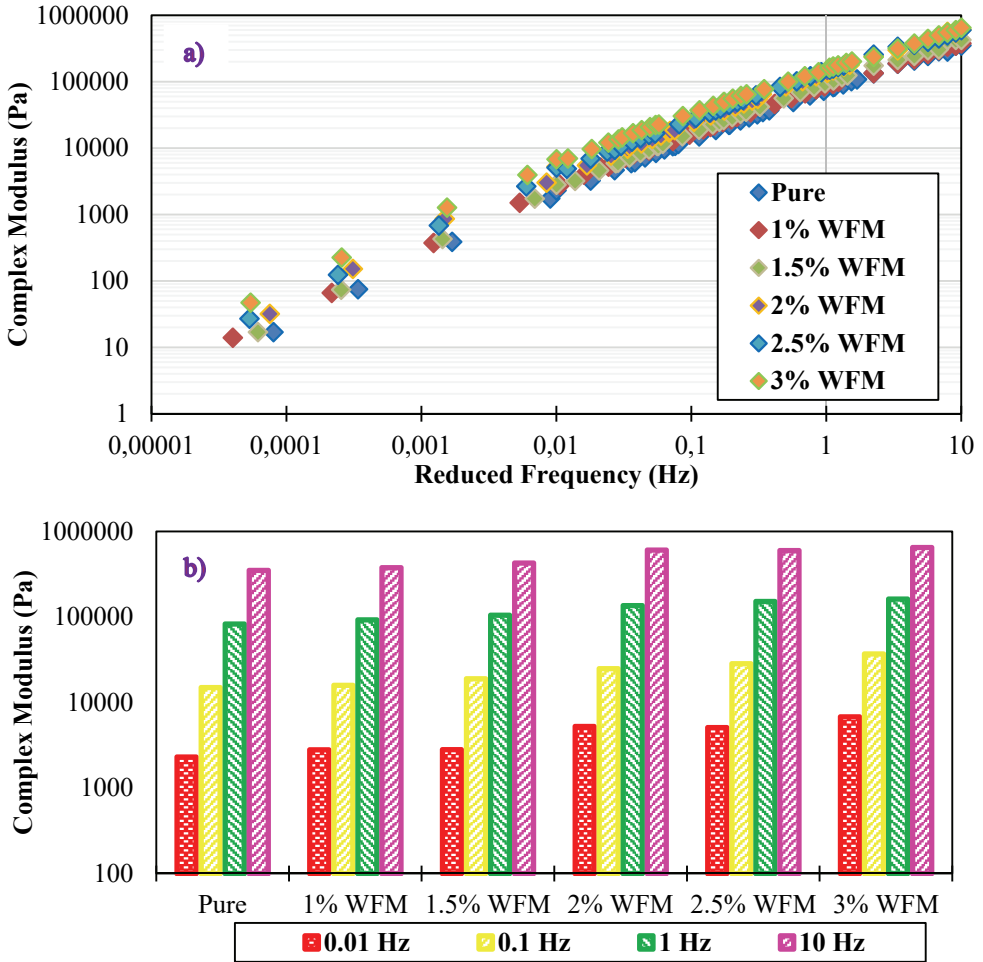
Figure 5 - a) TTSP master curves of pure and WFM modified asphalt binders,
b) complex modulus values at 0.01, 0.1, 1, and 10 Hz

the effect of WFM content decreased at high frequencies, and the complex modulus values became closer. Since both the horizontal and vertical axes are logarithmic in the graphs, the values are close, although the differences between the binders are apparent. Furthermore, as the amount of waste mask increased, the difference in complex modulus values became evident. The pure binder gives the lowest complex modulus value. As WFM increases, the overall resistance of the binders against deformation when subjected to shear load also increases. Total resistance to deformation was seen at most 3% of the WFM binder. To efficiently evaluate the complex modulus values of bitumens, master curve G^* values at frequencies of 0.01, 0.1, 1, and 10 Hz were given in Figure 5 (b). As seen in Figure 5 (b), the complex modulus values increased as the frequency and WFM content increased. The

changes in the G* values of binders are visible when the frequency changes. When Figure 5 is examined, compared to the pure binder, the G* values of the other binders increased more, especially after 2% WFM.
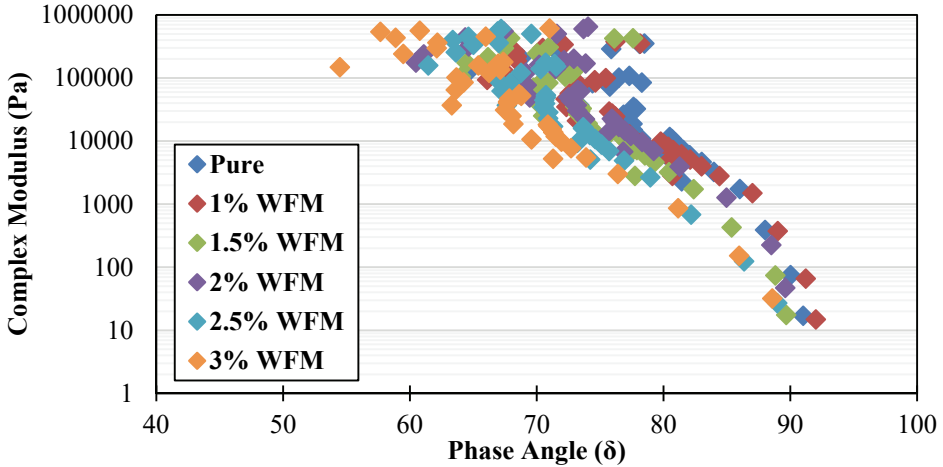
Figure 6 - Illustration of complex modulus-phase angle relationship (black diagram)

The black diagram, generated by data obtained at 40-70ºC, is given in Figure 6. The waste mask modification shows that curves create too much clutter and do not form a proper "S" shape, so it is a thermo-rheologically mixed material; therefore, it is a complex material. High phase angle values show that the time-temperature superposition is broken, and the material is transformed into a thermo-rheologically complex structure. At low phase angle values, i.e., at low temperatures, the waste mask modifications shift slightly to the left of the diagram relative to the pure binder, meaning they are slightly more elastic. Low phase angle and high G* values indicate that binders behave more elastic. When Figure 6 is examined, the phase angle values have increased with the decrease in the G* values in the pure bitumen. Considering the modified bitumens, the phase angle values have reached the lowest level, and the phase angle values have increased regularly, especially in G* values of 1.0E + 4 Pa and 1.0E + 5 Pa, especially as the WFM content increases. In WFM modified bitumen, the G* values increase up to 1.0E+5 Pa after decreasing phase angle values. The phase angle value in the 3%WFM binder was around 60-70°.

4. RESULTS AND DİSCUSSİONS

4.1. Christiensen-Anderson (CA) Model results

The analysis of the master curves of asphalt binders pure and containing 1%, 1.5%, 2%, 2.5%, 3% WFM with CA Model is given in Figure 7. Also, all CA Model curves are presented collectively in Figure 8. Rheological model parameters are given in Table 2.
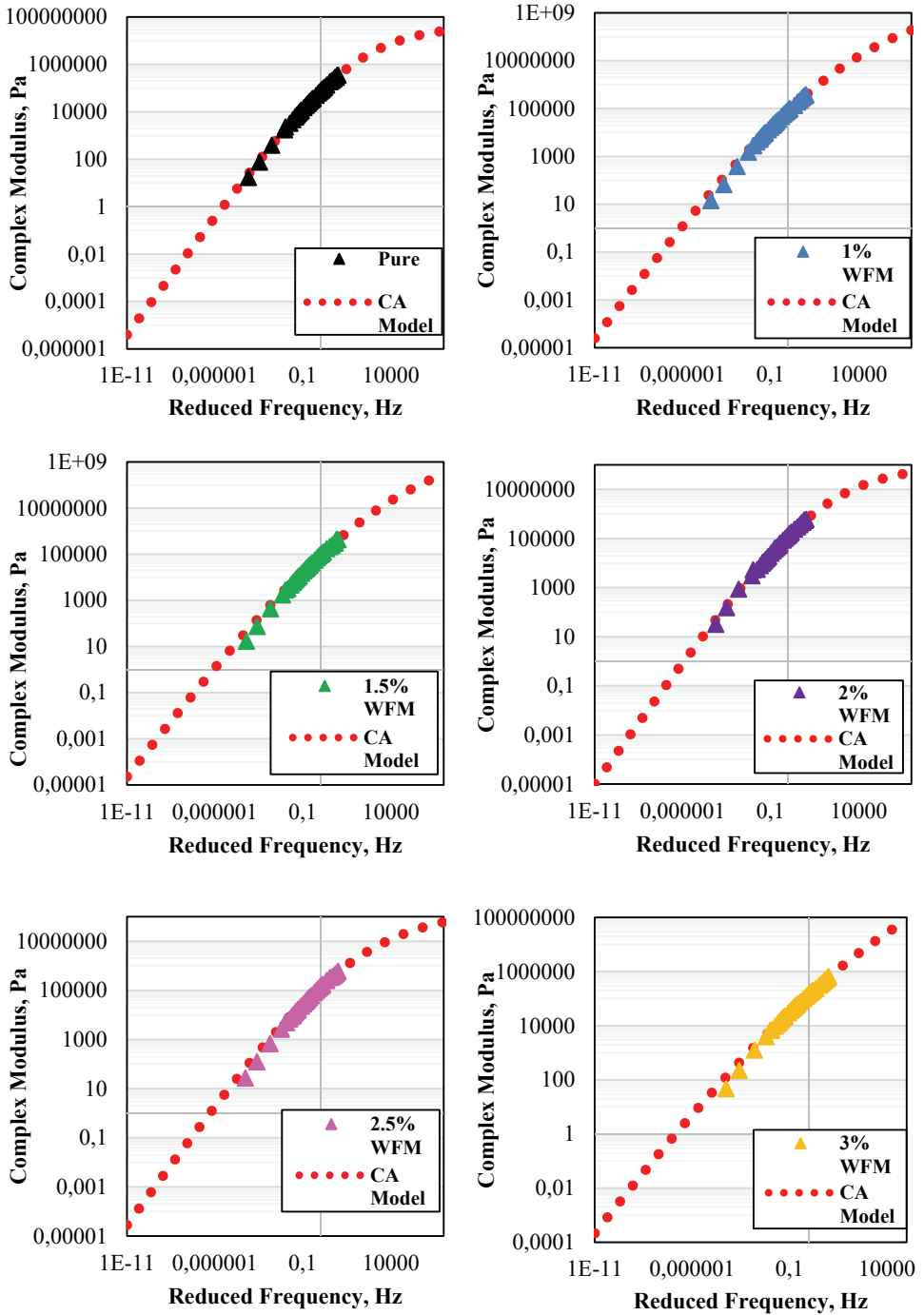
Figure 7 - CA model results of pure and 1, 1.5, 2, 2.5, 3% WFM modified asphalt binders
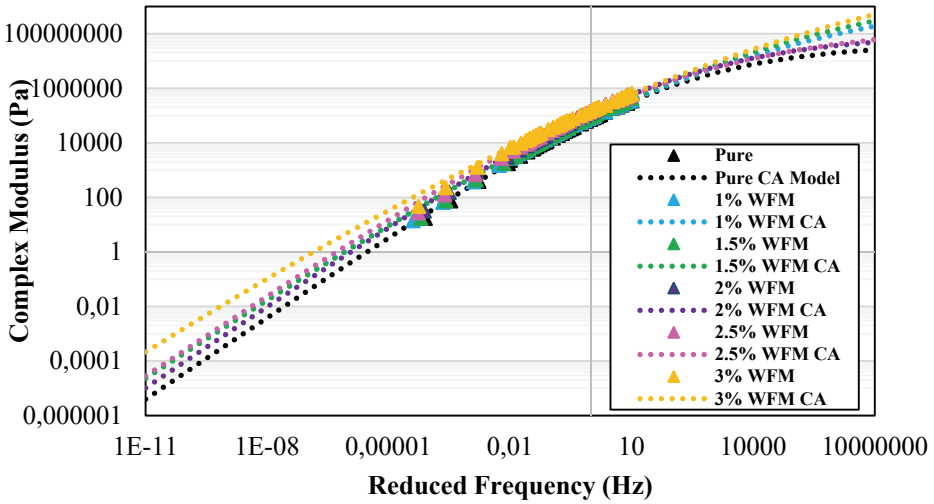
Figure 8 - Illustration of whole CA model curves

Table 2 - CA model parameters of pure and modified binder samples

	Gg	ωc	R	Coefficient of determination
Pure	1×10^9	104.89	2.611	0.98
1% WFM	1×10^9	1398.92	2.360	0.99
1.5% WFM	1×10^9	3290.97	2.186	0.96
2% WFM	1×10^9	3666.48	2.079	0.97
2.5% WFM	1×10^9	4098.21	1.544	0.97
3% WFM	1×10^9	4294.23	0.647	0.99

When Figure 7 is examined, it is clearly seen that the master curves have been successfully fitted with the CA model ($R^2 > 0,95$). The pure binder is closer to the model curve in the initial frequency values, but there is little deviation in the other binder contents. This case led to the difference in CA model parameters. Thus, rheological characterization between pure and modified binders was possible. In Figure 8, whole master curves and CA model curves were given together. According to Figure 8, the differentiation and modification effect of very low and very high frequency values can be clearly seen. In the CA model curve of 3% WFM modified bitumen, separation is evident at the lowest and highest frequency values. CA model parameters was given in Table 2. Various studies have been carried out to obtain 1 GPa at shear strength of the glassy modulus (Gg), and it has been determined that most binders offer this value. In previous studies, it has been suggested to fix the glassy modulus (Gg) value to 10^9. Most bitumen has a Gg value of 10^9. In this study, the Gg value was fixed to 10^9, and other parameters (ωc and R) were released. ωc is a binder-specific value and can be defined as a measure of the overall consistency of bitumen. When the crossover frequency

(ωc) values are examined (Table 2), it is seen that ωc also increases with the increase in the WFM rate. This is interpreted as the modification mechanism is formed, and the material hardens with the addition of WFM, confirming the penetration and softening point results. The rheological index (R) can be used to describe the shape of the master curve. R is associated with the width of the relaxation spectrum [58]. In addition, this parameter is a beneficial tool because of its sensitivity to bitumen hardness variations in loading time/frequency. Even small changes in bitumen hardness due to aging and chemical changes produce significant changes in R values [52]. In Table 2, it was seen that R values decreased as the amount of WFM increased.

4.2. Christiensen-Anderson-Marasteanu (CAM) Model results

Figure 9 shows the CAM Model curves for pure and WFM modified asphalt binders. In Figure 10, a collective representation of all CAM curves is presented. Also, the CAM Model parameters are given in Table 3.
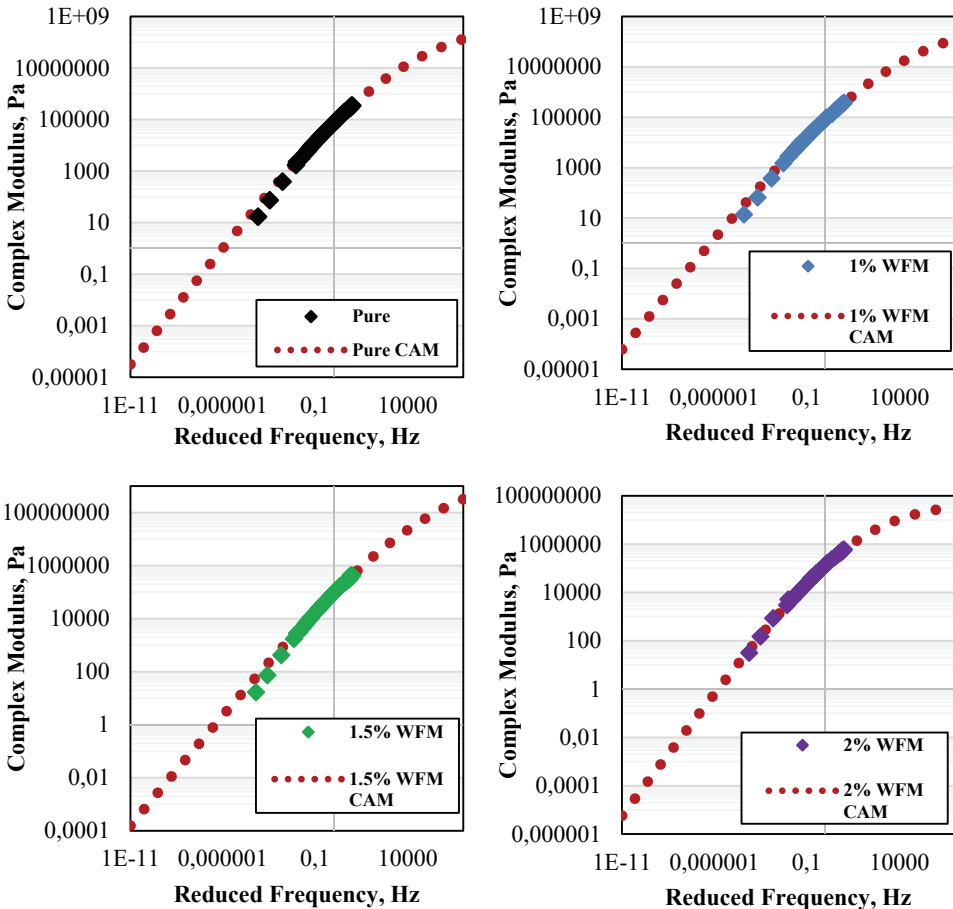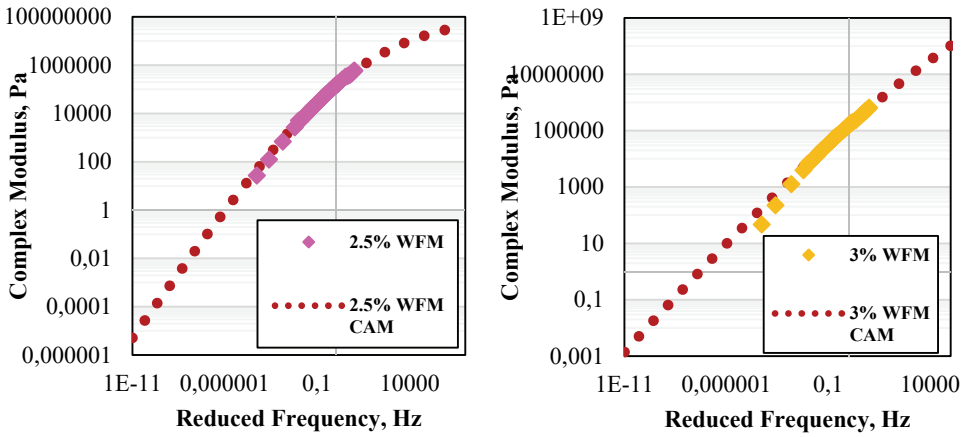
Figure 9 - CAM model results of pure and 1, 1.5, 2, 2.5, 3% WFM modified asphalt binders
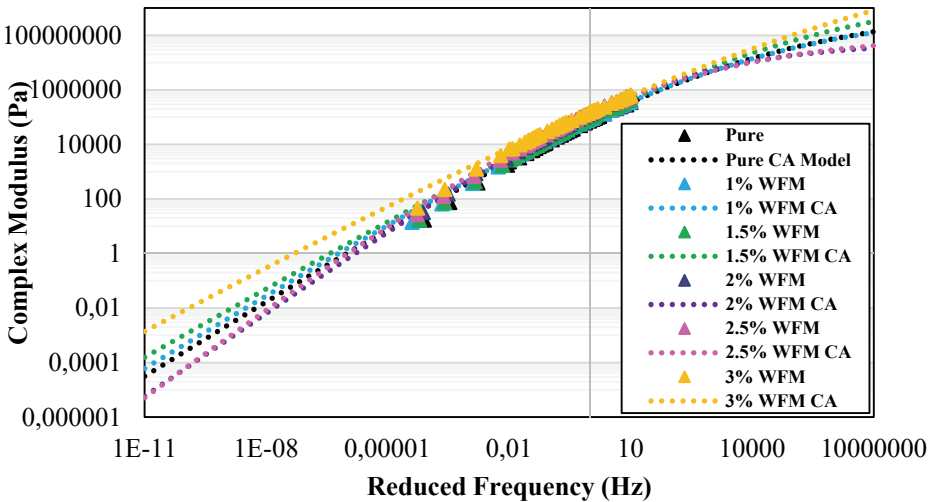
Figure 10 - Illustration of whole CAM model curves

Table 3 - CAM model parameters of pure and modified binder samples

	Gg	ωc	w	v	R²
Pure	$1x10^9$	3512,17	1,023	0,138	0,99
1% WFM	$1x10^9$	3695,97	0,900	0,136	0,99
1.5% WFM	$1x10^9$	8049,10	0,846	0,133	0,98
2% WFM	$1x10^9$	49067,21	0,877	0,135	0,99
2.5% WFM	$1x10^9$	94487,14	0,798	0,141	0,97
3% WFM	$1x10^9$	170603,01	0,818	0,139	0,96

4.3. Sigmoidal Model (SM) results

SM curves of pure and WFM modified asphalt binders are given in Figure 11. Figure 12 was plotted to investigate the rheological changes with increasing additive ratio. Also, SM parameters are given in Table 4.

In fact, the sigmoidal model is designed to define the dynamic modulus of asphalt mixtures. However, it is also widely preferred for binders. The SM model does not consistently achieve the desired performance in the master curve characterization of modified bitumens. Figure 11 shows the sigmoidal model curves of pure and 1%, 1.5%, 2%, 2.5%, and 3% WFM modified binder samples. When Figures 11 and 12 are examined, the formation of the Sigmoidal model in the form of "S" has been successful, and the complex modus values are highly accurate (min. $R^2 = 0,97$). According to Table 4, the value "v" is negative for all samples. This case is expected. A negative value of "v" means that complex modulus values are too low in low frequency and high-temperature conditions. Except for 1.5% WFM, the β value for whole samples is higher than the pure bitumen. This is attributed to the formation of a modification mechanism and the hardening of the material. The "γ" values are negative and almost identical in all samples. This indicates that the addition of WFM does not change the direction of the master curve.
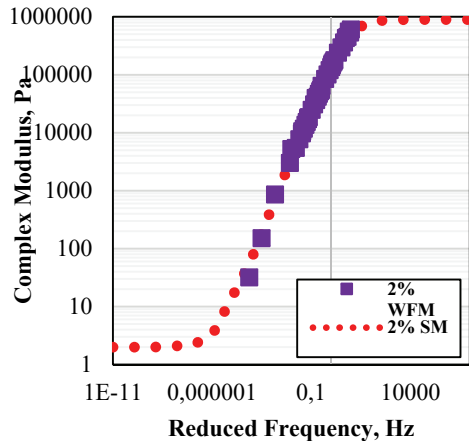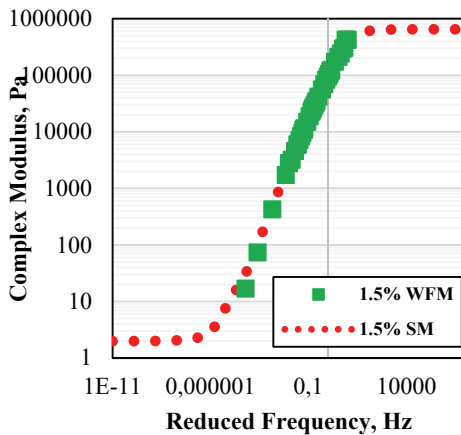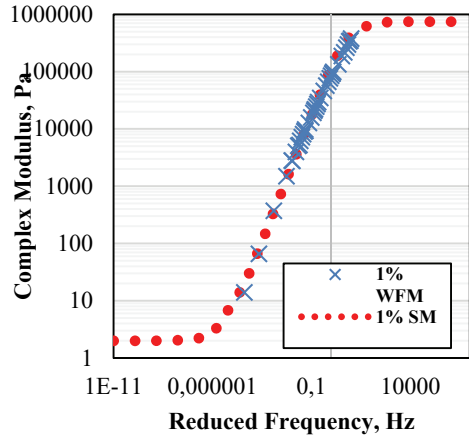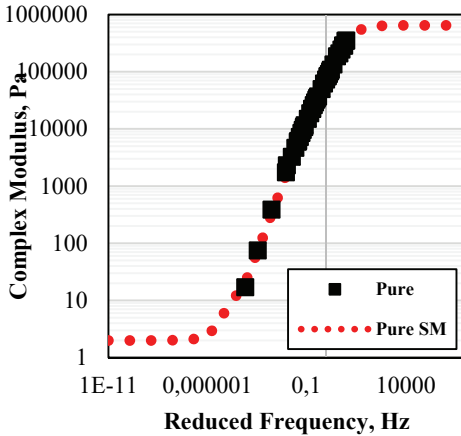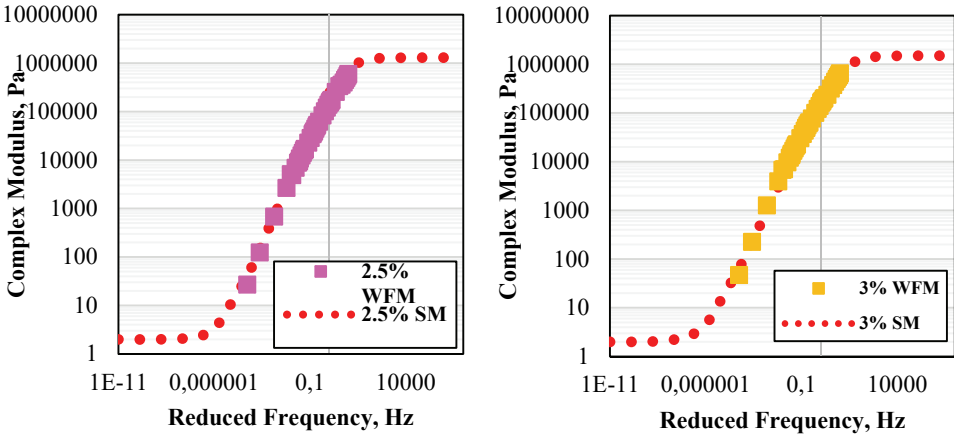
Figure 11 - SM model results of pure and 1, 1.5, 2, 2.5, 3% WFM modified asphalt binders
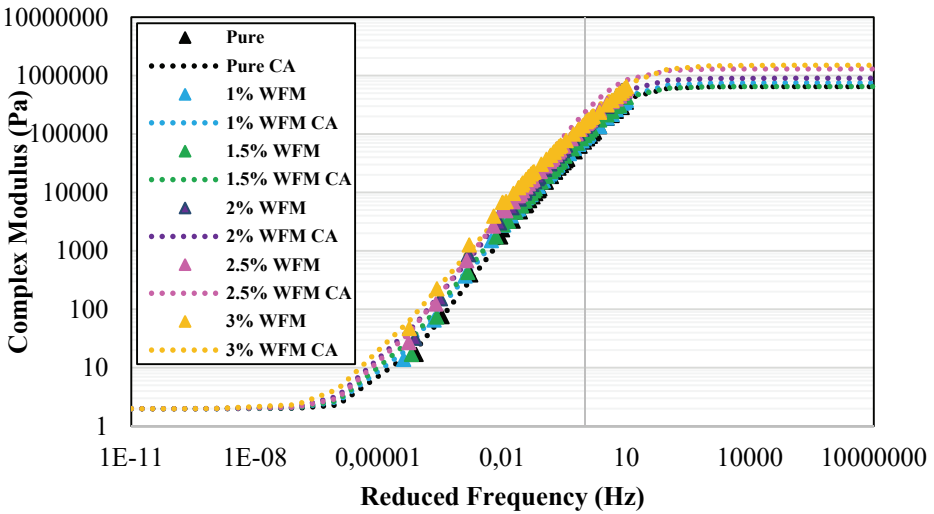
Figure 12 - Illustration of whole SM model curves

Table 4 - Sigmoidal model parameters of pure and modified binder samples

	ν	a	β	γ
Pure	2	650000	1,40	-2,15
1% WFM	2	750000	1,71	-2,05
1.5% WFM	2	650000	1,53	-2,05
2% WFM	2	900000	1,88	-2
2.5% WFM	2	1300000	2,11	-2,1
3% WFM	2	1500000	2,00	-1,9

4.4. Huet-Sayegh Model (HSM) results

Master curves of pure and 1%, 1.5%, 2%, 2.5%, and 3% WFM added bitumens were fitted to the mechanistic Huet-Sayegh model. The results are given in Table 5 and Figure 13.
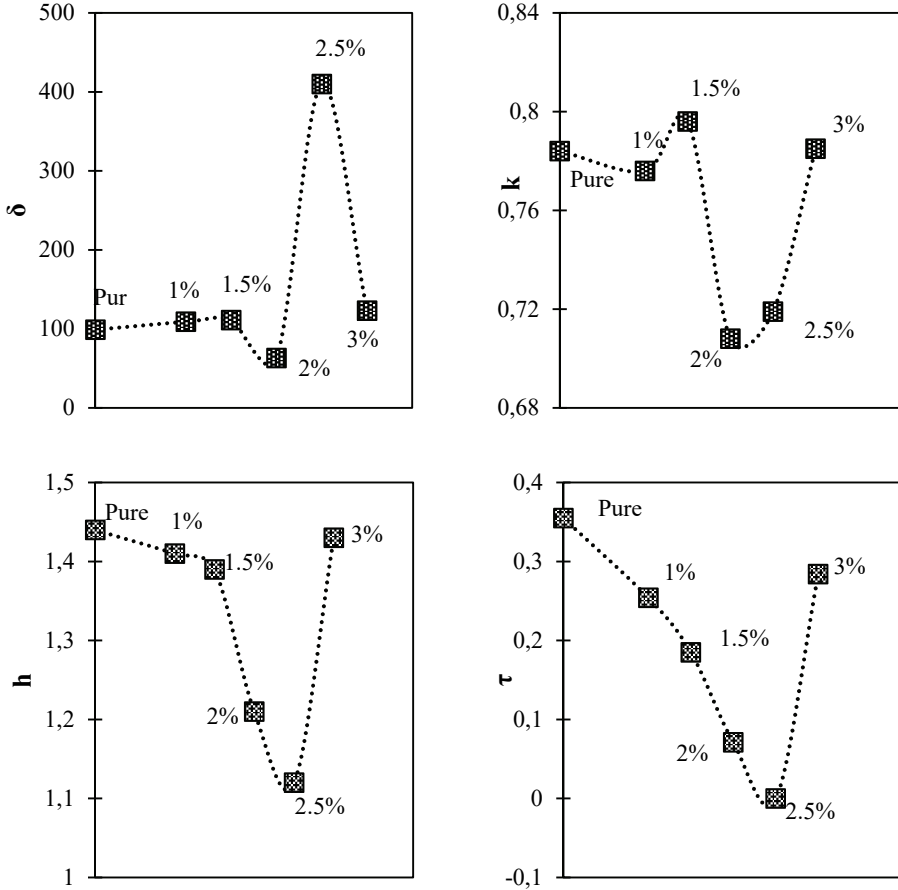
Figure 13 - Huet-Sayegh model parameters with different WFM contents

Table 5 - Huet Sayegh mechanistic model parameters (Reference Temperature = 40°C)

	E0	E1	δ	k	h	τ
Pure	$2{,}91 \times 10^{-31}$	3,70E+06	99,18	0,784	1,440	0,355
1% WFM	$8{,}76 \times 10^{-36}$	5,70E+06	109,5	0,776	1,406	0,254
1.50% WFM	$4{,}67 \times 10^{-39}$	8,36E+06	111,89	0,796	1,398	0,185
2% WFM	7,17	1,51E+09	224,40	0,708	1,207	0,071
2.50% WFM	1,31	1,98E+09	410,064	0,719	1,121	5,04E-05
3% WFM	$5{,}76 \times 10^{-38}$	2,15E+09	123,282	0,785	1	0,284

Some assumptions can be made for E_0 and E_1 values. It is known that there are studies in the literature where E_0 is equal to zero and E_1 is equal to 1 GPa. In this study, both values were released, the fitting process was performed, and other model parameters were obtained. When Table 5 is examined, the static modulus (E_0) values are almost zero for all bitumen samples. As the angular frequency goes to infinity, the glass transition module E_1 is mentioned. It was observed that E_1 values increased with the use of WFM, and this was interpreted as an indication that the bitumen hardened and its strength increased. "k" and "h" are two crucial parabolic creep parameters in viscoelastic characterization. According to Table 5, the k and h parameters are almost the same for all binder samples. This result shows that the modification process does not cause any change in the shape and direction of the master curves. If explicitly evaluated, it is possible to interpret the decrease in h value as a decrease in viscous properties [59]. An increase in δ indicates that the material has hardened. When the results were examined, the increase in the WFM ratio increased the δ values, confirming the traditional binder test results. The reduction in the 3% WFM sample is considered to be an error due to a concentration in the data.

5. CONCLUSIONS

In this study, the usability of waste face masks (WFM), which has emerged due to the Covid-19 pandemic that recently affected the world, was investigated as a bitumen additive. WFMs were divided into small pieces and afterwards added to the bitumen at the rates of 1%, 1.5%, 2%, 2.5%, and 3%. The modified bitumen samples were subjected to frequency sweep test through Dynamic Shear Rheometer (DSR). After the DSR test, rheological characterization was conducted using analytical and mechanistic models. The results were given as follows:

- Compared to the pure binder, higher G* values were obtained by adding WFM. Furthermore, a steady increase was observed in direct proportion to the PDG content. The addition of WFM resulted in more rutting-resistant asphalt binders.

- Master curves have been successfully obtained to evaluate the response of the bitumens at very high and very low frequency values in a broader range. With the increase in frequency, higher G* values were obtained. The increase in WFM content showed a higher complex modulus value at almost every frequency compared to the pure binder.

- Four different rheological models (CA, CAM, SM, HSM) were successfully applied to the results ($R^2 > 0,98$). To summarize;

- According to the CA model, the crossover frequency (ωc) values increased with the increase in WFM content. This indicates that the bitumen hardening occurs due to the modification process. When the CAM Model parameters were examined, it was determined that adding WFM increased the inclination to elastic behavior. According to the SM Model results, it can be said that no negativity has occurred in the shape and direction of the master curves. The HSM results showed that mechanistic models could successfully apply to WFM modified bitumen.

- When the models are compared among themselves, it is seen that for the CA and CAM Models, both provide highly accurate results ($R^2 > 0.96$). In addition, the ωc value increased with the increase in the additive ratio in both models. When the CA Model results were analyzed, it was observed that the R value decreased with the use of

additives, which was interpreted as the additive caused hardening of the bitumen. Based on this, it is interesting that the highest value of "w" among the CAM Model parameters was obtained in pure bitumen. A higher value of "w" means that it approaches 90°, in other words, the viscous asymptote, faster. In other words, it can be said that pure bitumen is less prone to elastic behavior.

- When the sigmoidal model results are compared with other rheological models, it is seen that it does not provide very accurate results at low frequencies. It was observed that SM and G* value did not give correlated results until the frequency value reached the range of 10^{-5}-10^{-6} Hz. The same situation is also present at high frequency values. At this point, CA and CAM Models give more correlated results with G* values at very low and very high frequencies.

- The Huet-Sayegh Model is a mechanistic model and thanks to its physical elements, it reflects the effect of polymer modification rheologically more efficiently. At this point, it is more preferable for viscoelastic materials compared to CA and CAM models. Future studies aim to investigate the relationship between various mechanistic models and the behavior of polymer modified bitumen.

Consequently, using face masks, which has increased considerably in recent years, creates environmental problems. With the use of waste masks in asphalt modification, both the properties of asphalt have been improved, and waste management has been achieved by evaluating an environmentally harmful waste material. It is aimed to evaluate the performance of the WFM modified mixture in future studies.

References

[1]   Fadare, O. O. and Okoffo, E. D., Covid-19 face masks: A potential source of microplastic fibers in the environment. Science Of The Total Environment, 737: 140279,2020 .

[2]   Internet: (WHO), W. H. O., Shortage of Personal Protective Equipment Endangering Health Workers Worldwide. https://www.who.int/news/item/03-03-2020-shortage-of-personal-protective-equipment-endangering-health-workers-worldwide (2021).

[3]   Internet: Xinhuanet, China Focus: Mask Makers Go All out in Fight against Novel Coronavirus. http://www.xinhuanet.com/english/2020-02/06/c_138760527.htm (2021).

[4]   Internet: Yagıcı Çiftci, M., Türkiye'de Haftada 50 Milyon Maske Üretiliyor. https://www.trthaber.com/haber/koronavirus/turkiyede-haftada-50-milyon-maske-uretiliyor-514410.html (2021).

[5]   Prata, J. C., Silva, A. L. P., Walker, T. R., Duarte, A. C., and Rocha-Santos, T., COVID-19 Pandemic Repercussions on the Use and Management of Plastics. Environmental Science & Technology, 54(13), 7760–7765,2020 .

[6]   Hantoko, D., Li, X., Pariatamby, A., Yoshikawa, K., Horttanainen, M., and Yan, M., Challenges and practices on waste management and disposal during COVID-19 pandemic. Journal Of Environmental Management, 286: 112140,2021 .

[7]   Nzediegwu, C. and Chang, S. X., Improper solid waste management increases potential for COVID-19 spread in developing countries. Resources, Conservation And Recycling, 161: 104947,2020 .

[8]   Potluri, P. and Needham, P., Technical textiles for protection. Textiles for Protection, Elsevier, 151–175 , 2005.

[9]   Ali, N., Mohd Yusup, N. F., Sheikh Khalid, F., Shahidan, S., and Abdullah, S. R., The Effect of Water Cement Ratio on Cement Brick Containing High Density Polyethylene (HDPE) as Sand Replacement. MATEC Web Of Conferences, 150: 03010,2018 .

[10]   Akinwumi, I. I., Domo-Spiff, A. H., and Salami, A., Marine plastic pollution and affordable housing challenge: Shredded waste plastic stabilized soil for producing compressed earth bricks. Case Studies In Construction Materials, 11: e00241,2019 .

[11]   Gangwar, P. and Tiwari, S., Stabilization of soil with waste plastic bottles. Materials Today: Proceedings, ,2021 .

[12]   Fang, C., Zhang, Y., Yu, Q., Zhou, X., Guo, D., Yu, R., and Zhang, M., Preparation, Characterization and Hot Storage Stability of Asphalt Modified by Waste Polyethylene Packaging. Journal Of Materials Science & Technology, 29(5), 434–438,2013 .

[13]   Fang, C., Zhang, M., Yu, R., and Liu, X., Effect of Preparation Temperature on the Aging Properties of Waste Polyethylene Modified Asphalt. Journal Of Materials Science & Technology, 31(3), 320–324,2015 .

[14]   Aldagari, S., Kabir, S. F., and Fini, E. H., Investigating aging properties of bitumen modified with polyethylene-terephthalate waste plastic. Resources, Conservation And Recycling, 173: 105687,2021 .

[15]   Ahmadinia, E., Zargar, M., Karim, M. R., Abdelaziz, M., and Ahmadinia, E., Performance evaluation of utilization of waste Polyethylene Terephthalate (PET) in stone mastic asphalt. Construction And Building Materials, 36: 984–989,2012 .

[16]   Cong, L., Yang, F., Guo, G., Ren, M., Shi, J., and Tan, L., The use of polyurethane for asphalt pavement engineering applications: A state-of-the-art review. Construction And Building Materials, 225: 1012–1025,2019 .

[17]   Du, Z., Jiang, C., Yuan, J., Xiao, F., and Wang, J., Low temperature performance characteristics of polyethylene modified asphalts – A review. Construction And Building Materials, 264: 120704,2020 .

[18]   Lastra-González, P., Calzada-Pérez, M. A., Castro-Fresno, D., Vega-Zamanillo, Á., and Indacoechea-Vega, I., Comparative analysis of the performance of asphalt concretes modified by dry way with polymeric waste. Construction And Building Materials, 112: 1133–1140,2016 .

[19]   Hake, S. L., Damgir, R. M., and Awsarmal, P. R., Utilization of Plastic waste in Bitumen Mixes for Flexible Pavement. Transportation Research Procedia, 48: 3779–3785,2020 .

[20]   Suganya, S., A Study on Mechanical Properties of fly ash Brick with Waste Plastic Strips. International Journal Of Applied Engineering Research, 10: ,2015 .

[21] Tapkire, G., Recycled plastic used in concrete paver block. International Journal Of Research In Engineering And Technology, 03(21), 33–35,2014 .

[22] Vanitha, S., Natarajan, V., and Praba, M., Utilisation of Waste Plastics as a Partial Replacement of Coarse Aggregate in Concrete Blocks. Indian Journal Of Science And Technology, 8(12), ,2015 .

[23] Xu, Y., Jiang, L., Xu, J., and Li, Y., Mechanical properties of expanded polystyrene lightweight aggregate concrete and brick. Construction And Building Materials, 27(1), 32–38,2012 .

[24] Marian, S. and R., V. J., Use of e-plastic waste in concrete as a partial replacement of coarse mineral aggregate. Computers And Concrete, 21(4), 377–384,2018 .

[25] Aslani, F., Deghani, A., and Asif, Z., Development of Lightweight Rubberized Geopolymer Concrete by Using Polystyrene and Recycled Crumb-Rubber Aggregates. Journal Of Materials In Civil Engineering, 32(2), 04019345,2020 .

[26] Demirboga, R. and Kan, A., Thermal conductivity and shrinkage properties of modified waste polystyrene aggregate concretes. Construction And Building Materials, 35: 730–734,2012 .

[27] Abukhettala, M. and Fall, M., Geotechnical characterization of plastic waste materials in pavement subgrade applications. Transportation Geotechnics, 27: 100472,2021 .

[28] Veropalumbo, R., Russo, F., Oreto, C., Buonocore, G. G., Verdolotti, L., Muiambo, H., Biancardo, S. A., and Viscione, N., Chemical, Thermal, and Rheological Performance of Asphalt Binder Containing Plastic Waste. Sustainability, 13(24), 13887,2021 .

[29] Genet, M. B., Sendekie, Z. B., and Jembere, A. L., Investigation and optimization of waste LDPE plastic as a modifier of asphalt mix for highway asphalt: Case of Ethiopian roads. Case Studies In Chemical And Environmental Engineering, 4: 100150,2021 .

[30] Haider, S., Hafeez, I., Jamal, and Ullah, R., Sustainable use of waste plastic modifiers to strengthen the adhesion properties of asphalt mixtures. Construction And Building Materials, 235: 117496,2020 .

[31] Li, R., Leng, Z., Yang, J., Lu, G., Huang, M., Lan, J., Zhang, H., Bai, Y., and Dong, Z., Innovative application of waste polyethylene terephthalate (PET) derived additive as an antistripping agent for asphalt mixture: Experimental investigation and molecular dynamics simulation. Fuel, 300: 121015,2021 .

[32] Kakar, M. R., Mikhailenko, P., Piao, Z., Bueno, M., and Poulikakos, L., Analysis of waste polyethylene (PE) and its by-products in asphalt binder. Construction And Building Materials, 280: 122492,2021 .

[33] Yu, L., Lyu, L., Li, R., Du, Y., and Pei, J., Microscopic Mechanism of Direct-Input Waste Plastic Modified Asphalt. Journal Of Transportation Engineering, Part B: Pavements, 148(2), ,2022 .

[34] Dalhat, M. A. and Al-Abdul Wahhab, H. I., Performance of recycled plastic waste modified asphalt binder in Saudi Arabia. International Journal Of Pavement Engineering, 18(4), 349–357,2017 .

[35] Wang, G., Li, J., Saberian, M., Rahat, M. H. H., Massarra, C., Buckhalter, C., Farrington, J., Collins, T., and Johnson, J., Use of COVID-19 single-use face masks to improve the rutting resistance of asphalt pavement. Science Of The Total Environment, 826: 154118,2022 .

[36] Zhang, D., Guo, Y., Liu, Z., Xu, P., Ma, Z., and Zhan, J., Laboratory investigation on added-value application of the COVID-19 disposable mask in hot mix asphalt (HMA). Science Of The Total Environment, 860: 160243,2023 .

[37] Zhao, Z., Wu, S., Liu, Q., Xie, J., Yang, C., Wang, F., and Wan, P., Recycling waste disposable medical masks in improving the performance of asphalt and asphalt mixtures. Construction And Building Materials, 337: 127621,2022 .

[38] Yalcin, E., Munir Ozdemir, A., Vural Kok, B., Yilmaz, M., and Yilmaz, B., Influence of pandemic waste face mask on rheological, physical and chemical properties of bitumen. Construction And Building Materials, 337: 127576,2022 .

[39] Hsissou, R., Hilali, M., Dagdag, O., Adder, F., Elbachiri, A., and Rafik, M., Rheological behavior models of polymers. Biointerface Research In Applied Chemistry, 12(1), 1263–1272,2022 .

[40] Hsissou, R., Benzidia, B., Hajjaji, N., and Elharfi, A., Elaboration and Electrochemical Studies of the Coating Behavior of a New Nanofunctional Epoxy Polymer on E24 Steel in 3.5 % NaCl. Portugaliae Electrochimica Acta, 36(4), 259–270,2018 .

[41] Potluri, P. and Needham, P., Technical textiles for protection BT - Textiles for Protection. Textiles for Protection, 151–175 , 2005.

[42] Internet: İHKİP, Maske, Cerrahi Örtü, Önlükler ve Koruyucu Giysilerde Uyulması Gereken Standartlar. https://www.ihkib.org.tr/fp-icerik/ia/d/2020/05/06/maske-ve-koruyucu-giysi-bilgilendirme-ekoteks-04-05-2020-son-202005061258300443-cdd4a-202005061705110837-FAC50.pptx .

[43] van Doremalen, N., Bushmaker, T., Morris, D. H., Holbrook, M. G., Gamble, A., Williamson, B. N., Tamin, A., Harcourt, J. L., Thornburg, N. J., Gerber, S. I., Lloyd-Smith, J. O., de Wit, E., and Munster, V. J., Aerosol and Surface Stability of SARS-CoV-2 as Compared with SARS-CoV-1. New England Journal Of Medicine, 382(16), 1564–1567,2020 .

[44] Zaniewski, J. and Pumphrey, M., Evaluation of Performance Graded Asphalt Binder Equipment and Testing Protocol. ,2004 .

[45] Yalçın, E., Saf ve Modifiye Bitümlerin Farklı Frekans ve Sıcaklıklardaki Reolojik Özelliklerinin İncelenmesi. Bitlis Eren Üniversitesi Fen Bilimleri Dergisi, 9(2), 901–909,2020 .

[46] Huang, W., Wang, D., He, P., Long, X., Tong, B., Tian, J., and Yu, P., Rheological Characteristics Evaluation of Bitumen Composites Containing Rock Asphalt and Diatomite. Applied Sciences, 9(5), 1023,2019 .

[47] Christensen, D. W., Anderson, D. A., and Rowe, G. M., Relaxation spectra of asphalt binders and the Christensen–Anderson rheological model. Road Materials And Pavement Design, 18(sup1), 382–403,2017 .

[48] Liu, F., Zhou, Z., and Zhang, X., Linking chemical to rheological properties of asphalt binder with oxidative aging effect. Road Materials And Pavement Design, 22(9), 2014–2028,2021 .

[49] Zhao, K. and Wang, Y., Influences of aging conditions on the rheological properties of asphalt binders. International Journal Of Pavement Engineering, 21(5), 653–665,2020 .

[50] Teltayev, B. and Radovskiy, B., Predicting thermal cracking of asphalt pavements from bitumen and mix properties. Road Materials And Pavement Design, 19(8), 1832–1847,2018 .

[51] Hou, H., Wang, T., Wu, S., Xue, Y., Tan, R., Chen, J., and Zhou, M., Investigation on the pavement performance of asphalt mixture based on predicted dynamic modulus. Construction And Building Materials, 106: 11–17,2016 .

[52] Cholewińska, M., Iwański, M., and Mazurek, G., The impact of ageing on the bitumen stiffness modulus using the CAM model. The Baltic Journal Of Road And Bridge Engineering, 13(1), 34–39,2018 .

[53] Ma, X., Chen, H., Gui, C., Xing, M., and Yang, P., Influence of the properties of an asphalt binder on the rheological performance of mastic. Construction And Building Materials, 227: 116659,2019 .

[54] Xu, Q. and Solaimanian, M., Modelling linear viscoelastic properties of asphalt concrete by the Huet–Sayegh model. International Journal Of Pavement Engineering, 10(6), 401–422,2009 .

[55] Zbiciak, A., Michalczyk, R., and Brzeziński, K., Time–temperature superposition for viscoelastic materials with application to asphalt–aggregate mixes. International Journal Of Environmental Science And Technology, 16(9), 5059–5064,2019 .

[56] Di Mino, G., Airey, G., Di Paola, M., Pinnola, F. P., D'Angelo, G., and Lo Presti, D., Linear and nonlinear fractional hereditary constitutive laws of asphalt mixtures. Journal Of Civil Engineering And Management, 22(7), 882–889,2016 .

[57] Olard, F. and Di Benedetto, H., General "2S2P1D" Model and Relation Between the Linear Viscoelastic Behaviours of Bituminous Binders and Mixes. Road Materials And Pavement Design, 4(2), 185–224,2003 .

[58] Socal da Silva, L., de Camargo Forte, M. M., de Alencastro Vignol, L., and Cardozo, N. S. M., Study of rheological properties of pure and polymer-modified Brazilian asphalt binders. Journal Of Materials Science, 39(2), 539–546,2004 .

[59] Mazurek, G., The Viscoelastic Characteristics of the Asphalt Concrete Modified with Different Synthetic Waxes Using a Modified Huet- Sayegh Model. (2017).

Behavior of Base-Isolated Liquid Storage Tanks with Viscous Dampers under Historical Earthquakes Considering Superstructure Flexibility

Elif GÜLER[1]
Cenk ALHAN[2*]

ABSTRACT

Liquid storage tanks (LSTs) can be efficiently protected from far-fault earthquakes by base-isolation. However, large isolation system and sloshing displacements may threaten the tank's safety under near-fault earthquakes. Although the application of supplemental viscous dampers (VDs) at the base-isolation systems of LSTs located in near-fault areas may help, it may also increase superstructure demands under far-fault earthquakes. In addition to the characteristics of the earthquake, the isolation system and the superstructure properties may affect the success of base-isolated LSTs with supplemental VDs. Therefore, a numerical investigation is conducted in this study in order to determine the influence of the supplemental viscous damping ratio, the isolation system period, the tank wall flexibility, and the tank slenderness ratio on the seismic responses of base-isolated cylindrical steel LSTs with supplemental VDs including the base displacement, the sloshing displacement, and the normalized isolation system shear force under both near-fault and far-fault historical earthquake records. The tank is modeled by single-degree-of-freedom systems representing different modes on a common isolation basemat and the nonlinear dynamic analyses are carried out in 3D-BASIS-ME software. Findings show that while supplemental damping is required especially when LSTs with long-period isolation systems are subjected to large magnitude near-fault earthquakes, it may also cause amplifications in the sloshing displacement and isolation system shear force demands in case of far-fault earthquakes. Furthermore, it is determined that the influence of tank flexibility on both the superstructure and the isolation system responses is negligibly small while the tank slenderness ratio may have considerable effects.

Keywords: Liquid storage tank, base-isolation, supplemental viscous damper, near-fault earthquake, parametric analysis.

1 Maltepe University, Department of Civil Engineering, Istanbul, Türkiye
  elifguler@maltepe.edu.tr - https://orcid.org/0000-0001-5261-5320

2 Istanbul University-Cerrahpaşa, Department of Civil Engineering, Istanbul, Türkiye
  cenkalhan@iuc.edu.tr - https://orcid.org/0000-0002-6649-8409

* Corresponding author

1. INTRODUCTION

Along with the development of the economy and the increase in the density of the population, liquid storage tanks (LSTs) are becoming widespread and increasing in size today in order to meet the needs of the society. The exposure of these tanks to earthquakes can cause significant failures such as structural collapse, loss of function, fire, hazardous material leak, environmental pollution, and groundwater contamination which affects various sections of industry such as nuclear, chemical, pharmaceutical, food, or oil [1-3]. For example, Hatayama [4] reported that the 2003 Tokachi-oki Japan Earthquake (M_w=8.0), which produced large-amplitude and long-period (4-8 s) ground motions, caused severe damage in the seven large oil storage tanks with floating roof structures, leading to dangerous situations such as ring fire, roof sinking, and open-top fire because of severe sloshing of oil. Yazici and Cili [5] mentioned that the 1999 Kocaeli Turkey Earthquake caused fires in the Tüpraş İzmit Refinery, damaging more than 30 floating-roof naphtha tanks and at the Habas plant, 2 elevated liquid oxygen tanks collapsed because of the detrimental effects of the earthquake on the reinforced concrete pedestal.

In recent years, employing base-isolation is suggested as an effective way for the earthquake-resistant design of the LSTs. There are many studies in the literature showing the effect of base-isolation on the seismic responses of LSTs from different perspectives. Jadhav and Jangid [6] compared the responses of LSTs isolated by laminated rubber bearings, lead-rubber bearings, and friction pendulum systems with those of non-isolated systems under real earthquake ground motions considering the effects of parameters such as the aspect ratio of the tank and the isolation period. They stated that the elastomeric bearings with lead cores exhibited the best performance. Furthermore, they demonstrated that the proposed approximate model for evaluating seismic responses provided satisfactory estimations. Shrimali and Jangid [7] concluded that the effects of non-classical damping are generally insignificant and the responses obtained through modal analysis using the classical damping approach can be accurately calculated. Additionally, their analyses conducted using the response spectrum method and a simplified approximate method proposed showed that the responses obtained are consistent with the exact responses. In their study, Jadhav and Jangid [8] subjected LSTs isolated with elastomeric bearings and sliding systems to the fault normal and parallel components of near-fault ground motions. They demonstrated that the fault normal component mainly governs the resultant response. Additionally, they examined the effects of parameters such as the aspect ratio of the tank, isolation period, and damping of the isolation bearings on the effectiveness of seismic isolation. They emphasized that increasing the damping beyond the optimum value may result in an increase in base shear. Shekari et al. [9] examined the behavior of cylindrical LSTs modeled using finite shell elements and boundary elements combined with base isolation systems consisting of bilinear hysteretic bearing elements under long-period ground motions. Through their analysis using an iterative and step-by-step algorithm, they found that significant reduction in dynamic responses may be achieved with such isolation systems. Panchal and Soni [10] evaluated the studies in the literature about the behavior of seismically isolated liquid storage tanks with various shapes and materials under seismic excitations. They noted that most studies have shown that isolating liquid storage tanks effectively reduces the impulsive response component while causing a small increase in the convective component but the studies are still insufficient on some subjects. They have suggested examples of topics that require further research in the future, such as investigating the impact of three-axis earthquake

excitation on the responses of isolated steel tanks containing multilayered liquid, analyzing and assessing the feasibility of semi-active control devices for the aseismic design of fluid storage ground and elevated steel tanks. Saha et al. [11] modeled the base-isolated cylindrical steel water storage tanks with the Response Surface Model in order to investigate the effect of the uncertainty in the mechanical parameters of lead rubber bearings on the peak seismic responses using fragility curves obtained via Monte Carlo simulation. They found that such uncertainties affect the peak response quantities and the probability of failure for the base-isolated liquid storage tanks reduces as the isolation period increases. Hashemi and Aghashiri [12] conducted seismic analyses of base-isolated flexible rectangular fluid containers made of concrete under horizontal ground motion using an equivalent mechanical model. They concluded that the base shear, wall deformation, and hydrodynamic pressure of the rectangular fluid containers could be effectively reduced by base-isolation but the surface sloshing height of the fluid in the container could be increased. Alhan et al. [13] investigated the effect of the characteristic strength ratio on the seismic response behavior of cylindrical steel LSTs seismically isolated with lead-rubber bearings under representative near-fault and far-fault earthquakes. They concluded that higher characteristic strength ratio effectively helps reducing large base displacement under near-fault earthquakes but this may have a negative impact on the superstructure responses especially under far-fault earthquakes. In their dynamic analyses considering different damping models for isolators, including interpolated damping, Rayleigh damping with override, Rayleigh damping, constant damping with override, and constant damping for all modes, Tsipianitis and Tsompanakis [14] demonstrated that the most suitable method for numerical modeling of isolator's damping for a squat cylindrical liquid storage tank isolated with single friction pendulum bearings under strong near-fault ground motions is Rayleigh damping with override. In order to enhance the dynamic performance of base-isolated cylindrical LSTs, Tsipianitis and Tsompanakis [3] used sizing optimization of the main parameters of single friction pendulum bearings and triple friction pendulum bearings via efficient swarm intelligence optimization algorithms.

It is possible to effectively benefit from base-isolation systems in protecting liquid storage tanks from *far-fault* earthquakes with high-frequency content. However, when *near-fault* earthquakes are considered, large-amplitude velocity pulses with long periods, which are generally in the range of 2 s ~ 4 s [15-19], may coincide with the isolation periods of the base-isolated LSTs, which are generally in the range of 2 s ~ 4 s, and result in very large isolation system displacements that directly threaten the tank safety [20-22]. Dynamic behavior of liquid storage tanks is represented by the combination of three main modes, namely the sloshing/convective mode, the fluid-tank mode, and the rigid impulsive mode associated with the sloshing of the fluid in the tank, the deformation of the tank wall, and the non-vibratory part of the fluid, respectively [23]. In particular, the period of the sloshing mode is typically a long one and thus may coincide with the near-fault earthquake pulse periods, resulting in very large sloshing displacements. There are various research studies in the literature about the dynamic responses of base-isolated LSTs under near-fault earthquakes. For example, Alhan et al. [22] exemplified the seismic responses of a benchmark base-isolated cylindrical LST made of steel under synthetically generated sample near-fault earthquake records of different magnitudes at different fault-distances. Kalogerakou et al. [24] examined the hydrodynamic responses of rigid cylindrical liquid storage tanks by emphasizing the near-fault phenomenon. They showed that according to the

concept presented by Housner [25] considering an impulsive and a series of convective modes, neglecting the second convective mode can have important effects in predicting the maximum shaking wave height. Öncü-Davas et al. [26] evaluated the success of synthetic earthquake records generated by using different pulse models in representing equivalent historical earthquake records in terms of the seismic responses of base-isolated steel LSTs with a circular plan. Safari and Tarinejad [27] conducted a parametric study of stochastic seismic responses of base-isolated cylindrical steel LSTs under near-fault and far-fault ground motions to evaluate the influence of characteristic parameters of the storage tanks and isolation system and excitation features. Zhao et al. [2] showed that using ADINA software is feasible to simulate the sloshing wave heights of large vertical cylindrical storage tanks made of steel under near-fault earthquakes by comparing the shaking table test results with the results from the finite element simulation. They also conducted a research on the rationality of the wave-height fortification of national storage tank specifications.

As described above, large isolation system and sloshing displacements may be observed for base-isolated LSTs located in near-fault regions. In order to tackle this near-fault earthquake challenge, supplemental viscous dampers may be employed at the base-isolation systems of LSTs located in regions close to active faults. However, there are limited studies in the literature about the seismic behavior of base-isolated LSTs equipped with supplemental viscous dampers. In a numerical example of an earlier technical report, it is demonstrated how supplemental viscous dampers can be employed at the base-isolation system of a sample cylindrical steel LST model via the 3D-BASIS-ME program [28]. The study considers a single superstructure model, with H/R and h/R ratios of 0.67 and 0.0014, respectively, and a single rubber base-isolation system consisting of low-damping rubber bearings with linear viscous fluid dampers. In an experimental study, Castellano et al. [29] presented preliminary results of the shaking table tests conducted on a cylindrical liquefied natural gas storage tank mock-up seismically protected with laminated rubber bearings and steel hysteretic torsional dampers. In a more recent conference paper, Gazi et al. [30] numerically demonstrated the potential improvement in seismic response of base-isolated steel LSTs considering a single superstructure model with a circular plan [28], only, when nonlinear supplemental viscous dampers are employed in the isolation system. And, Luo et al. [31] proposed a hybrid control system, which simultaneously adjusts mass, stiffness, and damping, consisting of a viscous mass damper used with a rubber bearing to mitigate the liquid sloshing in cylindrical storage tanks. As a predecessor of the present work, Güler and Alhan [32] evaluated the seismic responses of a single benchmark squat (H/R=0.50) tank model, only, in order to determine the performance limits of base-isolated LSTs with/without supplemental viscous damping under near-fault earthquakes using synthetically generated pulse models. Most recently, Tsipianitis and Tsompanakis [33] investigated the beneficial impact of supplemental linear viscous dampers on the seismic performance of steel LSTs with the cylindrical form equipped with single friction pendulum devices in terms of isolators' displacement capacity and superstructure accelerations under a suite consisting of twenty near-fault accelerograms. They modelled the liquid tanks utilizing the so-called "Joystick" model presented by Bakalis et al. [34] for fixed-base tanks. In order to portray a complete picture for base-isolated LSTs equipped with rubber bearings and supplemental viscous dampers, it is essential to perform a comprehensive examination considering a wide range of both *superstructure* and *isolation system* characteristic parameters (the supplemental viscous damping ratio, the isolation system period, the tank wall flexibility, and the tank slenderness ratio) under both historical

near-fault and historical *far-fault* earthquake records encompassing a wide frequency range. In this study, a parametric investigation is carried out via nonlinear seismic response analyses in order to determine the influence of the considered parameters on the base displacement, the sloshing displacement, and the isolation system shear force demands.

The assumptions and limitations of this study can be summarized as follows: simplified lumped mass model [23] is taken into account. The wave-wave, wave-wall and wave-roof interactions are neglected. Fully symmetric base-isolation systems are taken into account in order to avoid eccentricity. Unidirectional excitation is considered in the time history analysis, ignoring the effect of the vertical components of the ground motions. Finally, soil-structure interaction is not taken into account.

The outline of the content can be summarized as follows: First, the properties of the tank superstructures and the base-isolation systems consisting of isolators and supplemental viscous dampers are introduced. Then, the numerical modeling of the base-isolated LSTs with supplemental viscous dampers is described. Next, the characteristics of twelve historical earthquake records, six representing near-fault and six representing far-fault earthquakes, are presented. Then, the nonlinear time history response results are discussed in terms of both the peak and the average responses in a comparative manner as a function of the parameters including the tank flexibility, the tank slenderness ratio, the isolation system period, and the supplemental viscous damping ratio. Finally, the conclusions drawn are presented.

2. BASE-ISOLATED LST MODELS WITH SUPPLEMENTAL VISCOUS DAMPERS

Within the scope of the study conducted by Güler [35], the base-isolated LST model equipped with supplemental viscous dampers whose schematic view given in Figure 1 is used. The overall tank geometry is similar to that considered by Tsopelas et al. [28]. The tank has a cylindrical steel wall of thickness h and is covered with a concave steel roof that allows the liquid to slosh without spilling. The radius (R) of the circular tank plan is 18.29 m and the
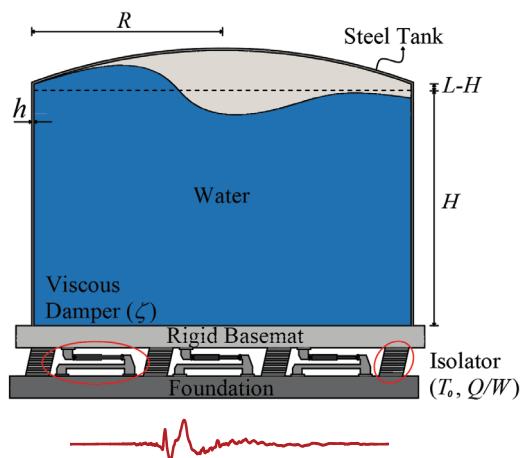
Figure 1 - Schematic view of the base-isolated LST with supplemental viscous dampers.

height of the water (H) in the tank is 0.61 m below the tank wall height (L). The tank is placed on a reinforced concrete basemat with a thickness of h_b=45.72 cm and a radius of R_b=18.59 m. In the following subsections, first, the superstructure (i.e. tank) model parameters including the ratio of the water height to the tank radius (H/R) and the ratio of the steel tank wall thickness to the tank radius (h/R) are defined. Then, isolation system model parameters (i.e. the characteristic values of the isolators and supplemental viscous dampers), including the characteristic strength of the isolation system to the total structure weight ratio (Q/W), the post-yield isolation system period (T_0), and the total supplemental viscous damping coefficient (ζ) are presented. Finally, the numerical modeling base-isolated LSTs with supplemental viscous dampers in 3D-BASIS-ME [28] software is explained. A total of 112 different models are formed by combining fourteen different superstructures with eight different base-isolation systems.

2.1. Tank Superstructure

Two main superstructure parameters that influence the seismic behavior of LSTs are (i) the ratio of water height to the tank radius (H/R) and (ii) the ratio of steel tank wall thickness to the tank radius (h/R). In this study, H/R values are chosen as 0.50, 0.75, 1.00, 1.25, 1.50, 1.75, and 2.00 in order to cover a wide practical range of slenderness ratio -from squat to slender- and h/R values are taken into account as 0.001 and 0.004, in order to consider flexible and rigid cases, respectively. The range of the selected parameters are in general compliance with those used in the literature [e.g., 27, 36-39]. Using the unit weights of 7850 kg/m^3, 1000 kg/m^3, and 2400 kg/m^3 for steel, water and concrete, respectively, the weight of water in the tank (W_w), the reinforced concrete basemat (W_{cb}), and the steel tank (W_{st}) and the total superstructure weight ($W_t=W_w+W_{cb}+W_{st}$) are calculated for each tank and reported in Table 1. The steel tank weight includes the weights of the tank wall and the roof.

Table 1 - Weights of LST models.

H/R	W_{st} [kN]		W_w [kN]	W_{cb} [kN]	W_t [kN]	
	h/R= 0.001	h/R= 0.004			h/R= 0.001	h/R= 0.004
0.50	3106.3	12425.1	94705.2	11699.8	109511.3	118830.1
0.75	3845.8	15383.2	142057.8	11699.8	157603.4	169140.8
1.00	4585.3	18341.3	189410.4	11699.8	205695.5	219451.5
1.25	5324.9	21299.5	236763.0	11699.8	253787.6	269762.2
1.50	6064.4	24257.6	284115.6	11699.8	301879.8	320073.0
1.75	6803.9	27215.7	331468.2	11699.8	349971.9	370383.7
2.00	7543.5	30173.8	378820.8	11699.8	398064.0	420694.4

2.2. Base-Isolation System - Isolators and Supplemental Viscous Dampers

The base-isolation system consists of 52 equivalent rubber-based isolators placed in a symmetrical fashion under the rigid reinforced concrete basemat and 24 equivalent supplemental viscous dampers placed in parallel with the isolators whose general layout is given in Figure 2 [28].
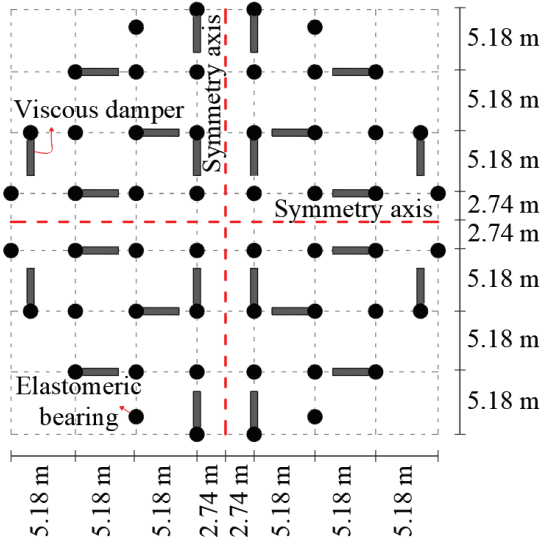
Figure 2 - Layout of the base-isolation system (modified from Tsopelas et al. [28]).

Rubber-based isolators show nonlinear hysteretic behavior. The behavior of these isolators can be represented by a smooth bilinear force (F)-displacement (D) curve [40] obtained by using an extended version of the Bouc-Wen [41, 42] hysteretic model presented by Park et al. [43] for biaxial interactions. In this regard, forces developed in the rubber-based isolators along orthogonal x and y directions are obtained by the following equations depending on the yield strength (F_y), the yield displacement (D_y), and the post-yield to pre-yield stiffness ratio (α):

$$F_x = \alpha \frac{F_y}{D_y} U_x + (1-\alpha) F_y Z_x \tag{1}$$

$$F_y = \alpha \frac{F_y}{D_y} U_y + (1-\alpha) F_y Z_y \tag{2}$$

Here, while U_x and U_y are the displacements of the rubber-based isolators in two orthogonal directions, Z_x and Z_y are the dimensionless hysteretic variables given by the following Equation [43]:

$$\begin{Bmatrix} \dot{Z}_x D_y \\ \dot{Z}_y D_y \end{Bmatrix} = \begin{Bmatrix} A\dot{U}_x \\ A\dot{U}_y \end{Bmatrix} - \begin{bmatrix} Z_x^2(\gamma \mathrm{Sign}(\dot{U}_x Z_x) + \beta) & Z_x Z_y(\gamma \mathrm{Sign}(\dot{U}_y Z_y) + \beta) \\ Z_x Z_y(\gamma \mathrm{Sign}(\dot{U}_x Z_x) + \beta) & Z_y^2(\gamma \mathrm{Sign}(\dot{U}_y Z_y) + \beta) \end{bmatrix} \begin{Bmatrix} \dot{U}_x \\ \dot{U}_y \end{Bmatrix} \tag{3}$$

where $\dot{U}_x$ and $\dot{U}_y$ are the velocities of the rubber-based isolators in two orthogonal directions, and Sign is the signum function. On the other hand, A, γ, and β are dimensionless quantities that control the shape of the hysteresis loop. And they are accepted as 1.0, 0.9, and 0.1 to represent the smooth bilinear force-displacement loop, respectively [28]. A graphical representation of the smooth bilinear force-displacement curve is given in Figure 3.
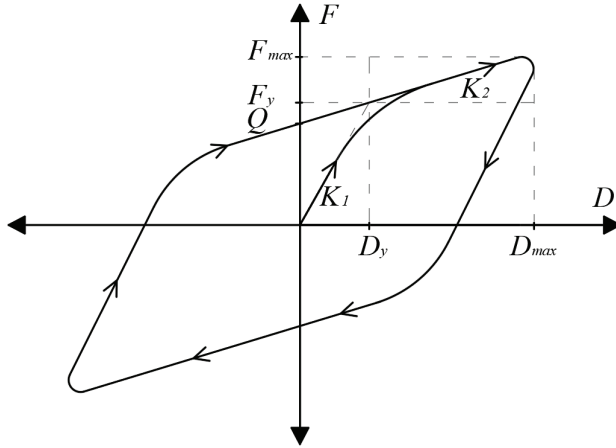
Figure 3 - Smooth bilinear force-displacement curve [44].

In this context, the basic mechanical parameters of the isolation system, which determine the seismically isolated behavior of the structure and used in 3D-BASIS-ME [28] can be listed as the pre-yield stiffness (K_1), the post-yield stiffness (K_2), the characteristic force (Q), the yield strength (F_y), and the yield displacement (D_y). For a total weight of W supported by the isolators, the post-yield isolation period (also known as rigid-body period) is presented as follows [40]:

$$T_0 = 2\pi / \sqrt{K_2(\mathrm{g}/W)} \tag{4}$$

The relationship between other parameters and the ratio of post-yield stiffness to pre-yield stiffness α is defined as follows [44]:

$$Q = (K_1 - K_2) \times D_y \tag{5}$$

$$K_1 = F_y / D_y \tag{6}$$

$$\alpha = K_2 / K_1 \tag{7}$$

In this study, two main sets of isolation systems with $T_0=2$ and 4 s that correspond to short and long-period isolation systems, respectively, are considered. The characteristic values for the isolation systems of each base-isolated LST model are obtained by using the relations presented in Equations (4), (5), (6), and (7) and given in Table 2. In calculating the isolation periods and the characteristic force ratios, the effective weight (W) values obtained by subtracting the flexible sloshing mode weight (W_s) from the total weight on the isolation system (W_t) are used, as suggested by Tsopelas et al. [28]. The characteristic strength ratio (Q/W) is assumed as 5% and the yield displacement (D_y) is accepted as 1.5 cm.

Table 2 - Characteristic values of the isolation systems.

H/R	W [kN× 10^{-3}]	Q [kN× 10^{-3}]	T_0=2 s, α=0.23			T_0=4 s, α=0.07		
			K_2 [kN/m× 10^{-3}]	K_1 [kN/m× 10^{-3}]	F_y [kN× 10^{-3}]	K_2 [kN/m× 10^{-3}]	K_1 [kN/m× 10^{-3}]	F_y [kN× 10^{-3}]
			h/R=0.001					
0.50	47.0	2.3	47.3	203.9	3.1	11.8	168.5	2.5
0.75	81.7	4.1	82.2	354.7	5.3	20.6	293.1	4.4
1.00	123.8	6.2	124.5	537.4	8.1	31.1	444.0	6.7
1.25	169.3	8.5	170.4	735.3	11.0	42.6	607.5	9.1
1.50	216.4	10.8	217.8	939.7	14.1	54.4	776.4	11.6
1.75	264.1	13.2	265.8	1146.8	17.2	66.4	947.5	14.2
2.00	312.0	15.6	314.0	1354.9	20.3	78.5	1119.4	16.8
			h/R=0.004					
0.50	56.3	2.8	56.6	244.4	3.7	14.2	201.9	3.0
0.75	93.2	4.7	93.8	404.8	6.1	23.5	334.5	5.0
1.00	137.5	6.9	138.4	597.2	8.9	34.6	493.4	7.4
1.25	185.3	9.3	186.5	804.7	12.1	46.6	664.9	10.0
1.50	234.6	11.7	236.1	1018.7	15.3	59.0	841.7	12.6
1.75	284.5	14.2	286.3	1235.4	18.5	71.6	1020.7	15.3
2.00	334.6	16.7	336.8	1453.2	21.8	84.2	1200.6	18.0

As part of the isolation systems defined above, supplemental linear viscous dampers providing a total supplemental viscous damping of

$$C = 2 \times \zeta \times M \times \omega_0 \tag{8}$$

are employed, where ζ is the supplemental damping ratio based on the post-yield angular frequency ($\omega_0=2\pi/T_0$) of the isolation system. The effective mass (M) is obtained by dividing the effective weight (W) by the gravitational acceleration. The total supplemental viscous damping coefficients (C) obtained for each base-isolated LST and $\zeta=10\%$, 20% and 30% are given in Table 3.

Table 3 - Total supplemental viscous damping coefficients.

H/R	M [kNs²/m]	C [kNs/m] for h/R=0.001					
		$T_0=2$ s, $\omega_0=3.14$ rad/s			$T_0=4$ s, $\omega_0=1.57$ rad/s		
		$\zeta=10\%$	$\zeta=20\%$	$\zeta=30\%$	$\zeta=10\%$	$\zeta=20\%$	$\zeta=30\%$
0.50	4787.8	3008.3	6016.5	9024.8	1504.1	3008.3	4512.4
0.75	8329.2	5233.4	10466.8	15700.2	2616.7	5233.4	7850.1
1.00	12619.4	7929.0	15858.0	23787.1	3964.5	7929.0	11893.5
1.25	17266.0	10848.5	21697.0	32545.6	5424.3	10848.5	16272.8
1.50	22065.2	13864.0	27728.0	41591.9	6932.0	13864.0	20796.0
1.75	26927.1	16918.8	33837.6	50756.4	5459.4	16918.8	25378.2
2.00	31814.3	19989.5	39979.0	59968.6	9994.8	19989.5	29984.3
		C [kNs/m] for h/R=0.004					
0.50	5738.0	3605.3	7210.6	10816.0	1802.7	3605.3	5408.0
0.75	9505.7	5972.6	11945.2	17917.8	2986.3	5972.6	8958.9
1.00	14022.2	8810.4	17620.8	26431.1	4405.2	8810.4	13215.6
1.25	18894.9	11872.0	23744.1	35616.1	5936.0	11872.0	17808.0
1.50	23920.4	15029.6	30059.3	45088.9	7514.8	15029.6	22544.4
1.75	29008.5	18226.6	36453.2	54679.8	9113.3	18226.6	27339.9
2.00	34122.0	21439.5	42878.9	64318.4	10719.7	21439.5	32159.2

2.3. Numerical Modeling

Mathematical models of liquid storage tanks in this study are based on the mechanical model proposed by Haroun and Housner [23], which takes into account the deformation of the tank wall and the sloshing of the liquid inside the tank. This type of modeling concept is illustrated in Figure 4 where the effective masses of m_s, m_f, and m_r are associated with the modes related to the sloshing motion of the fluid, the deformation of the steel wall (fluid-tank interaction) and the non-vibratory part of the liquid that behaves as a rigid body, and moves with respect to the ground above the isolation system, respectively and H_s, H_f and H_r are the effective heights corresponding to the aforementioned masses.

The effective masses, the effective heights and the dominant frequencies of sloshing (ω_s) and fluid-tank (ω_f) modes for tanks filled with water are presented by Haroun and Housner [23]

as a function of *H/R* and *h/R*. The readers are referred to Haroun and Housner [23] for the relevant formulations and charts. For the establishment of the mathematical model in this study, the necessary parameters related to the sloshing/convective mode, the fluid-tank mode, and the rigid impulsive mode are given in Tables 4, 5, and 6. In these tables, the sloshing mode period (T_s) and the sloshing mode stiffness (K_s) used in 3D-BASIS-ME modeling are obtained by $T_s=2\times\pi/\omega_s$ and $K_s=\omega_s{}^2\times m_s$, respectively. Similarly, the fluid-tank mode period (T_f) and the fluid-tank mode stiffness (K_f) values are obtained by $T_f=2\times\pi/\omega_f$ and $K_f=\omega_f{}^2\times m_f$, respectively. The critical damping ratios of the sloshing and the fluid-tank modes are taken as ζ_s=0.5% [45, 46] and ζ_f=2.0%, respectively. The part of the liquid that moves rigidly and is synchronized with the ground motion without sloshing (i.e. rigid impulsive mode) is modeled to move along with the reinforced concrete basemat. By subtracting the sloshing mode, fluid-tank mode and rigid reinforced concrete basemat weights from the total weight, the weight of the rigidly acting liquid (i.e., rigid impulsive mode weight) is obtained as $W_r = W_t - W_s - W_f - W_{cb}$ and rigid impulsive mode mass is calculated as $m_r = W_r/g$.
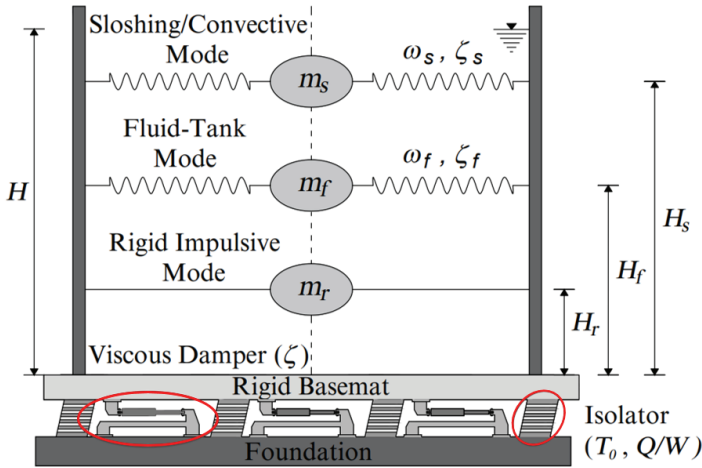
Figure 4 - Mechanical model of base-isolated LSTs.

Table 4 - Characteristic values of the sloshing mode (ζ_s=0.005).

H/R	ω_s [rad/s]	T_s [s]	m_s [kNs²/m]	K_s [kN/m]	H_s [m]
0.50	0.85	7.42	6379.3	4569.0	4.87
0.75	0.93	6.74	7741.9	6729.3	7.77
1.00	0.97	6.49	8355.7	7838.6	11.07
1.25	0.98	6.39	8613.2	8329.2	14.73
1.50	0.99	6.35	8718.0	8533.1	18.68
1.75	0.99	6.34	8760.1	8615.8	22.83
2.00	0.99	6.33	8776.9	8648.9	27.13

Table 5 - Characteristic values of the fluid-tank mode (ζ_f=0.02).

H/R	h/R=0.001				h/R=0.004			
	ω_f [rad/s]	T_f [s]	K_f [kN/m×10⁻³]	H_f [m]	ω_f [rad/s]	T_f [s]	K_f [kN/m×10⁻³]	H_f [m]
0.50	39.99	0.16	4725.6	3.59	79.98	0.08	20631.8	3.81
0.75	30.30	0.21	5973.2	5.54	60.04	0.10	25276.3	5.78
1.00	24.44	0.26	6427.3	7.68	47.81	0.13	26179.4	7.97
1.25	20.24	0.31	6179.9	10.03	39.54	0.16	24991.8	10.35
1.50	17.05	0.37	5628.4	12.55	33.15	0.19	22416.1	12.91
1.75	14.53	0.43	4939.7	15.22	28.22	0.22	19573.6	15.60
2.00	12.52	0.50	4261.2	18.01	24.23	0.26	16761.6	18.42

3D-BASIS-ME [28] software enables modeling base-isolated LSTs as a mechanical analog with its feature of defining multiple superstructures on a common basemat. Accordingly, single degree of freedom (SDOF) systems representing the fluid sloshing mode, the fluid-tank mode, and the rigid part of the liquid are located on a common basemat supported by an isolation system consisting of isolators and viscous dampers, as schematically shown in Figure 5. The base-isolated LSTs in this study are modeled in 3D-BASIS-ME with this approach and nonlinear seismic response analyses are conducted under historical earthquake records that are described in Section 3. It should be noted here that Scheller and Constantinou [47] showed that there is an excellent agreement between the time history results obtained from 3D-BASIS-ME and SAP2000 programs by making use of the base-isolated LST model presented by Tsopelas et al. [28] which has a similar geometry with the base-isolated tank models used in this study.

Table 6 - Masses.

H/R	m_s [kNs²/m]	h/R=0.001		h/R=0.004		m_{cb} [kNs²/m]
		m_f [kNs²/m]	m_r [kNs²/m]	m_f [kNs²/m]	m_r [kNs²/m]	
0.50	6379.3	2955.1	639.6	3225.5	1319.5	1192.6
0.75	7741.9	6504.2	632.0	7011.2	1301.5	1192.6
1.00	8355.7	10758.2	668.2	11453.5	1375.6	1192.6
1.25	8613.2	15089.4	983.5	15982.7	1719.1	1192.6
1.50	8718.0	19353.1	1519.0	20396.1	2331.3	1192.6
1.75	8760.1	23389.8	2344.2	24572.9	3242.6	1192.6
2.00	8776.9	27194.8	3426.5	28546.8	4382.1	1192.6

The details of the time integration algorithm used in the nonlinear time history analyses can be found in the 3D-BASIS-ME Technical Report [28]. In summary, the pseudo-force method

originally adopted in 3D-BASIS by Nagarajaiah et al. [40] is used. In this context, while obtaining the solution of the equations of motion and the solution of the differential equations governing the nonlinear behavior of the isolation elements, for each iteration, first, unconditionally stable Newmark's constant-average-acceleration method [48] then an unconditionally stable semi-implicit Runge-Kutta method suitable for stiff differential equations [49] are employed. In order to give an idea on the run time, it should be noted that the analysis for one tank model under TCU101-W ground motion with an Intel Core i7-7700HQ CPU @ 2.80GHz - 2.81 GHz, RAM 16.0 GB Processor is completed in 5.4 s.
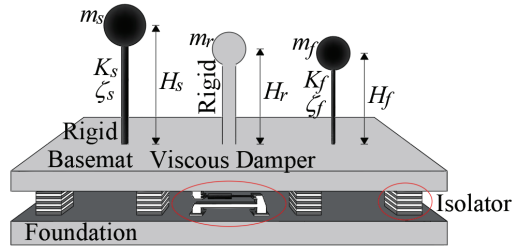

Figure 5 - Schematic representation of base-isolated LST models consisting of SDOF systems sharing a common basemat located on an isolation system equipped with supplemental viscous dampers.

3. EARTHQUAKE DATA

Near-fault earthquakes are pulse-like ground motions observed at locations close to a fault line. They have critical importance in the design of the seismically isolated structures since they may lead to serious seismic demands, particularly in terms of isolator displacements. These earthquake records differ from far-fault ones recorded further away from the seismic source by distinct pulses with high-amplitude and long-periods observed in the velocity time histories [17-19]. Although the aforementioned characteristic features of near-fault earthquakes were first revealed by Housner and Trifunac [15] while examining the records of the 1966 Parkfield earthquake at Cholame [50, 51], it was first addressed by Bertero et al. [52] that the flexible structures are vulnerable to severe effects of near-fault earthquakes. They associated the damage of the buildings of the Olive View Medical Center during the 1971 San Fernando California earthquake with near-fault earthquake effects [53]. However, this potential problem has attracted most engineers' attention, only after the 1994 Northridge, California Earthquake that occurred in a heavily urbanized area [54]. In this context, Hall et al. [55] and Heaton et al. [56] emphasized that the necessity of developing appropriate design codes to prevent the potential destructive effects of near-fault earthquakes by examining the seismic performance of flexible high-rise and seismically isolated buildings under the effect of a simulated M_w 7.00 earthquake on a blind thrust fault.

Until today, various studies have been carried out examining seismically isolated structures from different perspectives under near-fault earthquakes. Among these, base-isolated LSTs are of particular importance because both the period of the isolation system and the sloshing mode period of such structures may coincide with the velocity pulse periods of the near-fault earthquakes, resulting in very large isolation system and sloshing displacements. As

explained in Introduction section, supplemental viscous dampers may be employed at the base-isolation systems of LSTs in order to prevent large base displacements (i.e. isolation system displacements) that may occur under near-fault earthquakes but this may cause increases in the seismic demands of the superstructure in case of far-fault earthquakes. In order to examine both situations, in this study, twelve historical earthquake records, six representing near-fault and six representing far-fault earthquakes, are obtained from University of California, Berkeley PEER Ground Motion Database [57] for use in the nonlinear time history analyses. Information on these records is presented in Table 7 where M_w, r, PGA, PGV, T_p, VSI, and HI represent the moment magnitude, the fault-distance, the peak ground acceleration, the peak ground velocity, the predominant period (for far-fault earthquakes)/the pulse period (for near-fault earthquakes), the Velocity Spectrum Intensity, and the Housner Intensity, respectively. As it can be seen from Table 7, for the near-fault earthquake records, the closest distances to the fault lines are less than 10 km and PGV values vary from 40.6 cm/s to 166.1 cm/s. On the other hand, for the far-fault records, the fault-distances are more than 10 km (from 10.30 to 19.30 km) and PGV values are much less than those of near-fault ones and vary from 19.7 to 44.6 cm/s.

Table 7 - Characteristics of historical near-fault and far-fault earthquake records.

| Earthquake	M_w	Component	Station Name	r [km]	PGA [g]	PGV [cm/s]	T_p [s]	VSI [cm]	HI [cm]
Near-fault									
Chi-Chi	7.6	TCU052-W	TCU052	0.24	0.348	159.0	2.48	318.3	382.5
Erzincan	6.9	ERZ-NS	Erzincan	2.00	0.515	83.9	2.40	297.0	319.9
Chi-Chi	7.6	TCU101-W	TCU101	2.94	0.202	67.9	3.98	114.7	119.2
Loma Prieta	6.9	LGP000	LGPC	6.10	0.563	94.8	3.22	431.4	409.8
Northridge	6.7	RRS228	Rinaldi Receiving Sta.	7.10	0.838	166.1	1.42	509.7	456.8
Northridge	6.7	ARL090	Arleta-Nordhoff Fire Sta.	9.20	0.344	40.6	1.06	146.2	130.1
Far-fault									
Loma Prieta	6.9	BRN-090	BRAN	10.30	0.501	44.6	0.14	165.1	120.8
Northridge	6.7	RO3-090	Sun Valley-Roscoe Blvd.	12.30	0.443	38.2	0.16	173.7	165.7
Loma Prieta	6.9	CAP000	Capitola	14.50	0.529	36.5	0.28	207.4	187.0
Chi-Chi	7.6	CHY029-W	CHY029	15.28	0.277	30.3	0.46	125.4	116.7
Loma Prieta	6.9	WAH-090	WAHO	16.90	0.638	38.0	0.14	147.9	127.9
Northridge	6.7	SSU-090	Santa Susana Ground	19.30	0.290	19.7	0.33	89.2	78.2
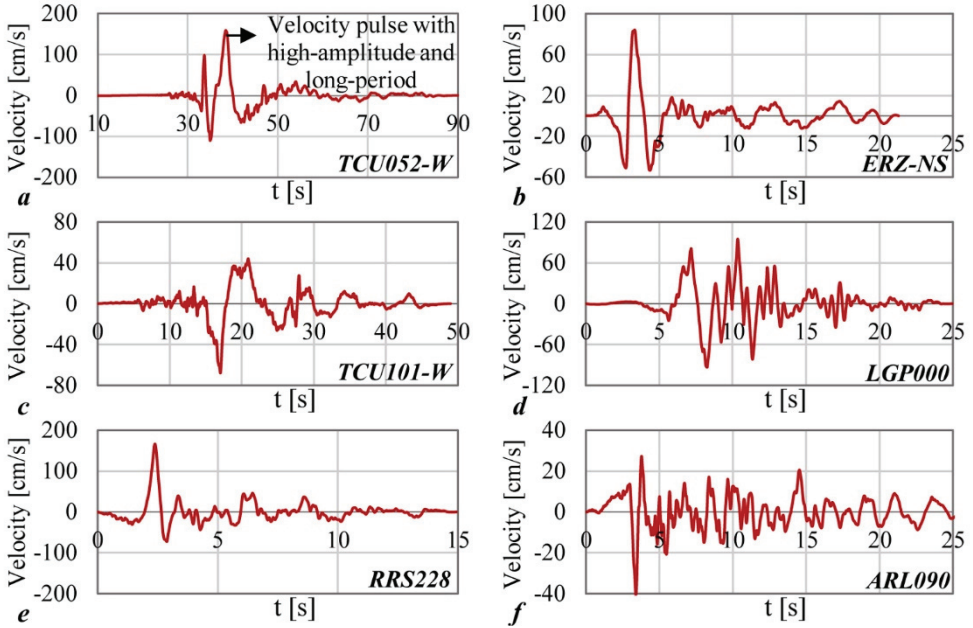
Figure 6 - Velocity time histories of near-fault earthquake records - (a) TCU052-W, (b) ERZ-NS, (c) TCU101-W, (d) LGP000, (e) RRS228, and (f) ARL090.
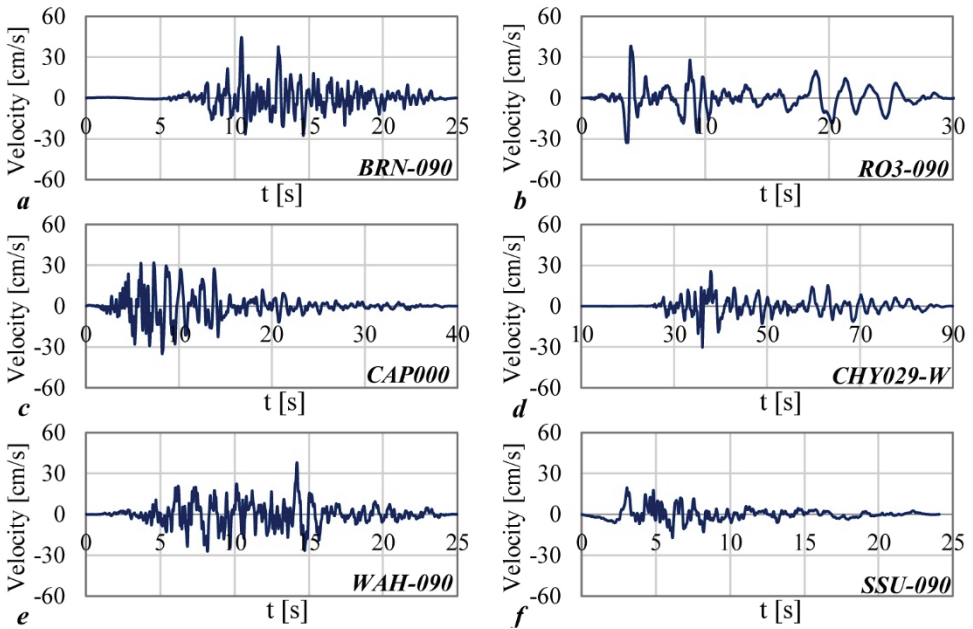

Figure 7 - Velocity time histories of far-fault earthquake records - (a) BRN-090, (b) RO3-090, (c) CAP000, (d) CHY029-W, (e) WAH-090, and (f) SSU-090.

Figures 6 and 7 present the velocity time histories of near-fault and far-fault earthquake records, respectively. Similar to what was pointed out in the previous studies [18, 26, 58], it is seen from Figure 6 that the near-fault earthquake records contain large-amplitude and long-period velocity pulses ranging from 1.06 s to 3.98 s as presented in Table 7, which would amplify the responses of base-isolated LSTs. On the other hand, far-fault earthquake records do not contain any velocity pulses (Figure 7). Also, the Housner Intensity and Velocity Spectrum Intensities for the near-fault earthquake records are much larger (ranging from 130.1 cm to 509.7 cm) compared to those for far-fault earthquake records (ranging from 78.2 cm to 207.4 cm). This also is an indicator of the much larger seismic demands near-fault earthquake records would have on the base-isolated LSTs considered in this study.

4. DISCUSSION OF RESULTS

Base-isolated LSTs obtained by combining different parameters including the properties of the tank geometry (H/R and h/R) and the properties of the base-isolation system (T_0 and ζ) as described in detail in Section 2 are modeled numerically in 3D-BASIS-ME and subjected to six near-fault (TCU052-W, ERZ-NS, TCU101-W, LGP000, RRS228, and ARL090) and six far-fault (BRN-090, RO3-090, CAP000, CHY029-W, WAH-090, and SSU-090) historical earthquake records whose characteristic features are described in detail in Section 3. As a result of the nonlinear time history analyses, structural responses including the base displacement, the sloshing displacement, and the isolation system shear force are obtained and reported here. Normalized isolation system shear forces are obtained by proportioning the isolation system shear forces to the total weight of the superstructure on the isolation system.

4.1. Response Time Histories

Although the assessments here are made using the peak values, in order to also portray the time history behavior visually, first, the time variation of aforementioned structural responses are presented in Figure 8 for a sample base-isolated LST model with T_0=4 s, ζ=20%, H/R=1.25 and for TCU052-W and CAP000, only, as representatives of near-fault and far-fault earthquakes, respectively. This figure shows that the TCU052-W near-fault earthquake leads to significantly higher responses in comparison with the CAP000 far-fault earthquake. It is also observed that while the far-fault earthquake responses in terms of base displacement and isolation system shear force contain high-frequency parts, counterpart near-fault responses show pulse-like nature. Differently, the sloshing displacement responses both in case of far-fault and near-fault earthquakes have long-periods and the sloshing continues even after the earthquake comes to an end due to the very low sloshing mode damping.

4.2. Peak Responses

The complete picture of the study in terms of peak responses are presented in Figures 9-11. The peak base displacement, the peak sloshing displacement, and the normalized peak isolation system shear force demands for all considered cases and parameters are shown in Figures 9, 10, and 11, respectively. It should be noted here that these and other remaining
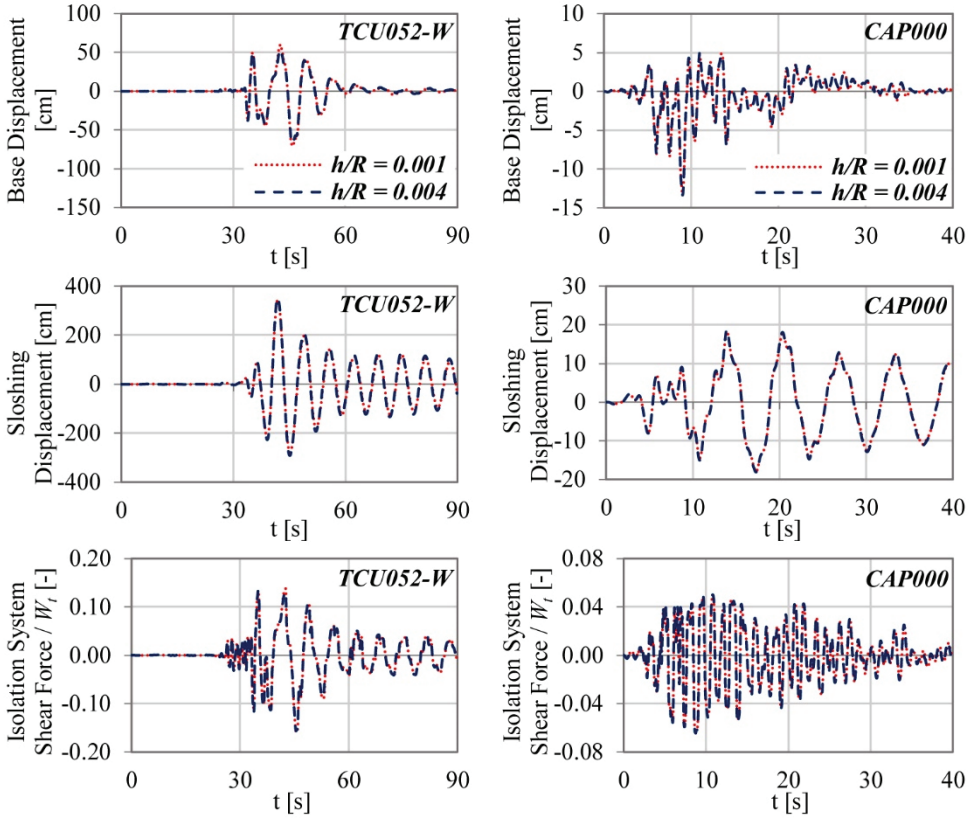
Figure 8 - Time histories of the structural responses for base-isolated LSTs with T_0=4 s, ζ=20%, H/R=1.25 under near-fault TCU052-W and far-fault CAP000 earthquakes.

figures in this paper are presented for h/R=0.001, only, since the influence of this parameter which is related to tank thickness/flexibility are rather limited as demonstrated in Figure 8 that compares the time histories of the structural responses for h/R=0.001 and h/R=0.004. A more detailed discussion regarding this issue is presented in Section 4.3.1.

As seen in Figures 9-11, the structural responses vary in a wide range depending on the characteristic of the earthquake record (i.e. moment magnitude (M_w), the fault-distance (r), near-fault vs. far-fault), the slenderness of the tank (i.e. H/R ratio), the isolation period (T_0), and the level of viscous supplemental damping (ζ).

As a common observation, the structural responses obtained in case of near-fault earthquakes are significantly higher than those obtained for far-fault earthquakes. While the peak base displacement can be as high as 132.54 cm in case of near-fault earthquakes (for TCU052-W, H/R=0.50, T_0=4 s), the highest value is only 17.10 cm in case of far-fault earthquakes (for CAP000 earthquake and T_0=2 s). Therefore, it is seen that supplemental damping may be required when LSTs with long-period isolation systems are subjected to large magnitude near-fault earthquakes.

Figure 9 - Peak base displacement (PBD) demands for near-fault and far-fault earthquakes. (Values in parenthesis are the moment magnitude, M_w, and the fault-distance, r).
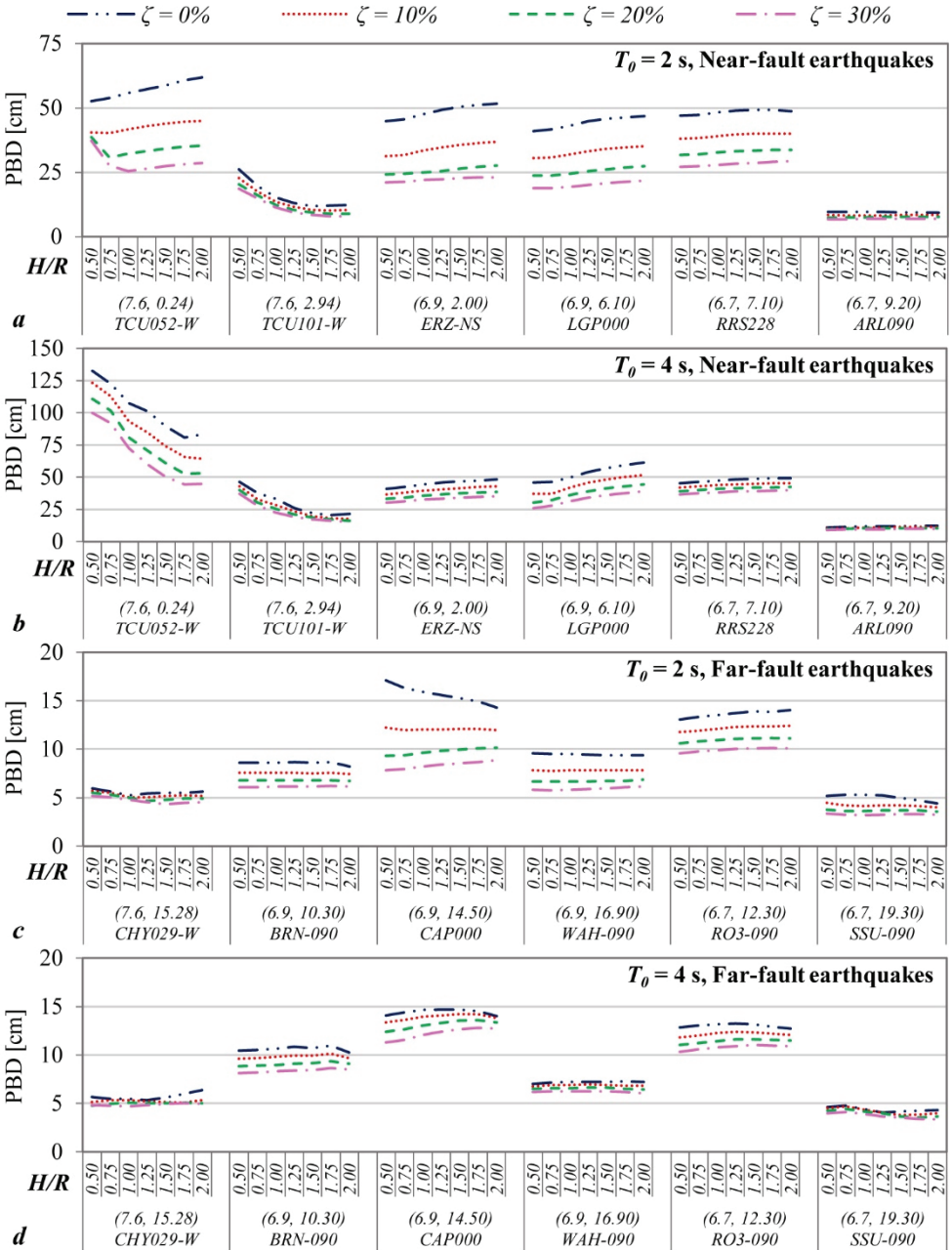
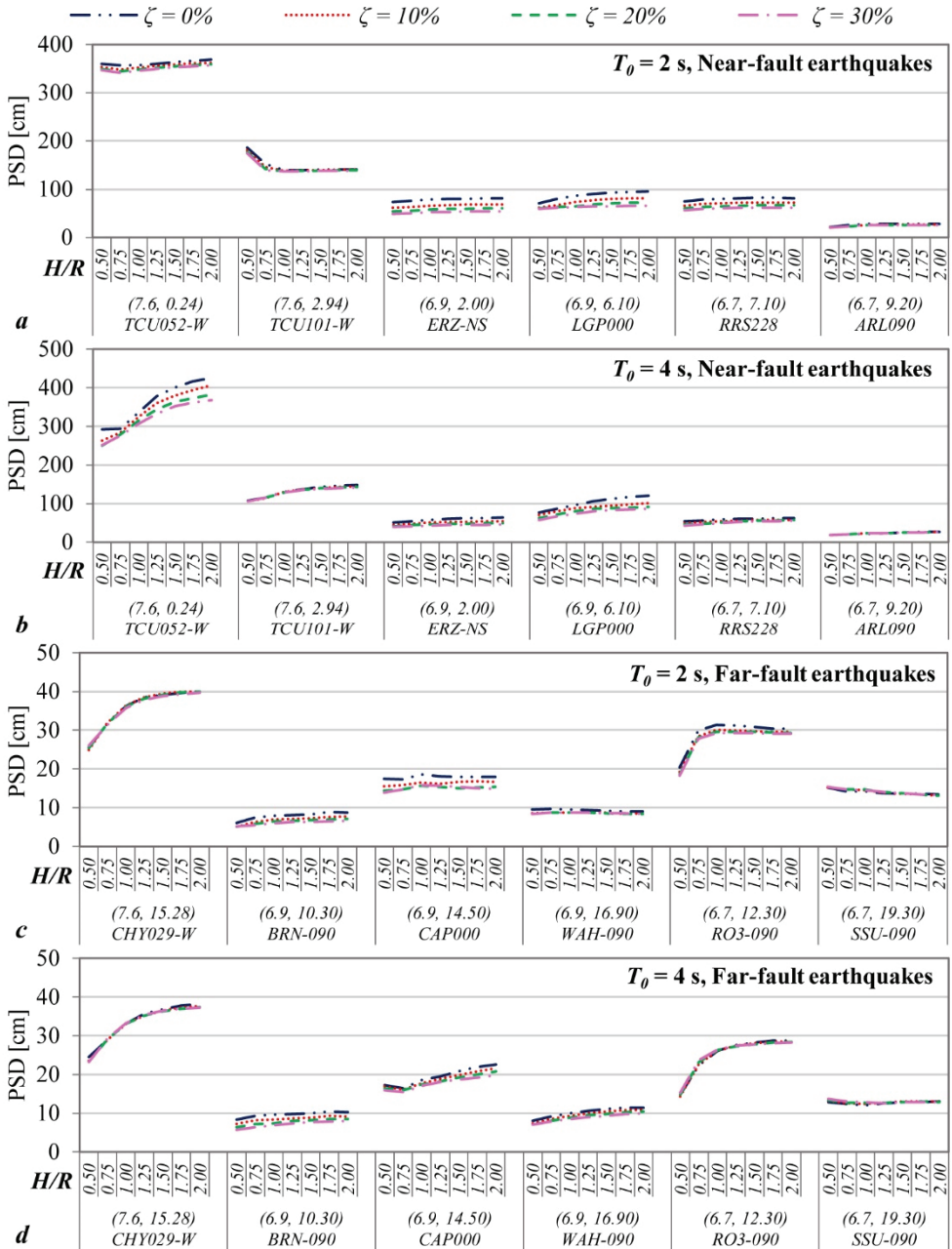*Figure 10 - Peak sloshing displacement (PSD) demands for near-fault and far-fault earthquakes. (Values in parenthesis are the moment magnitude, M_w, and the fault-distance, r).*
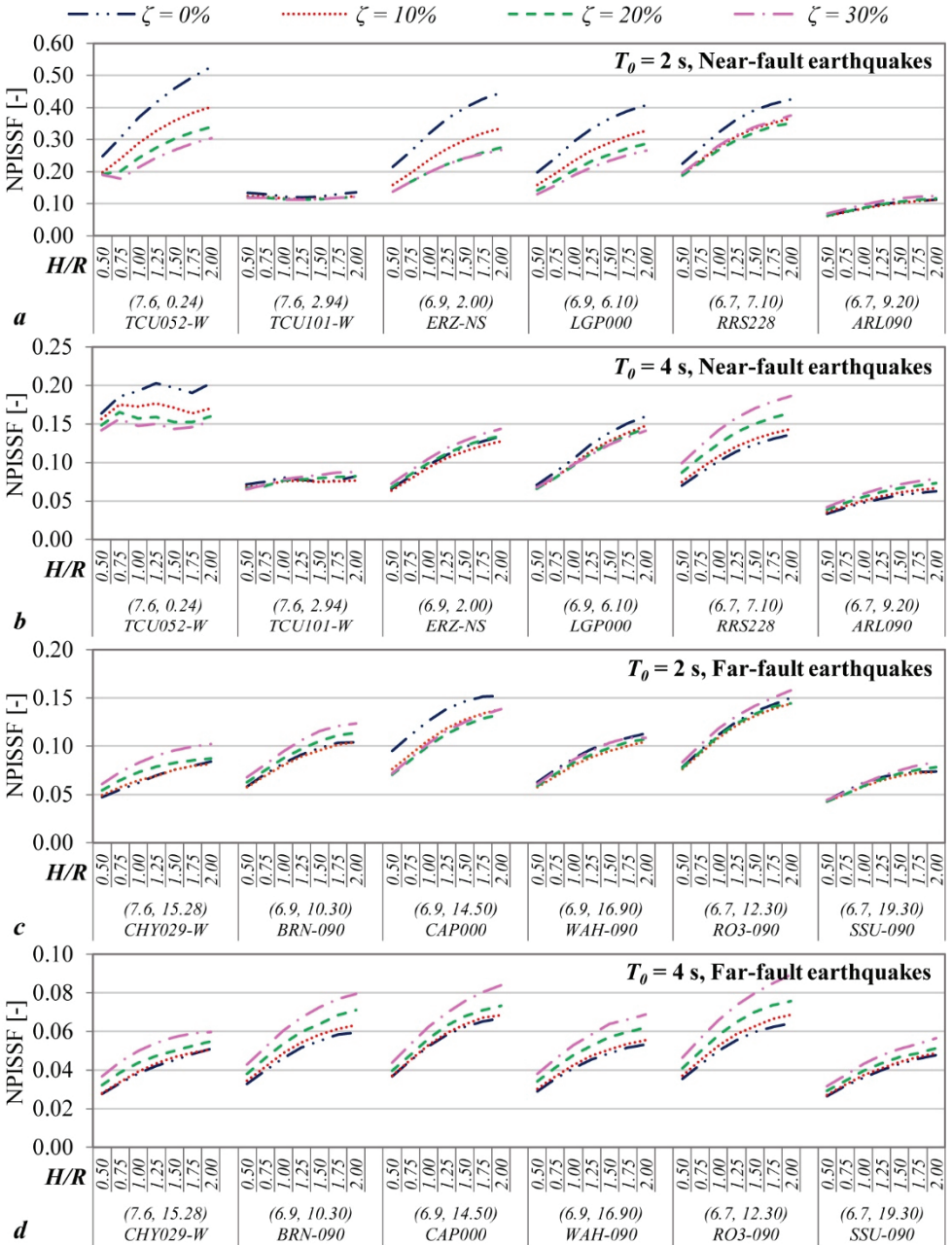
Figure 11 - Normalized peak isolation system shear force (NPISSF) demands for near-fault and far-fault earthquakes. (Values in parenthesis are the moment magnitude, M_w, and the fault-distance, r).

Likewise, the sloshing displacement demands may be extremely high in near-fault earthquakes, with the largest being 425.20 cm observed for TCU052-W, *H/R*=2.00, and T_0=4 s. On the other hand, the largest peak sloshing displacement demand in case of far-fault earthquakes was only 40.0 cm which is obtained for CHY029-W. The peak isolation system shear force values also yield a similar trend. While the largest demand in terms of this structural response is 0.16 in case of far-fault earthquakes (for RO3-090, *H/R*=2.00, T_0=2 s), it is about 3.3 times larger, i.e. 0.53, in case of near-fault earthquakes (for TCU052-W, *H/R*=2.00, T_0=2 s).

Another observation is that while the demands quickly decrease as the fault-distance increases in case of near-fault earthquakes, such a clear trend is not observed in case of far-fault earthquakes. In particular, TCU052-W, which is recorded at only 0.24 km away from the fault line, dissociates from other earthquake records which results in very high demands especially for long-period isolation systems and in terms of base displacement and sloshing displacement. The supplemental viscous damping proved to be very successful in this case by reducing the peak base displacement demands from 83.03 ~ 132.54 cm range realized for ζ=0% to 44.17 ~ 99.90 cm range realized for ζ=30% (depending on *H/R*). Furthermore, even the peak sloshing displacement demands, which may be classified as part of the superstructure response, are suppressed from 292.35 ~ 425.20 cm realized for ζ=0% to 251.94 ~ 367.79 cm range realized for ζ=30%.

4.3. Average Peak Responses and General Trends

In order to bring out the general trends as a function of the parameters examined herein, the average values of the peak base displacement, the peak sloshing displacement, and the normalized isolation system shear force demands are presented in Figures 12, 13, and 14, respectively, in a comparative fashion both for near-fault and far-fault earthquakes. The influences of the tank flexibility, *h/R*, the tank slenderness ratio, *H/R*, the isolation system period, T_0, and the supplemental viscous damping ratio, ζ, on the behavior of base-isolated LSTs equipped with supplemental viscous dampers under near-fault and far-fault earthquakes are discussed by making use of these plots in Sections 4.3.1-4.3.4.

4.3.1. Influence of the Tank Flexibility, h/R

Figure 8 compares the time histories of the structural responses for tank flexibility ratios of *h/R*=0.001 and *h/R*=0.004 for the sample base-isolated LST model with T_0=4 s, ζ=20%, *H/R*=1.25 under TCU052-W and CAP000 which are meant to represent near-fault and far-fault earthquakes, respectively. It is observed that the influence of tank flexibility, i.e. the influence of tank-fluid interaction, on both the superstructure and the isolation system responses are much less than the other parameters (i.e., *H/R*, T_0, and ζ) and negligibly small. This finding is in line with other studies on base-isolated LSTs without supplemental dampers [e.g., 59-61]. Besides, Safari and Tarinejad [27] reported that the effect of the tank flexibility on the sloshing displacement, the isolator displacement, and the base shear demands generally can be neglected.
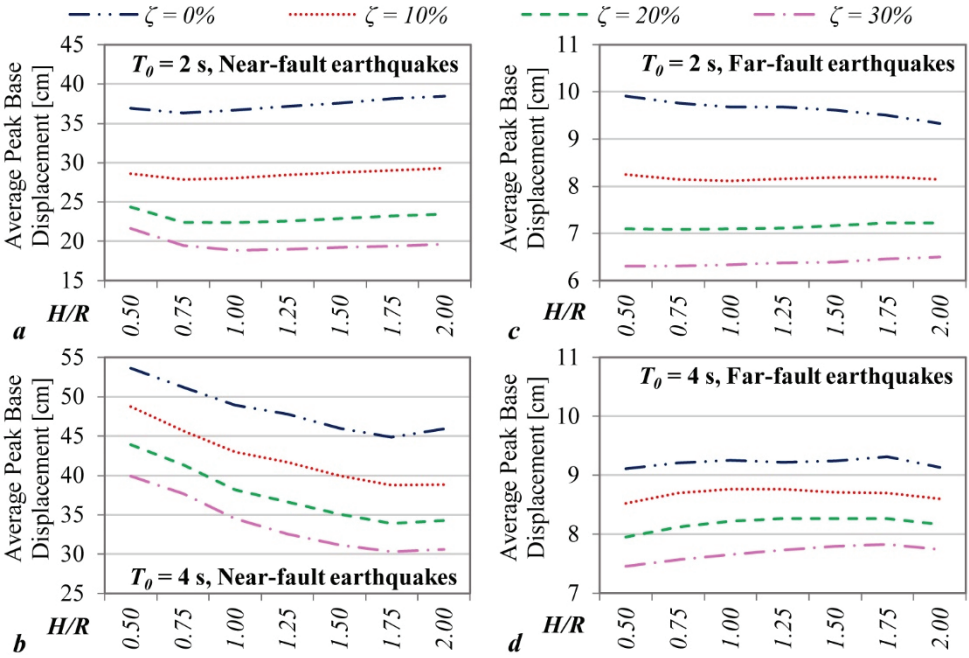
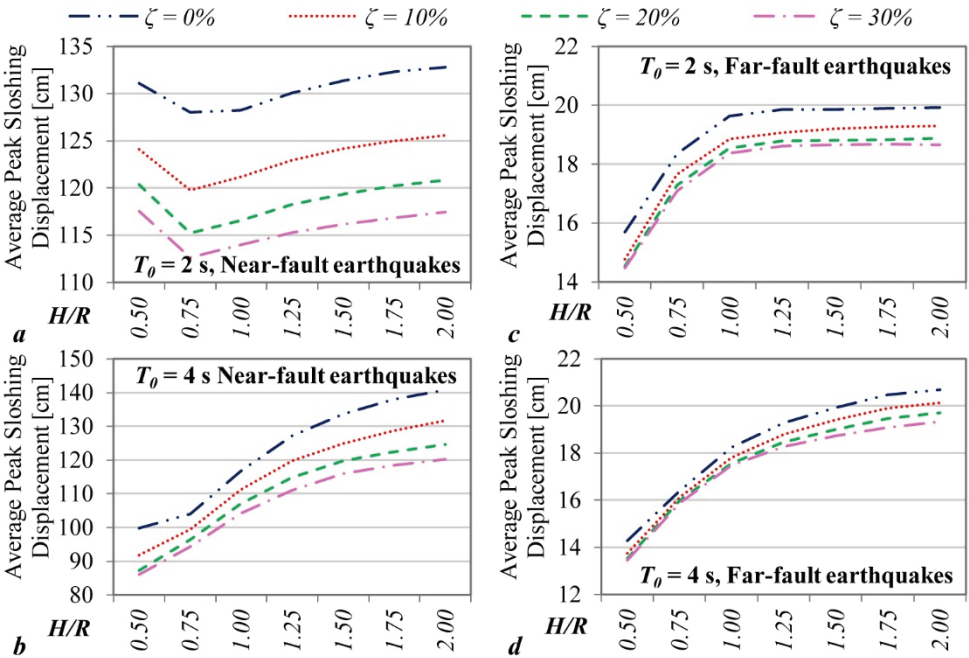Figure 12 - Average peak base displacement demands.

Figure 13 - Average peak sloshing displacement demands.
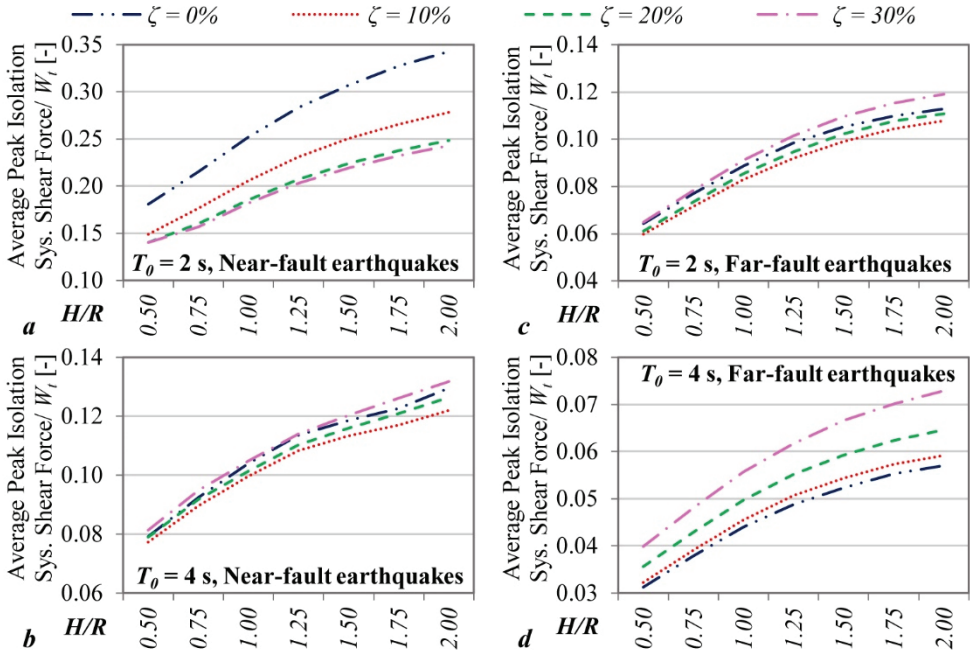
Figure 14 - Average normalized peak isolation system shear force demands.

4.3.2. Influence of the Tank Slenderness Ratio, H/R

It is observed that the increase in the tank slenderness ratio, *H/R*, could increase or decrease the peak base displacement demands depending on the characteristics of the earthquake (see Figure 12). Although there is no clear trend, it is important to observe that the tank slenderness ratio may have considerable effects on the peak base displacement demands particularly in case of LSTs with long-period isolation systems. As it can be seen from Figure 12, in case of long-period T_0=4 s isolation systems under near-fault earthquakes, the change in the average peak base displacement demands is about 20% as *H/R* varies from 0.50 to 2.00.

When Figure 13 is examined, the increase in the tank slenderness ratio, *H/R*, generally increases the peak sloshing displacement demands for both near-fault and far-fault earthquakes. While the extent of this increase varies depending on the characteristics of the individual earthquake record, the effect is more significant in case of long-period T_0=4 s isolation systems and the change in the average peak sloshing displacement demands is about 40% as *H/R* varies from 0.50 to 2.00.

Normalized peak isolation system shear forces increase both under the near-fault and the far-fault earthquakes with the increase in the tank slenderness ratio, *H/R*. As seen in Figure 14, the increase observed in the average normalized peak isolation system shear force responses is significant and varies in the range of about 60 to 90% as *H/R* varies from 0.50 to 2.00.

4.3.3. Influence of the Isolation System Period, T_0

As shown in Figure 12, the peak base displacement demands for the short-period base-isolated LSTs with T_0=2 s are smaller than long-period ones with T_0=4 s for both near-fault and far-fault earthquakes. This is much more pronounced in case of near-fault earthquakes where the peak base displacement demands of long-period isolation systems may be higher than that of the short-period isolation system as much as 84.48% as observed for H/R=0.50, ζ=30% case. Under the far-fault earthquakes, although the increase in the isolation system period results in a higher peak base displacement demand, it is not as dramatic as is the case for near-fault earthquakes. The largest increase in this case is about 22%. Furthermore, although exceptional, there may be cases for which the increase in the isolation period results in a decrease in the peak base displacement under far-fault earthquakes. For example, for H/R=0.50, ζ=0%, this decrease is 8.07%.

It is seen from Figure 13 that increasing the isolation period decreases the peak sloshing displacement demand under near-fault and far-fault earthquakes for squat tanks with H/R values smaller than 1.00. This effect is most pronounced for the smallest H/R and in case of near-fault earthquakes where the reduction in the peak sloshing displacement demand may increase to 27.54%. However, for slender tanks with H/R values greater than 1.00, this trend is reversed and short-period isolation systems result in slightly smaller peak sloshing displacement demands. In case of the highest H/R value of 2.00, this reduction is on the order of 5%.

It is observed that the normalized peak isolation system shear force responses of the tanks with long-period isolation systems (T_0=4 s) are about 50% smaller than the tanks with short-period isolation systems (T_0=2 s) under both near-fault and far-fault earthquake records (Figure 14). This trend is valid for all cases examined without any exception.

4.3.4. Influence of the Supplemental Viscous Damping Ratio, ζ

Figures 12-14 demonstrate the significant influence of the use of supplemental viscous dampers on the seismic behavior of base-isolated LSTs. As discussed in detail in Sections 4.1 and 4.2, the need for supplemental viscous damping is especially seen when the structure is subjected to near-fault earthquakes and this need rises even more as the fault-distance decreases. However, it should be kept in mind that typically a structure is threatened by more than one fault at various distances and thus potentially hit by both near-fault and far-fault earthquakes during its lifetime. The supplemental dampers provided against near-fault earthquakes will be there and thus act when the same structure is hit by a far-fault earthquake. Therefore, it is essential to assess the seismic behavior not only under near-fault earthquakes but also under far-fault earthquakes since negative effects of high damping may come into scene in the superstructure responses.

As it can be seen in Figure 12, supplemental viscous dampers reduce the peak base displacement demands with respect to no supplemental viscous damper case and increasing damping ratios from 10 to 30% steadily decrease the displacement demands. The reduction obtained for ζ=30% varies in the range of 25 ~ 50% among the examined cases. This behavior is valid for all base-isolated LSTs examined herein and for both near-fault and far-fault earthquakes.

Figure 13 shows the effect of supplemental viscous damping on the peak sloshing displacement demands. As seen, although use of supplemental viscous dampers reduce this demand for both near-fault and far-fault earthquakes, the extent of the reduction is modest, i.e. varies 10~15 among the examined cases even for ζ=30% as compared to no damper (ζ=0%) case. The effectiveness of the supplemental viscous dampers in terms of reducing peak sloshing displacement demands are more for slender tanks and less for squat tanks. It should be noted here that there may be exceptions on an individual record basis where the use of supplemental viscous dampers at the base-isolation system causes amplification in the peak sloshing displacement, which is a superstructure response (Figure 10). For example, under the SSU-090 earthquake record, adding supplemental damping with ζ=30% increases the peak sloshing displacement demand by 7.67% with respect to no supplemental damper case for H/R=1.00 and T_0=4 s.

The supplemental viscous dampers have complex effects on the peak isolation system shear force demands. In case of near-fault earthquakes -except for very high damping (ζ=30%) in case of long-period (T_0=4 s) isolation systems- increasing supplemental viscous damping ratio decreases this demand. However, for far-fault earthquakes, it is clearly seen that increasing supplemental viscous damping ratio increases the peak isolation system shear force demand, which is a superstructure response parameter.

5. CONCLUSIONS

Employing seismic isolation at the base of liquid storage tanks (LSTs) is an effective way of protecting these critical structures from the detrimental effects of earthquakes. For those located in the near-fault regions, use of supplemental viscous dampers may be essential for reducing the base displacements to acceptable values, which may on the other hand cause increase in the superstructure demands in case of far-fault earthquakes. The success of such hybrid base-isolation systems depends on the characteristics of the earthquake, the isolation system properties, and the superstructure properties. In this study, in order to determine the influence of the supplemental viscous damping ratio (ζ), the isolation system period (T_0), the tank wall flexibility, i.e. the ratio of the steel tank wall thickness to the tank radius (h/R), and the slenderness ratio, i.e. the ratio of the water height to the tank radius (H/R) on the seismic responses including the base displacement, the sloshing displacement, and the isolation system shear force demands normalized by total superstructure weight, a parametric investigation is carried out via nonlinear seismic response analyses of benchmark base-isolated LSTs with supplemental viscous dampers under six near-fault and six far-fault historical earthquake records.

Based on the results of the analyses conducted, following conclusions are reached:

- As a common observation, structural responses generally increase exponentially as the fault-distance decreases. Under some earthquake records, this increase may be much more pronounced for the base and sloshing displacement demands especially for long-period isolation systems which may be considerably increased or decreased depending on the tank slenderness ratio.

- While supplemental viscous damping is very successful in reducing high base displacement demands in near-fault cases to acceptable levels, the extent of the reduction

is modest in terms of sloshing displacement demands. There may even be exceptions where supplemental viscous dampers cause slight amplifications on the sloshing displacement, which is a superstructure response. And, the effectiveness of the supplemental viscous dampers in terms of reducing sloshing displacement demands are more for slender tanks with H/R values larger than 1.00 and less for squat tanks with H/R values smaller than 1.00.

- In case of near-fault earthquakes -except for high damping ($\zeta=30\%$)- increasing supplemental viscous damping decreases the isolation system shear force. However, employing and increasing supplemental viscous damping increase the isolation system shear force -a superstructure response- in case of far-fault earthquakes.

- Under both near-fault and far-fault earthquakes, while increasing the isolation period decreases the sloshing displacement demand for squat tanks, it slightly reduces the sloshing displacement demand for slender tanks. Especially for long-period isolation systems, increase in the tank slenderness ratio generally increases the sloshing displacement demands.

- Normalized isolation system shear force demands are greater for short-period isolation systems and increase with the increase in the tank slenderness ratio under both near-fault and far-fault earthquakes.

- The influence of tank flexibility, i.e. tank-fluid interaction, on both the superstructure and the isolation system responses is negligibly small for LSTs with hybrid base-isolation systems. This finding is in line with other studies in the literature on base-isolated LSTs without supplemental dampers.

The conclusions above are drawn by neglecting the wave-wave, wave-wall and wave-roof interactions. These interactions may be important especially in case of high amplitude vibrations. Therefore, further investigations considering these interactions particularly in case of near-fault earthquakes should be carried out as part of the future studies.

References

[1]   Lee, S., Kim, B., Lee, Y-J., Seismic Fragility Analysis of Steel Liquid Storage Tanks using Earthquake Ground Motions Recorded in Korea. Math. Probl. Eng., Article ID 6190159, 15 pages, 2019.

[2]   Zhao, Z., Lu, X., Guo, Y., Zhao, X., Seismic Fragility Assessment of Base-Isolated Steel Water Storage Tank. Shock Vib., Article ID 8835943, 13 pages, 2020.

[3]   Tsipianitis, A., Tsompanakis, Y., Optimizing the Seismic Response of Base-Isolated Liquid Storage Tanks using Swarm Intelligence Algorithms. Comput. Struct., 243, 106407, 2021.

[4] Hatayama, K., Lessons from the 2003 Tokachi-oki, Japan, Earthquake for Prediction of Long-Period Strong Ground Motions and Sloshing Damage to Oil Storage Tanks. J. Seismol., 12, 255-263, 2008.

[5] Yazici, G., Cili, F., Evaluation of the Liquid Storage Tank Failures in the 1999 Kocaeli Earthquake. 14th World Conference on Earthquake Engineering, Beijing, China, 2008.

[6] Jadhav, M.B., Jangid, R.S., Response of Base-Isolated Liquid Storage Tanks. Shock and Vibration, 11, 33-45, 2004.

[7] Shrimali, M.K., Jangid, R.S., Seismic Analysis of Base-Isolated Liquid Storage Tanks. Journal of Sound and Vibration, 275(1), 59-75, 2004.

[8] Jadhav, M.B., Jangid, R.S., Response of Base-Isolated Liquid Storage Tanks to Near-Fault Motions. Structural Engineering and Mechanics, 23(6), 615-634, 2006.

[9] Shekari, M.R., Khaji, N., Ahmadi, M.T., On the Seismic Behavior of Cylindrical Base-Isolated Liquid Storage Tanks Excited by Long-Period Ground Motions. Soil Dynamics and Earthquake Engineering, 30, 968-980, 2010.

[10] Panchal, V.R., Soni, D.P., Seismic Behaviour of Isolated Fluid Storage Tanks: A-State-of-the-Art Review. KSCE J. Civ. Eng., 18(4), 1097-1104, 2014.

[11] Saha, S.K., Matsagar, V., Chakraborty, S., Uncertainty Quantification and Seismic Fragility of Base-Isolated Liquid Storage Tanks using Response Surface Models. Probabilistic Eng. Mech., 43, 20-35, 2016.

[12] Hashemi, S., Aghashiri, M.H., Seismic Responses of Base-Isolated Flexible Rectangular Fluid Containers under Horizontal Ground Motions. Soil Dyn. Earthq. Eng., 100, 159-168, 2017.

[13] Alhan, C., Gazi, H., Güler, E., Influence of Isolation System Characteristic Strength on the Earthquake Behavior of Base-Isolated Liquid Storage Tanks. Indian J. Eng. Mater. Sci., 25(4), 346-352, 2018.

[14] Tsipianitis, A., Tsompanakis, Y., Impact of Damping Modeling on the Seismic Response of Base-Isolated Liquid Storage Tanks. Soil Dynamics and Earthquake Engineering, 121, 281-292, 2019.

[15] Housner, G.W., Trifunac, M.D., Analysis of Accelerograms-Parkfield Earthquake. Bull. Seismol. Soc. Am., 57(6), 1193-220, 1967.

[16] Makris, N., Rigidity-Plasticity-Viscosity: Can Electrorheological Dampers Protect Base Isolated Structures from Near-Source Ground Motions? Earthq. Eng. Struct. Dyn., 26, 571-591, 1997.

[17] Bray, J.D., Rodriguez-Marek, A., Characterization of Forward-Directivity Ground Motions in the Near-Fault Region. Soil Dyn. Earthq. Eng., 24, 815-828, 2004.

[18] He, W.L., Agrawal, A.K., An Analytical Model of Ground Motion Pulses for the Design and Assessment of Smart Protective Systems. ASCE J. Struct. Eng., 134(7), 1177-1188, 2008.

[19] Kanbir, Z., Alhan, C., Özdemir, G., Influence of Superstructure Modeling Approach on the Response Prediction of Buildings with LRBs Considering Heating Effects. Structures, 28, 1756-1773, 2020.

[20] Hall, J.F., Seismic Response of Steel Frame Buildings to Near-Source Ground Motions. Earthq. Eng. Struct. Dyn., 27, 1445-1464, 1998.

[21] Somerville, P.G., Graves, R.W., Characterization of Earthquake Strong Ground Motion. Pure Appl. Geophys., 160, 1811-1828, 2003.

[22] Alhan, C., Güler, E., Gazi, H., Behavior of Base-Isolated Liquid Storage Tanks under Synthetic Near-Fault Earthquake Pulses. 5th International Symposium on Life-Cycle Civil Engineering, Delft, Holland, 515, 2415-2419, 2016.

[23] Haroun, M.A., Housner, G.W., Seismic Design of Liquid Storage Tanks. Journal of the Technical Councils of ASCE, 107, 191-207, 1981.

[24] Kalogerakou, M.E., Maniatakis, C.A., Spyrakos, C.C., Psaropoulos, P.N., Seismic Response of Liquid-Containing Tanks with Emphasis on the Hydrodynamic Response and Near-Fault Phenomena. Eng. Struct., 153, 383-403, 2017.

[25] Housner, G.W., Earthquake Pressures on Fluid Containers, Tech. Rep. NR-081-095, California Institute of Technology, Pasadena, California, 1954.

[26] Öncü-Davas, S., Gazi, H., Güler, E., Alhan, C., Comparison of Ground Motion Pulse Models for the Seismic Response of Seismically Isolated Liquid Storage Tanks, Earthquake Engineering and Structural Dynamics in Memory of Ragnar Sigbjörnsson, In: Rupakhety, R. and Olafsson, S., (eds.), Chapter 7, Springer International Publishing AG, Geotechnical, Geological and Earthquake Engineering, 143-157, 2018.

[27] Safari, S., Tarinejad, R., Parametric Study of Stochastic Seismic Responses of Base-Isolated Liquid Storage Tanks under Near-Fault and Far-Fault Ground Motions. J. Vib. Control, 24, 5747-5764, 2018.

[28] Tsopelas, P.C., Constantinou, M.C., Reinhorn, A.M., 3D-BASIS-ME: Computer Program for Nonlinear Dynamic Analysis of Seismically Isolated Single and Multiple Structures and Liquid Storage Tanks, Tech. Rep. NCEER-94-0010, National center for earthquake engineering research, State Univ. of New York, Buffalo, NY, 1994.

[29] Castellano, M.G., Infanti, S., Dumoulin, C., Ducoup, L., Martelli, A., Dusi, A., Shaking Table Tests on a Liquefied Natural Gas Storage Tank Mock-up Seismically Protected with Elastomeric Isolators and Steel Hysteretic Torsional Dampers. 12th World Conference on Earthquake Engineering, Auckland, New Zealand, 2000.

[30] Gazi, H., Kazezyılmaz-Alhan, C.M., Alhan, C., Behavior of Seismically Isolated Liquid Storage Tanks Equipped with Nonlinear Viscous Dampers in Seismic Environment. 10th Pacific Conference on Earthquake Engineering, Sydney, Australia, 2015.

[31] Luo, H., Zhang, R., Weng, D., Mitigation of Liquid Sloshing in Storage Tanks by using a Hybrid Control Method. Soil Dyn. Earthq. Eng., 90, 183-195, 2016.

[32] Güler, E., Alhan, C., Performance Limits of Base-Isolated Liquid Storage Tanks with/without Supplemental Dampers under Near-Fault Earthquakes. Structures, 33, 355-367, 2021.

[33] Tsipianitis, A., Tsompanakis, Y., Improving the Seismic Performance of Base-Isolated Liquid Storage Tanks with Supplemental Linear Viscous Dampers. Earthq. Eng. Eng. Vib., 21, 269-282, 2022.

[34] Bakalis, K., Fragiadakis, M., Vamvatsikos, D., Surrogate Modeling for the Seismic Performance Assessment of Liquid Storage Tanks. Journal of Structural Engineering, 143(4): 1–13, 2017.

[35] Güler, E., Effect of Supplemental Damping on the Earthquake Behavior of Base-Isolated Liquid Storage Tanks, Ph.D. Thesis, Istanbul University-Cerrahpaşa, Institute of graduate studies, 2019.

[36] Malhotra, P.K., Wenk, T., Wieland, M., Simple Procedure for Seismic Analysis of Liquid-Storage Tanks. Struct. Eng. Int., 3, 197-201, 2000.

[37] Shrimali, M.K., Jangid, R.S., Seismic Analysis of Base-Isolated Liquid Storage Tanks. J. Sound Vib., 275, 59-75, 2004.

[38] Seleemah, A.A., El-Sharkawy, M., Seismic Response of Base Isolated Liquid Storage Ground Tanks. Ain Shams Eng. J., 2(1), 33-42, 2011.

[39] Compagnoni, M.E., Curadelli, O., Ambrosini, D., Experimental Study on the Seismic Response of Liquid Storage Tanks with Sliding Concave Bearings. J. Loss Prev. Process Ind., 55, 1-9, 2018.

[40] Nagarajaiah, S., Reinhorn, A.M., Constantinou, M.C., 3D-BASIS: Nonlinear Dynamic Analysis of Three-Dimensional Base Isolated Structures, Tech. Rep. NCEER-89-0019, National Center for Earthquake Engineering Research, State University of New York, Buffalo, NY, 1989.

[41] Bouc, R., Forced Vibrations of a Mechanical System with Hysteresis. 4th Conference on Non-linear Oscillations, Prague, Czechoslovakia, pp. 315, 1967.

[42] Wen, Y.K., Method for Random Vibration of Hysteretic Systems. J. Eng. Mech. Div., 102, 246-263, 1976.

[43] Park, Y., Wen, Y., Ang, A., Random Vibration of Hysteretic Systems under Bi-directional Ground Motions. Earthquake Eng. Struct. Dyn., 14, 543–557, 1986.

[44] Naeim, F., Kelly, J.M., Design of Seismic Isolated Structures: From Theory to Practice, 978-0-471-14921-7, John Wiley & Sons, New York, 1999.

[45] Eurocode 8: EN1998. Design of Structures for Earthquake Resistance, Part 4: Silos, Tanks and Pipelines, Brussels, Belgium, 2006.

[46] ASCE 7. Minimum Design Loads and Associated Criteria for Buildings and Other Structures, ASCE/SEI 7-16, Reston, Virginia, 2017.

[47] Scheller, J., Constantinou, M.C., Response History Analyses of Structures with Seismic Isolation and Energy Dissipation Systems: Verification Examples for Program SAP2000, Technical Report MCEER-99-0002, University at Buffalo, New York, 1999.

[48] Newmark, N.M., A Method of Computation for Structural Dynamics, J. of Engrg. Mech. Div. ASCE, 85, 67-94, 1959.

[49] Rosenbrock, H.H., Some General Implicit Processes for the Numerical Solution of Differential Equations, Computer J., 18, 50-64, 1964.

[50] Mavroeidis, G.P., Dong, G., Papageorgiou, A.S., Near-Fault Ground Motions, and the Response of Elastic and Inelastic Single-Degree-of-Freedom (SDOF) Systems. Earthq. Eng. Struct. Dyn., 33(9), 1023-49, 2004.

[51] Yadav, K.K., Gupta, V.K., Near-Fault Fling-Step Ground Motions: Characteristics and Simulation. Soil Dyn. Earthq. Eng., 101, 90-104, 2017.

[52] Bertero, V.V., Mahin, S.A., Herrera, R.A., Aseismic Design Implications of Near-Fault San Fernando Earthquake Records. Earthq. Eng. Struct. Dyn., 6(1), 31-42, 1978.

[53] Mavroeidis, G.P., Papageorgiou, A.S., A Mathematical Representation of Near-Fault Ground Motions. Bull. Seismol. Soc. Am., 93(3), 1099-131, 2003.

[54] Güler, E., Alhan, C., Effectiveness of Non-Linear Fluid Viscous Dampers in Seismically Isolated Buildings. Earthq. Struct., 17(2), 191-204, 2019.

[55] Hall, J.F., Heaton, T.H., Halling, M.W., Wald, D.J., Near-Source Ground Motion and its Effects on Flexible Buildings. Earthq. Spectra, 11(4), 569-605, 1995.

[56] Heaton, T.H., Hall, J.F., Wald, D.J., Halling, M.W., Response of High-Rise and Base-Isolated Buildings to a Hypothetical Mw 7.0 Blind Thrust Earthquake. Science, 267, 206-11, 1995.

[57] PEER, Pacific Earthquake Engineering Research Center Ground Motion Database, University of California, Berkeley, CA, 2013 (http://ngawest2.berkeley.edu).

[58] Saha, S.K., Matsagar, V.A., Jain, A.K., Response of Base-Isolated Liquid Storage Tanks under Near-Fault Earthquakes. Indian Society of Earthquake Technology Golden Jubilee Symposium, Roorkee, India, D011, 2012.

[59] Haroun, M.A., Vibration Studies and Tests of Liquid Storage Tanks. Earthq. Eng. Struct. Dyn., 11, 179-206, 1983.

[60] Malhotra, P.K., Method for Seismic Base Isolation of Liquid-Storage Tanks. J. Struct. Eng., 123, 113-6, 1997.

[61] Veletsos, A.S., Yang, J.Y., Earthquake Response of Liquid Storage Tanks. 2nd Engineering Mechanics Specialty Conference, ASCE, Raleigh, North Carolina, USA, pp. 1-24, 1977.

Turkish Journal of Civil Engineering (formerly Teknik Dergi) Manuscript Drafting Rules

1. The whole manuscript (text, charts, equations, drawings etc.) should be arranged in Word and submitted in ready to print format. The article should be typed on A4 (210 x 297 mm) size paper using 10 pt (main title 15 pt) Times New Roman font, single spacing. Margins should be 40 mm on the left and right sides and 52.5 mm at the top and bottom of the page.

2. Including drawings and tables, articles should not exceed 25 pages, technical notes 10 pages.

3. Your contributed manuscript must be sent over the DergiPark system. (http://dergipark.gov.tr/tekderg)

4. The text must be written in a clear and understandable language, conform to the grammar rules. Third singular person and passive tense must be used, and no inverted sentences should be contained.

5. Title must be short (10 words maximum) and clear, and reflect the content of the paper.

6. Sections should be arranged as: (i) abstract and keywords, (ii) title, abstract and keywords in the other language, (iii) main text, (iv) symbols, (v) acknowledgements (if required) and (vi) references.

7. Both abstracts should briefly describe the object, scope, method and conclusions of the work and should not exceed 100 words. If necessary, abstracts may be re-written without consulting the author. At least three keywords must be given. Titles, abstracts and keywords must be fitted in the first page leaving ten line space at the bottom of the first page and the main text must start in the second page.

8. Section and sub-section titles must be numbered complying with the standard TS1212.

9. Symbols must conform to the international rules; each symbol must be defined where it appears first, additionally, a list of symbols must be given in alphabetic order (first Latin, then Greek alphabets) at the end of the text (before References).

10. Equations must be numbered and these numbers must be shown in brackets at the end of the line.

11. Tables, drawings and photographs must be placed inside the text, each one should have a number and title and titles should be written above the tables and below the drawings and photographs.

12. Only SI units must be used in the manuscripts.

13. Quotes must be given in inverted commas and the source must be indicated with a reference number.

14. Acknowledgement must be short and mention the people/ institutions contributed or assisted the study.

15. References must be numbered (in brackets) in the text referring to the reference list arranged in the order of appearance in the text. References must include the following information:

    If the reference is an article: Author's surname, his/her initials, other authors, full title of the article, name of the journal, volume, issue, starting and ending pages, year of publication.

    > Example : Naghdi, P. M., Kalnins, A., On Vibrations of Elastic Spherical Shells. J. Appl. Mech., 29, 65-72, 1962.

    If the reference is a book: Author's surname, his/her initials, other authors, title of the book, volume number, editor if available, place of publication, year of publication.

    > Example : Kraus. H., Thin Elastic Shells, New York. Wiley, 1967.

    If the reference is a conference paper: Author's surname, his/her initials, other authors, title of the paper, title of the conference, location and year.

    If the source is a thesis: Author's surname, his/her initials, thesis title, level, university, year.

    If the source is a report: Author's surname, his/her initials, other authors, title of the report, type, number, institution it is submitted to, publication place, year.

16. Discussions to an article published in Turkish Journal of Civil Engineering (formerly Teknik Dergi) should not exceed two pages, must briefly express the addressed points, must criticize the content, not the author and must be written in a polite language. Authors' closing remarks must also follow the above rules.

17. A separate note should accompany the manuscript. The note should include, (i) authors' names, business and home addresses and phone numbers, (ii) brief resumes of the authors and (iii) a statement "I declare in honesty that this article is the product of a genuinely original study and that a similar version of the article has not been previously published anywhere else" signed by all authors.

18. Copyright has to be transferred to UCTEA Turkish Chamber of Civil Engineers. The standard copyright form signed by the authorised author should therefore be submitted together with the manuscript.